Azimuthal Anisotropy Measurement of Neutral Pion and Direct Photon in $\sqrt{s_{\mathrm{NN}}} = 200$ GeV Au + Au Collisions at RHIC-PHENIX

Kentaro MIKI

February 2009

Azimuthal Anisotropy Measurement of Neutral Pion and Direct Photon in $\sqrt{s_{\mathrm{NN}}} = 200$ GeV Au + Au Collisions at RHIC-PHENIX

Kentaro MIKI
(Doctoral Program in Physics)

Submitted to the Graduate School of
Pure and Applied Sciences
in Partial Fulfillment of the Requirements
for the Degree of Doctor of Philosophy in
Science

at the
University of Tsukuba

Abstract

The existence of quarks and gluons as a smaller structure inside the nucleus has been discovered by development of particle accelerators. According to the Quantum Chromodynamics theory (QCD), mesons and baryons are expected to transform into a new phase of matter at an extreme temperature and density. Mesons and baryons would be lost their identities and release their partons into finite volume in such the extreme state, named Quark Gluon Plasma (QGP). Relativistic heavy-ion collisions is a unique tool to realize the phase transition to QGP state on the earth.

The space-time evolution of a high energy density matter or state generated by relativistic heavy-ion collisions involves complicated processes, and they are investigated by measuring particles in the final state of the system development, mostly hadrons. However thermal equilibrium and the QGP are expected to exist only at the very early stage of collisions, and significant amount of the information can be masked by large number of emissions from the final state.

Direct photons which are defined as photons not resulting from hadronic decay such as $\pi^0 \rightarrow 2\gamma$, are a powerful and direct probe to study the early stage of heavy-ion collisions, since the direct photons do not interact strongly with the hot and dense medium because of its large mean free path, (photon mean free path in QGP is 20 times larger than that of quarks), and thus can carry out directly the thermodynamical and/or kinematical information on the state of production source.

In the heavy-ion collision experiments at the Relativistic Heavy-Ion Collider (RHIC), a strong suppression has been observed in hadron yields at high transverse momentum (p_{T}) in central Au+Au collisions compared with p+p collisions scaled by the number of binary nucleon-nucleon collisions. The observed high-p_{T} suppression is attributed to a characteristic of energy loss of hard-scattered partons passing through the high density matter. On the contrary, non suppression of high-p_{T} direct photon yields has been observed in Au+Au collisions.

Although the measurements of direct photon as a penetrating probe provides direct and more reliable information of the early stage of collisions, photons are emitted at all the stage of collisions such as hard-scattering on the initial stage, interaction of quarks and gluons on the thermalized phase, and the hadron gas on the late stage. Thus there is complexity to entangle a particular source of photon experimentally.

In non-central heavy-ion collisions, a geometrical shape of the collision zone becomes almond like shape. The anisotropic shape of participant produces the modification of pressure gradients and particle density in azimuth, which causes the azimuthal anisotropy in particle emission. Photon emissions are also sensitive to the anisotropic structure of the generation source, and they are going through the collision region without re-scattering. Therefore, an azimuthal anisotropy parameter v_2 is a powerful tool to explore the source of direct photons. If more partons, parent of the direct photon, are emitted in the short-axis direction of the ellipsoid, v_2 should have a positive sign. Photons resulting from initial Compton-like hard-scattering are expected to exhibit a zero v_2 if they do not interact with the hot dense matter. The v_2 of photons from parton fragmentation are expected to have a similar v_2 to hadron's because of the suppression of high-p_{T} hadrons. On the other hand, photons resulting from the energy loss of parton jets in

the hot dense medium caused by Bremsstrahlung should have negative v_2, because the partons emitted in the direction of the major ellipsoidal axis of the collisions region should produce more Bremsstrahlung photons.

In this thesis we perform the v_2 measurements of neutral pion and direct photon to discuss about the properties of hot and dense medium which generated by heavy-ion collisions, in $\sqrt{s_{\rm NN}}$ = 200 GeV Au+Au collisions at RHIC-PHENIX. The measured v_2 of direct photon is well described with $v_2 = 0$ at $p_{\rm T} > 6$ GeV/c, it indicates that the most of direct photons are emitted from initial hard-scattering of partons, which should have zero v_2. This is consistent with independent measurements such as the non-suppressed direct photon which is confirmed by nuclear modification factor ($R_{\rm AA}$) of direct photon and neutral pion. Although a systematical error of direct photon is significantly large, it is important to extend the discussion about secondary contribution in the direct photon yield. A fraction of direct photon contribution in high-$p_{\rm T}$ is speculated from the experimental results of v_2 and $R_{\rm AA}$ of direct photon and neutral pion with some suppositions. In the meantime, spectra of low-$p_{\rm T}$ direct photon which are expected to emit from the thermalized phase have been observed by using an internal conversion to dilepton of a virtual photon as an alternative approaching for direct photons. From the results of excess ratio of direct photons via dilepton measurement, we discuss about the low-$p_{\rm T}$ direct photon v_2 with referring to a collective flow of quarks or hadrons.

Contents

List of Figures

List of Tables

Acknowledgement

First of all, I would like to express my great appreciation to Prof. Y. Miake for providing me the exciting opportunity for physics research and discussions, and I could learn a lot from him as not only an experimental physicist but many aspects of life.

I would like to express my thanks to Prof. S. Esumi. His continuous encouragement, valuable ideas, and appropriate answers for my questions show me the reliable directions of my work.

I express my thanks to Prof. T. Chujo. His careful reading of my thesis and proper comments lead much improvement of this work.

The continuous financial support from PHENIX-J and RIKEN was essential to continue work. I would like to express many thanks to the all member of the PHENIX-J group, especially, Prof. H. Hamagaki, and Prof. K. Ozawa for their supports. I also would like to express my thanks the chief scientist of the radiation laboratory at RIKEN, Dr. H. En'yo for providing me many supports through the Junior Research Associate program.

I express my heartfelt appreciation to Dr. T. Sakaguchi for leading me for the photon analysis and valuable discussions in PHENIX. His appropriate and kind advices have helped me a lot for this work.

I acknowledge the member of the high energy nuclear experiment group at University of Tsukuba. I express my thanks to staffs, Prof. M. Inaba, Mr. S. Kato, and Ms. H. Sakai for their useful advise and many supports. I appreciate Dr. H. Masui, Dr. S. Sakai, Dr. M. Konno, Ms. M. Shimomura, Mr. Y. Ikeda, Mr. R. Tanabe, Mr. K. Watanabe, Mr. D. Sakata, Mr. M. Sano, Mr. H. Yokoyama, Ms. M. Kajigaya, Mr. E. Hamada, Mr. N. Shiohara, Ms. M. Kimura, Mr. T. Todoroki, Mr. P. Chang, Mr. Y. Sekine, and Mr. T. Takeuchi and many other colleagues for their advice and encouragements.

I wish to acknowledge all the collaborators of the PHENIX experiment. I would like to appreciation to Dr. Y. Akiba, Dr. G. David, Dr. B. Jacak, Dr. D. Winter, Dr. A. Kiyomichi, Dr. S. Milov, Dr. J. Mitchell, Dr. E. O'Brien, Dr. C. Ogilvie, Dr. K. Okada, and Dr. C. Pinkenburg for their valuable advices and supports. I also wish to express many thanks to Mr. Y. Nakamiya, Mr. Y. Morino, Mr. K. Sakashita, Mr. J. Tamura, and Mr. S. Dairaku for their friendship in the BNL life.

I would like to express many thanks to Mr. M. Igarashi, Mr. M. Yamaura, Mr. T. Motokizawa, and Mr. Y. Kobayashi for their friendship in campus life.

Finally, I would like to express my great appreciation to my parents and brothers, Kyoji, Eiko, Ayumi, and Tatsuya for their tender support and encouragement. I could never finish this work without their great help and understanding.

Thank you again for all.

Chapter 1

Introduction

All of things we can see in the world are composed of atoms. Existence of a nucleus inside the atom was found by E. Rutherford in 1911. In the latter half of the 20th century, studying of the matter structure is developed into smaller and smaller scales, science has been on a continual quest to find the most elementary particle forming the substance of the universe. According to the discovery of various particles by development of particle accelerators, we found the smaller structure even inside the proton/neutron, named quarks and gluons.

In normal state, quarks are confined in mesons or baryons. On the other hand, a quark gluon plasma (QGP) state which exists at extremely high temperature and density, mesons and baryons lose their identities and release their quarks and gluons into an finite volume.

In the universe, such an extremely state to form the QGP is thought to exist in the early stage after a few μs from the Big Bang. Now, relativistic heavy-ion collisions provide a unique occasion to achieve those conditions on the earth. In this chapter, Quantum Chromodynamics (QCD), underlying theory of the strong interaction of quarks and gluons, and experimental observables at the Relativistic Heavy-Ion Collider (RHIC) for the study of QGP are described.

1.1 Quantum Chromodynamics and Quark Gluon Plasma

Quantum Chromodynamics (QCD) has been developed for the theory of strong interaction between quarks. One of the important features in the QCD is "color confinement": quarks and gluons have a degree of freedom of color, and they can not be observed as naked particles since they are confined in hadrons as a color-singlet state. The next remarkable characteristic of QCD is "asymptotic freedom": at high energy and/or short distance, the strong coupling constant α_s becomes small, and quarks and gluons interact weakly.

According to the theoretical prediction by using QCD, there is the quite interesting property of nuclear matter at high density and temperature [1][2][3]. Especially it is suggested the existence of new phases of nuclear matter, which quarks and gluons would be liberated from color confinement in the finite volume at an extreme temperature and density [4]. This new state is called "Quark Gluon Plasma (QGP)". The first extensive study of such the high temperature state in detail was given in 1980 [5].

The perturbative QCD (pQCD) calculation is performed for interactions with large momen-

tum transfers at the short distance stage. In order to study the strong coupling stage where pQCD calculations is not valid, the Lattice QCD is used as a strong tool to study phase transition phenomena. The calculation using Lattice QCD predicts a phase transition temperature is $T \approx 170$ MeV $\approx 10^{12}$ K, and it is corresponding to an energy density $\varepsilon \approx 1$ GeV/fm^3. Figure 1.1 shows the results for ε/T^4, where ε is energy density and T is temperature, as a function of temperature scaled by the critical temperature T_C calculated by Lattice QCD [6].

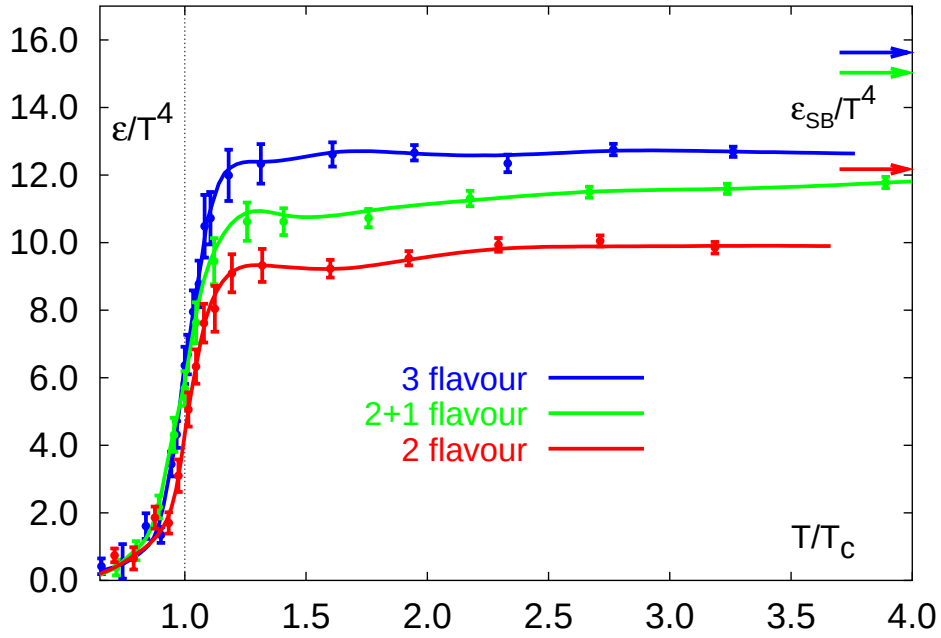

Figure 1.1: Energy density/T^4 as a function of temperature scaled by the critical temperature T_C resulting from Lattice QCD calculation [6]. The arrows on the right side indicating the values for the Stefan-Boltzmann limit.

In the limit of massless noninteracting particles ("Stefan-Boltzmann" limit), each bosonic degree of freedom contributes $(\pi^2/30) \cdot T^4$ to the energy density. And each fermionic degree of freedom contributes $\frac{7}{8}$ of this value. The energy density in "Stefan-Boltzmann" limit is,

$$\varepsilon_{SB} = \left(\frac{7}{8} d_{\text{quark}} + d_{\text{gluon}}\right) \frac{\pi^2}{30} T^4, \tag{1.1}$$

$$\varepsilon^2_{SB} = \left(2_f \cdot 2_s \cdot 2_q \cdot 3_c \cdot \frac{7}{8} + 2_s \cdot 8_c\right) \frac{\pi^2}{30} T^4 = 37 \frac{\pi^2}{30} T^4 \tag{1.2}$$

$$\varepsilon^3_{SB} = \left(3_f \cdot 2_s \cdot 2_q \cdot 3_c \cdot \frac{7}{8} + 2_s \cdot 8_c\right) \frac{\pi^2}{30} T^4 = 47.5 \frac{\pi^2}{30} T^4 \tag{1.3}$$

where, $\varepsilon^{2(3)}_{SB}$ denotes the energy density for the case of 2 or 3 active flavors in the QGP. The degree of freedom for quarks (the appropriate flavor, spin, quark/antiquark, and color factors) and that for gluons (spin and color factor) are summing into the energy density calculation. Calculated Stefan-Boltzmann limits are also indicated in Fig. 1.1 as arrow symbols. When the temperature gets over the critical temperature T_C, the hadronic matter would transit into a new

phase. Even at a temperature over the $T_{\rm C}$, the interaction between quarks and gluons are not negligible because of Stefan-Boltzmann limit is still larger.

1.2 High Energy Heavy-Ion Collision

Relativistic heavy-ion collision is a unique tool to realize the phase transition to QGP on the earth, which is predicted by QCD at extreme temperature and density. Since 1980's the investigations have been taking place both at the Brookhaven National Laboratory (BNL) and European Organization for Nuclear Research (CERN), as summarized in Table 1.1.

Table 1.1: Heavy ion accelerator facilities with the ion beams, and the center of mass energy.

Accelerator	Location	Ion beam	$\sqrt{s_{\rm NN}}$ [GeV]	Year
AGS	BNL	^{16}O, ^{28}Si	5.4	1986
		^{197}Au	4.8	1992
SPS	CERN	^{16}O, ^{32}S	19.4	1986
		^{208}Pb	17.4	1994
RHIC	BNL	^{197}Au	130	2000
		^{197}Au	200	2001, 2004, 2007
		d+^{197}Au	200	2003
		^{197}Au	62.4	2004
		$^{63.5}$Cu	200	2005
LHC	CERN	proton	14000	2009 (projected)

1.2.1 Participant Spectator Picture

In the high energy heavy-ion collision experiment, extreme velocity of Lorentz contracted nucleus being much faster than Fermi motion allows us to separate the nucleus-nucleus collisions into two parts; "participants" which is taking part in the primary collisions, and "spectators" which is the rest one. In this picture, the spectator going through the collision region keeping their velocity, while the mostly secondary particles from participants are emitted in the mid-rapidity. Figure 1.2 shows the illustration of nucleus (looks like thin disks due to the Lorentz contraction) for a heavy-ion collision.

The impact parameter b is defined by the distance between the center of nuclei in the heavy-ion collisions. The number of participant nucleons ($N_{\rm part}$), nucleon-nucleon collisions are related to the given b by using the Glauber Model [10].

1.2.2 Space Time Evolution of the Colliding System

Figure 1.3 shows the system development after initial collision in the center-of-momentum frame with longitudinal position z and time t in relativistic heavy-ion collisions.

J. D. Bjorken proposed a scenario to describe various phases in the relativistic heavy ion collisions and initial energy density of medium. In the initial parton-parton collision, the free partons are generated between the two nuclei. The system begins expansion in space, and its

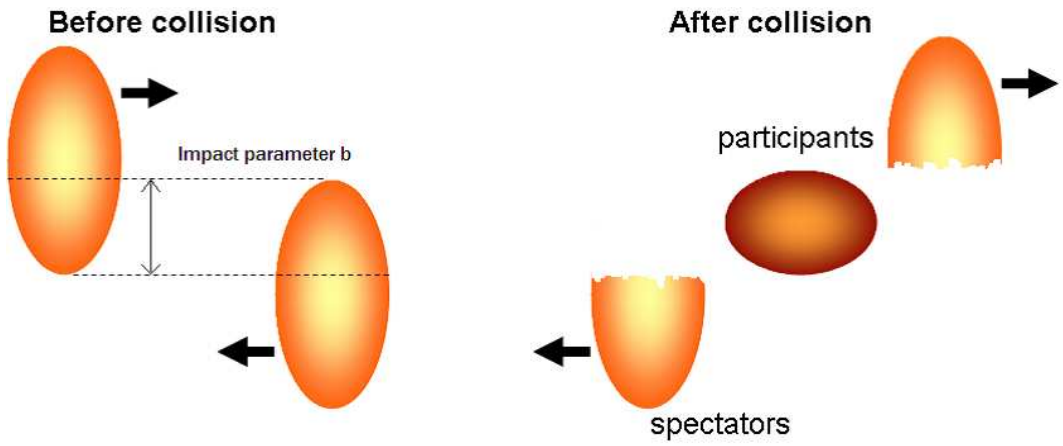

Figure 1.2: Participant spectator picture for a heavy ion collision.

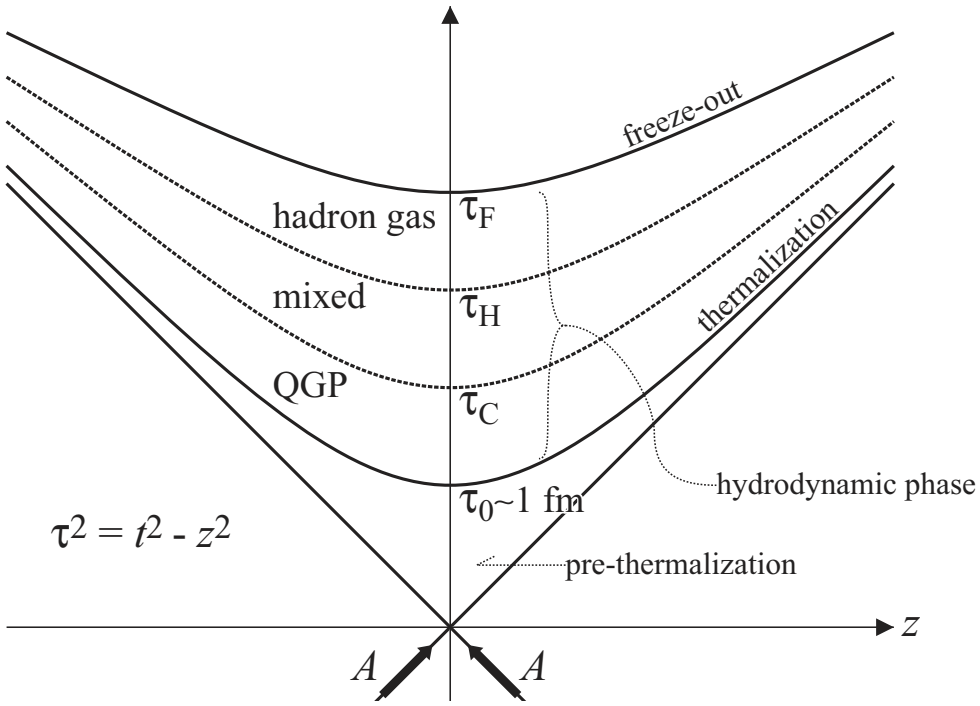

Figure 1.3: Space-time evolution of the system in center-of-momentum frame in relativistic heavy-ion collisions.

dynamics may be described by a cascade of colliding partons. In case of deposited energy is large enough and exceeds the critical energy, QGP might be formed from $t = \tau_0$. If the system keep their entropy during expansion, the system will reach the critical temperature between QGP and ordinary hadrons at $t = \tau_C$. After QGP formed in the collision region, the system expands and cools down. Then, the system becomes the ordinary hadron gas at $t = \tau_H$ and is expanded by the interaction of produced hadrons. Finally at $t = \tau_F$, each hadron does not interact and freeze out.

The achieved energy density at the QGP formation time $t = \tau_0$ is estimated by using rapidity y and τ,

$$y = \frac{1}{2}\ln\frac{E+p_z}{E-p_z}, \tag{1.4}$$

$$= \frac{1}{2}\ln\frac{t+z}{t-z} \quad (v_z = \frac{z}{t} = \frac{p_z}{E}), \tag{1.5}$$

$$\tau = \sqrt{t^2-z^2}. \tag{1.6}$$

The deposit energy E at $t = \tau_0$ is estimated from a longitudinal thickness of collision region ($2d$), and the overlap area S ($S = \pi r^2$, r is nucleon radius) as,

$$E = \frac{d\langle E\rangle}{dy}\Delta y, \tag{1.7}$$

$$= \frac{d\langle E\rangle}{dy}\cdot\frac{2d}{\tau_0}, \tag{1.8}$$

where, $\langle E\rangle$ is a mean energy. Then the energy density in the Bjorken picture is given by,

$$\varepsilon_{Bj} = \frac{E}{2dS}, \tag{1.9}$$

$$= \frac{1}{S}\frac{1}{\tau_0}\frac{d\langle E\rangle}{dy}, \tag{1.10}$$

$$= \frac{1}{\tau_0\pi r_0^2 N^{2/3}}\frac{d\langle E\rangle}{dy}, \tag{1.11}$$

$$\approx \frac{\langle E_{\rm T}\rangle}{\tau_0\pi r_0^2 N^{2/3}}\frac{dN}{dy}, \tag{1.12}$$

where, $\langle E_{\rm T}\rangle$ is the mean transverse energy, dN/dy is the rapidity density of multiplicity. In this equation, $d\langle E\rangle/dy|_{y=0} = d\langle E_{\rm T}\rangle/dy|_{y=0} = \langle E_{\rm T}\rangle/dy \cdot dN/dy$ is assumed at $y = 0$. In case of RHIC energy ($\sqrt{s_{\rm NN}} = 200$ GeV) and collision nucleus (^{197}Au) at $\tau_0 = 1$ fm/c,

$$\varepsilon_{Bj} \approx 5.0({\rm GeV/fm}^3), \tag{1.13}$$

are estimated. This energy density is large enough for the QGP phase transition. Figure 1.4 shows the energy density by choosing $\tau_{\rm form} = 1$ fm/c as a function of the number of participant nucleus measure at PHENIX [27].

1.3 Experimental Observables

The experimental data of high energy heavy ion collisions have been collected using the Relativistic Heavy Ion Collider (RHIC) at Brookhaven National Laboratory (BNL) since 2000. The primary goal of RHIC is the experimental study of the QCD phase transition. The RHIC accelerator and its experimental facilities produce collisions of Au+Au, p+p, and d+Au for the study of QCD phase transition from various "probes" of hot and dense medium.

The hadron emission from initial stage of collisions is the one of most significant probes to study the QCD transition. In this section, transverse mass spectra, particle ratios, and azimuthal distribution of produced hadrons are described from the view point of the thermalization of the system.

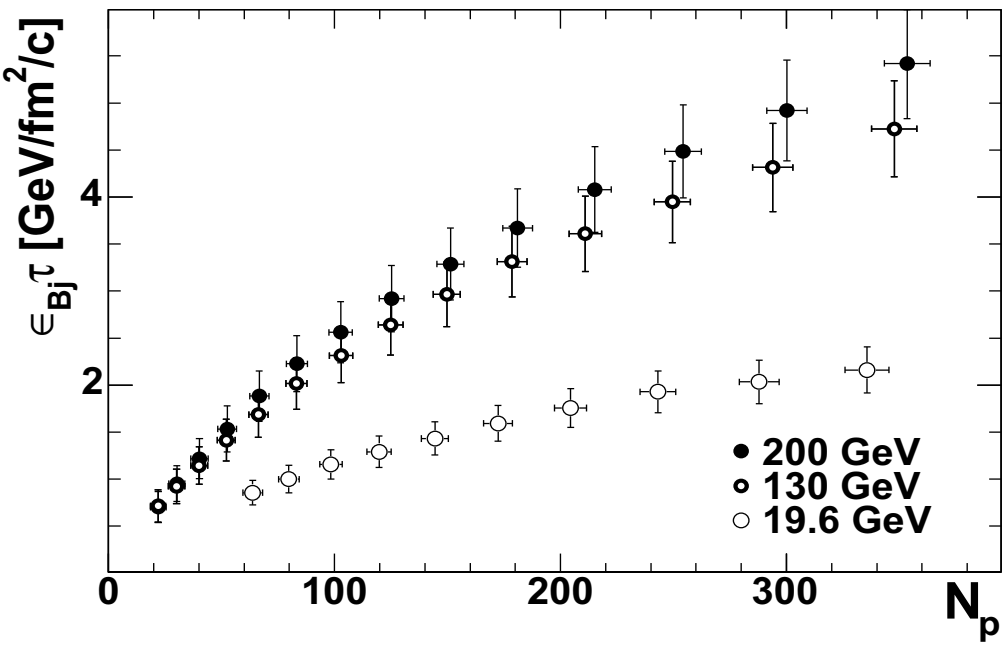

Figure 1.4: Energy density as a function of N_{part} measured at three RHIC energies [27].

1.3.1 Chemical Equilibrium

In high energy heavy-ion collisions, local equilibrium and collective behavior would be observed due to the large number of multiple scatterings. The particle ratios give us the properties of chemical equilibrium of the system since no more particles are produced after chemical equilibrium. The ratios of produced hadrons are well described by the simple statistical model, which is based on a grand canonical ensemble to describe the partition function, so that the particle density in an equilibrated system is given by,

$$n_i = \frac{g_i}{2\pi^2} \int_0^\infty \frac{p^2 dp}{\exp[(E_i \mu_i)/T_{\rm ch}] \pm 1} \tag{1.14}$$

where, n_i is particle density of particle i, g_i is spin degeneracy, p is momentum, E is energy, and $\mu_i = \mu_{\rm B} B_i - \mu_{\rm S} S_i - \mu_{\rm I_3} I_i^3$ is chemical potential. The quantities B_i, S_i, and I_i^3 denote the baryon, strangeness, and third-component of the isospin quantum numbers. In this model, the temperature $T_{\rm ch}$ and a baryon chemical potential $\mu_{\rm B}$ are independent.

Figure 1.5 shows the particle ratios in central collisions at $\sqrt{s_{\rm NN}} = 200$ GeV with thermal model prediction [12]. From the fitting results of particle ratios, chemical freeze-out temperature $T_{\rm ch} = 177 \pm 7$ MeV, and baryon chemical potential $\mu_{\rm B} = 29 \pm 8$ MeV are extracted. There is a good agreement between data and model.

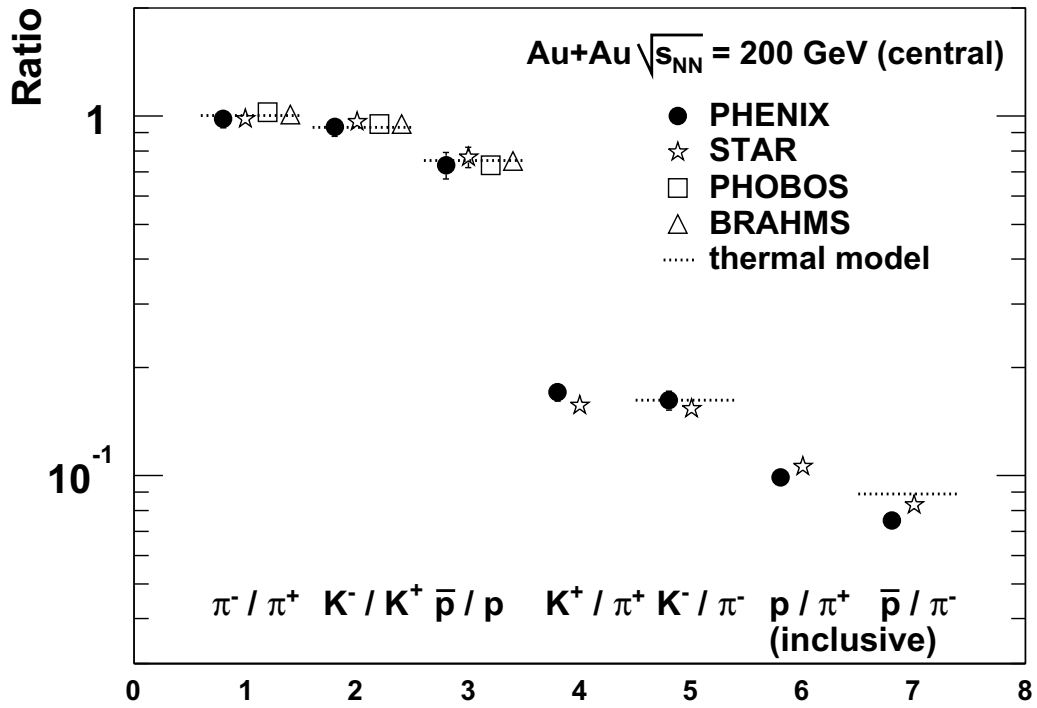

Figure 1.5: Particle ratios [58] in central collisions at $\sqrt{s_{\rm NN}} = 200$ GeV at mid-rapidity with thermal model prediction [12] compared with PHENIX, PHOBOS [13], BRAHMS [14], and STAR [15].

1.3.2 Kinematical Equilibrium and Collective Flow

After chemical freeze-out, the particle abundances are fixed but there are still elastic scatterings of hadrons in expanding system. Finally, the mean free path becomes comparable to the size of system at kinetic freeze-out temperature where momentum of hadron are fixed. Therefore, measured kinetic distributions of hadrons reflect the stage of kinetic freeze-out.

Transverse Mass Spectra

The produced hadrons reflect the condition of states in the reaction as well as the integrated effects for the system development of collisions. Therefore the transverse momentum spectra of hadrons are one of the common tools to study the collision dynamics. The spectra of identified particles are presented in terms of a Lorentz-invariant differential cross-section. The invariant cross-section for a particle which has four-momentum, (E, p_x, p_y, p_z), is given by,

$$E\frac{d^3\sigma}{dp^3} = E\frac{d^3\sigma}{dp_x dp_y dp_z}, \tag{1.15}$$

$$= \frac{d^3\sigma}{p_{\rm T} dp_{\rm T} dy d\phi_p}, \tag{1.16}$$

$$= \frac{1}{2\pi p_{\rm T}}\frac{d^2\sigma}{dp_{\rm T} dy}, \tag{1.17}$$

where, $p_{\rm T}$ is transverse momentum ($p_{\rm T} = \sqrt{p_x^2 + p_y^2}$), ϕ_p is the azimuthal angle, and y is rapidity ($y = \frac{1}{2}\ln\frac{1+\beta}{1-\beta}$). In low $p_{\rm T}$ region, the transverse mass spectra of single particle are well described by an exponential shape,

$$E\frac{d^3\sigma}{dp^3} = \frac{1}{2\pi p_{\rm T}}\frac{d^2\sigma}{dp_{\rm T}dy}, \tag{1.18}$$

$$= \frac{1}{2\pi m_{\rm T}}\frac{d^2\sigma}{dm_{\rm T}dy}, \tag{1.19}$$

$$\approx \exp(-m_{\rm T}/T), \tag{1.20}$$

where, $m_{\rm T} = \sqrt{m_0^2 + p_{\rm T}^2}$ is transverse mass, and m_0 is hadron mass. The inverse slope parameter, T corresponds to the temperature of kinetic freeze-out. In high energy p+p and p+A collisions, T is shown to be same among various particles such as pions, kaons, and protons ($T \approx 150$ MeV) [8]. This phenomenon is called "$m_{\rm T}$ scaling".

Radial Flow

In N+N collisions, the particle mass dependence is observed in inverse slope parameters [9]. Figure 1.6 shows the $m_{\rm T}$ spectra for pions, kaons, protons and anti-protons for central 0-5%, mid-central 40-50%, and peripheral 60-92% collisions [58]. The solid lines on each spectra are fitting result by using exponential functions. The inverse slope parameters for each particle are shown in Fig. 1.7. The values of the slope parameters depend on the particle mass and collided nucleus. The feature indicates the existence of the outward collective flow resulting from strong interaction of produced particles. If the particles have a common expanding velocity to transverse direction, the modified slope parameter is given by,

$$T \simeq T_f + \frac{1}{2}m\beta^2, \tag{1.21}$$

where, T_f is the thermal temperature, m is particle mass, and β is the collective radial flow velocity. From the results of experimental data, $T_f = 177.0 \pm 1.2$ MeV and $\beta = 0.48 \pm 0.07$ are extracted for most central collisions [48].

Elliptic Flow

The measurement of particle production in the azimuthal direction allows us the more valuable study through the collective motion in heavy ion collisions. When the mean free path is larger than the size of the system, the particle emission distribution becomes isotropic in the azimuthal direction. On the other hand, the mean free path is much shorter than the size of the system, the shape of system would be reflected to the azimuthal distribution of emitted particles.

In the non-central Au+Au collisions, the initial medium has the ellipsoidal shape in non-central collisions as shown in Fig. 1.8. Experimentally, the azimuthal anisotropy of emission particles has been studied using Fourier expansion of the azimuthal distribution as,

$$E\frac{d^3N}{dp^3} = N_0(1 + 2\sum_{n=1}^{\infty}[v_n\cos(n(\phi - \Psi))]), \tag{1.22}$$

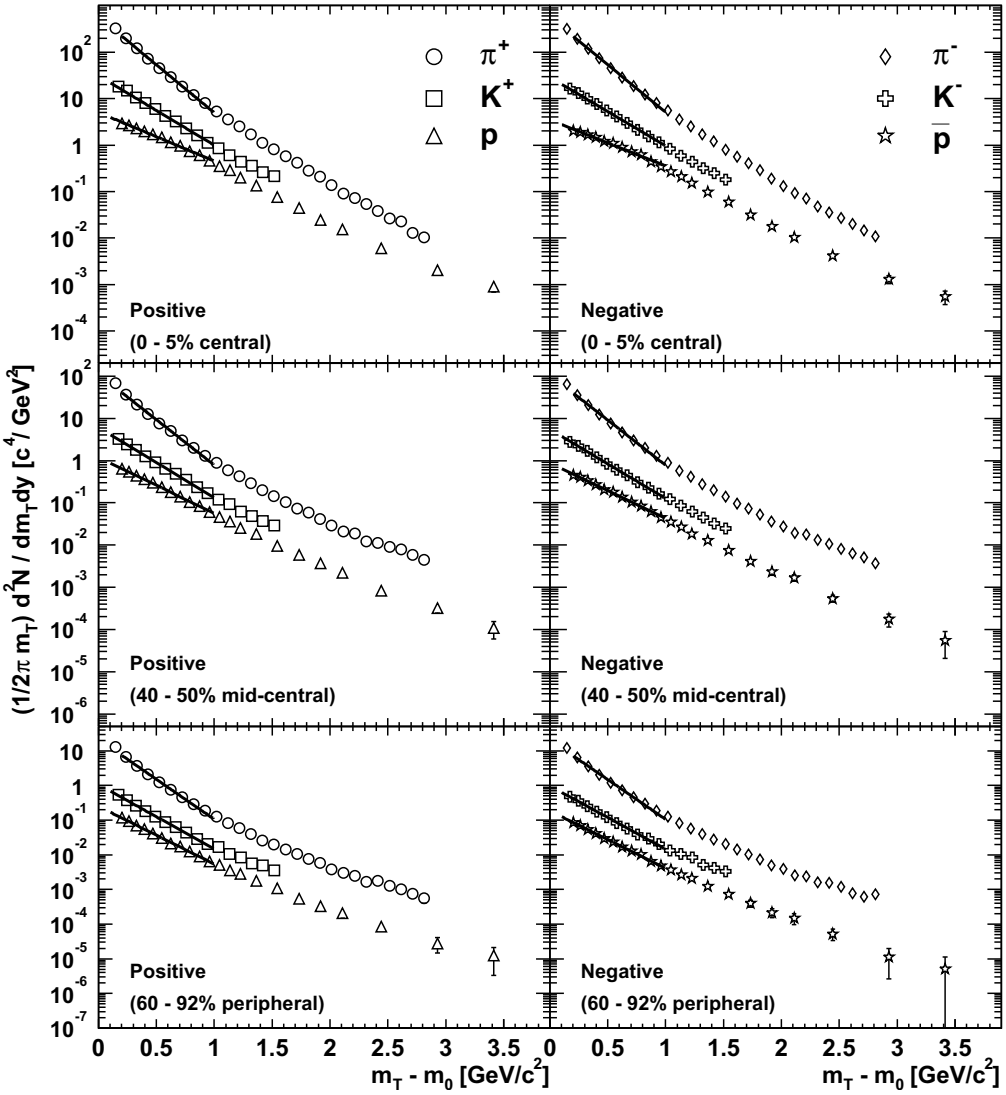

Figure 1.6: Transverse mass spectra for $\pi^{\pm}$, $K^{\pm}$, p, and $\bar{p}$ for three centrality selections in Au+Au collisions at $\sqrt{s_{\rm NN}}$ = 200 GeV [58]. The solid lines on each spectra are fitted results using $m_{\rm T}$ exponential function.

where, ϕ is azimuthal angle of emission particles and Ψ is angle of reaction plane which is defined by the impact parameter and beam axis direction. Particularly the second harmonic coefficient of the Fourier expansion, v_2, is sensitive to the geometry of collision region in the early stage of collisions, and it reflects the strength of elliptic flow.

At RHIC, strong azimuthal anisotropy has been observed, about twice larger than v_2 at SPS. Figure 1.9 shows the measured v_2 for identified $\pi^{\pm}$, $K^{\pm}$, proton and anti-proton as a function of $p_{\rm T}$. In low $p_{\rm T}$ region (< 1.5 GeV/c), v_2 increases with $p_{\rm T}$ and show the mass dependence, which is described well by hydrodynamical prediction [43]. This model assumes that the initial local equilibrium is occurred at 0.6 fm/c and the phase transition is the first-order phase transition with a freeze-out temperature of 120 MeV. In this model, the viscosity of the matter assumed

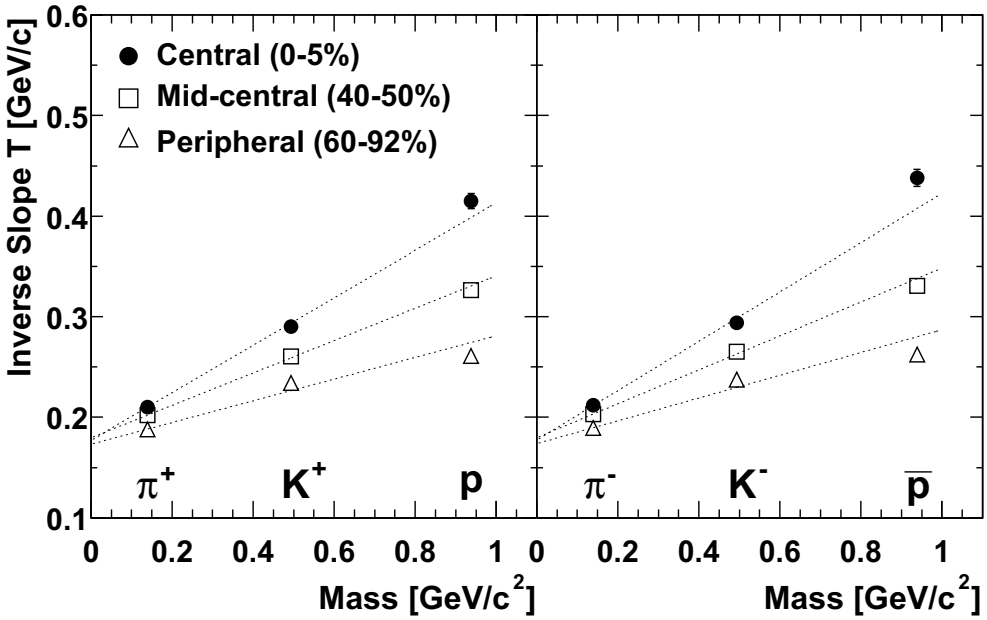

Figure 1.7: Mass and centrality dependence of inverse slope parameters T in Au+Au collisions at $\sqrt{s_{\rm NN}} = 200$ GeV.

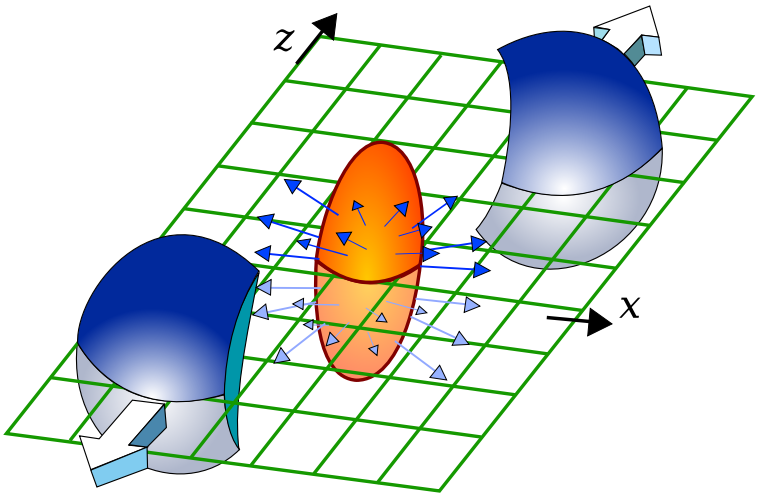

Figure 1.8: The ellipsoidal shape of participant in non-central high energy nucleus-nucleus collisions.

very low. Therefore, the property of the matter created in Au + Au collisions is expected as a perfect liquid.

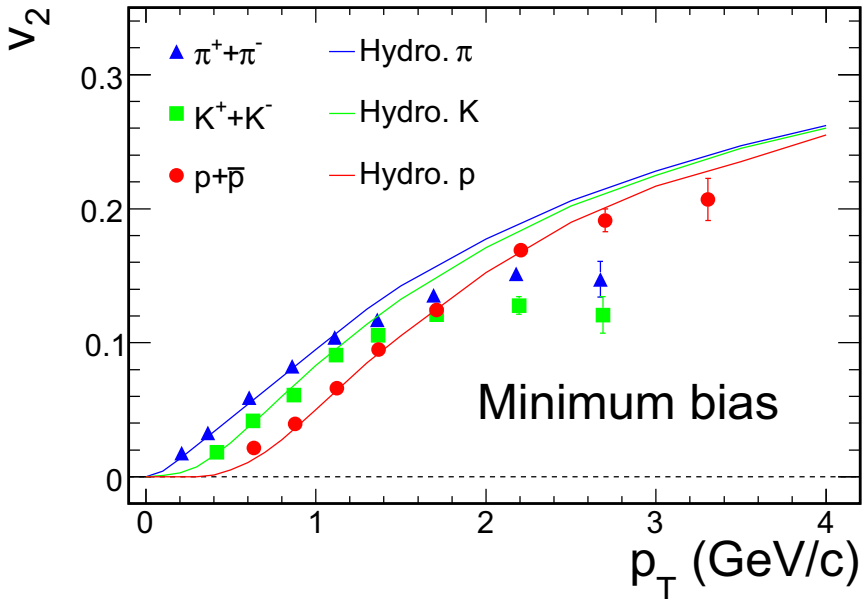

Figure 1.9: Measured identified charged particle v_2 as a function of p_{T} at $\sqrt{s_{\mathrm{NN}}} = 200$ GeV in central Au + Au collisions [33]. The curves on each point show the hydrodynamical prediction for each particle.

1.4 Direct Photon Production in Relativistic Heavy Ion Collisions

In high energy density state, observed hadrons suffer from the final-state interactions, which partially hide the significant information on the initial-stage of collisions. On the contrary, electromagnetic radiation is a powerful probe in the created matter at RHIC, because photons do not interact strongly with hot dense medium due to much larger mean free path. Especially, direct photon, which is defined as photons not originating from hadronic decay such as $\pi^0 \to 2\gamma$, will be directly carried out the information of thermodynamical and kinematical properties of produced matter.

1.4.1 Production Processes

Direct photon is emitted at every stage on the system development, such as the pre-equilibrium stage, the quark-gluon fluid, and the hot hadron gas stage. Observed direct photons are not able to identify their production sources experimentally, but the information of each generation is reflected into p_{T} spectra because photons do not interact strongly once produced. Therefore, the dominant source of photons would be investigated by using appropriate p_{T} window of the spectra of measured direct photon. Basically, there are three subprocesses for high p_{T} photon emissions in the parton-parton interaction: quark-gluon Compton scattering ($q + g \to q + \gamma$), quark-antiquark annihilation ($q + \bar{q} \to g + \gamma$), and Bremsstrahlung emission of photons from the quarks undergoing hard scattering as shown in Fig. 1.10. Direct photon emissions from various stages of developing system are usually further classified. This section describes the origin of

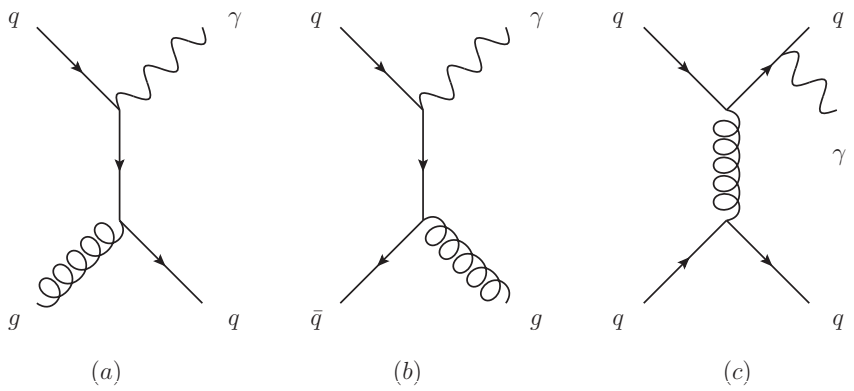

Figure 1.10: Feynman diagrams of the production subprocesses for photons: (a) quark-gluon Compton scattering, (b) quark-antiquark annihilation , (c) Bremsstrahlung.

each direct photon production in the heavy-ion collision experiments.

Direct Photon from Hard-Scattering

In nucleon-nucleon collisions, high-p_{T} particles are mainly emitted from hard scattering of partons with a large momentum transfer and fragmentation of quarks and gluons. Photons are also emitted from the hard scattering by Compton and annihilation process, and fragmentation of hard scattered partons in the initial stage of nucleon-nucleon collisions. The photons from hard scattering of partons are named as prompt photon. The process of direct photon production can be well described by the next-to-leading order perturbative QCD (pQCD) at high energy and high momentum transfer in p+p collisions. The cross section of direct photon in p+p collisions with large momentum transfer (Q) is given by,

$$\begin{aligned} \sigma_{\mathrm{p+p}}^{AB\to\gamma X} &= \sigma_{\mathrm{prompt}} + \sigma_{\mathrm{fragmentation}}, & (1.23)\\ &= \sum_{a,b,z} \int dx_a dx_b \cdot f_A^a(x_a, Q^2) \cdot f_B^b(x_b, Q^2) & (1.24)\\ &\times \left\{ \sigma(ab \to \gamma) + \int dz \sigma(ab \to z) \cdot D_z(x_z, Q^2) \right\}, \end{aligned}$$

where, $f_A^a(x_a, Q^2)$ ($f_B^b(x_b, Q^2)$) is the parton distribution function for parton a (b) in the nucleus A (B), and $D_z(x_z, Q^2)$ is fragmentation function from the parton z to photon. Figure 1.11 shows the measured cross section of direct photon at mid-rapidity in p + p collisions at $\sqrt{s} = 200$ GeV up to $p_{\mathrm{T}} = 24$ GeV/c . The cross section of direct photon is well described by NLO pQCD calculation in high p_{T} region.

Thermal Photon from QGP

In $N + N$ collisions, the thermal radiation would be emitted from thermalized system. The calculation of direct photon emissions from a thermalized QGP which is generated by heavy-ion collisions is an exercise in thermal field theory, which has been used since 1950's [35]. In the assumption as the net baryon density is equal to zero in the QGP so that the quark distribution

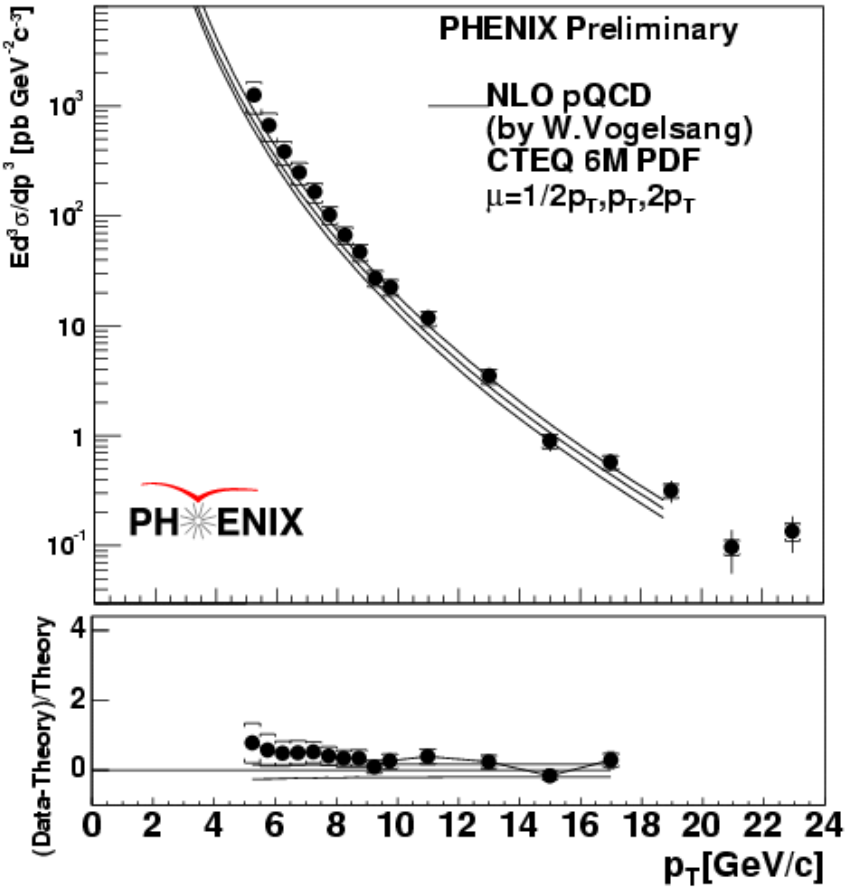

Figure 1.11: Direct photon cross section in $\sqrt{s} = 200$ GeV p + p collisions with NLO pQCD calculation.

$f_q(E)$ is corresponding to the antiquark distribution $f_{\bar{q}}(E)$. The thermal emission rate of photons with energy E and momentum p from a small system (compared to the photon mean free path) can be derived by following equation both perturbatively [24] and nonperturbatively [25]:

$$E_\gamma \frac{dR}{d^3p_\gamma} = \frac{-2}{(2\pi)^2} \mathrm{Im}\Pi_\mu^{R,\mu} \frac{1}{e^{E/T} - 1}, \tag{1.25}$$

where $\Pi_\mu^{R,\mu}$ is the retarded photon self-energy at finite T. It is valid to all orders in the strong interactions, but only to order e^2 in the electromagnetic interactions, as in the derivation it was assumed that the produced photons emitted from the matter without final-state scattering.

Thermal Photon from Hadron Gas

The calculation of the thermal photon spectrum from the hot and dense medium involves also the contribution from the hot hadron gas phase in the later stage of the expansion. The emission rate of thermal photons from the hadron gas can be described very similar to the QGP case. The different point is that π, η, and ρ mesons are treated as the constituted hadrons instead of quarks

and gluons. Figure 1.12 shows the examples of processes for the production of photons. The

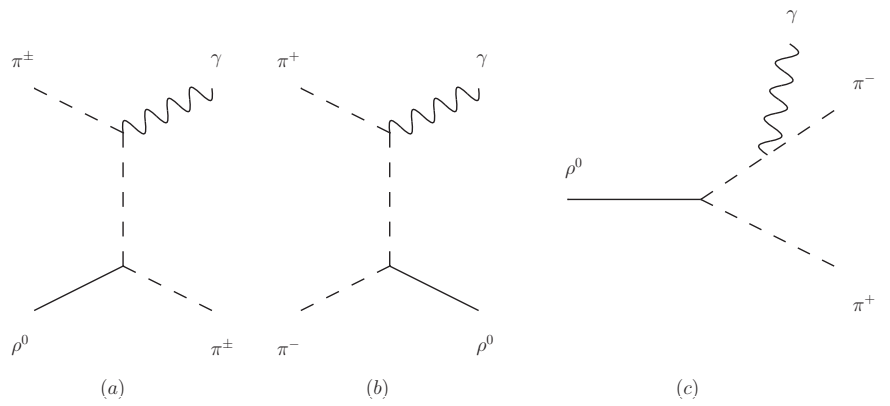

Figure 1.12: Examples of processes for the production of photons in a hadron gas: (a) Compton scattering, (b) annihilation, (c) ρ meson decay.

first estimate of the emission rate from a hadron gas has been presented in [26]. The thermal photon spectra from a hadron gas are similar to that from a QGP at the same temperature, but dominant p_{T} range would be slightly different from the total direct photon yield. Figure 1.13 shows the theoretical prediction for the mid-rapidity direct photon yield in central Au + Au collisions at RHIC energy. It is expected that thermal photon dominate the direct photon yield

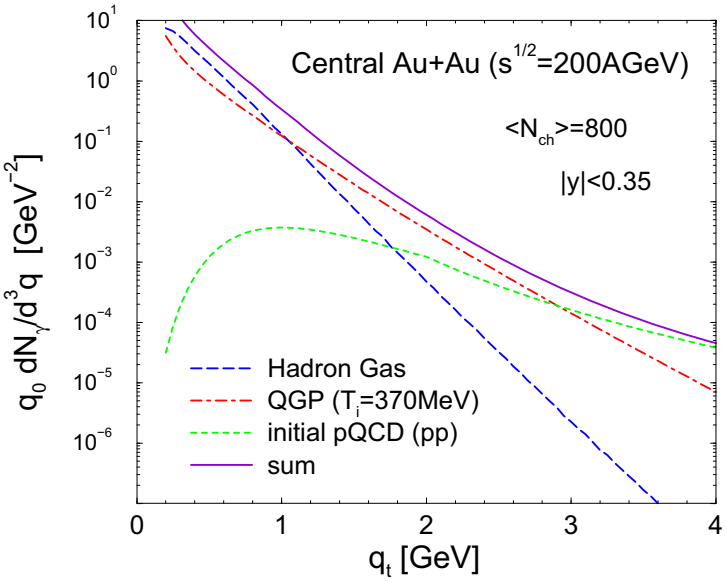

Figure 1.13: Theoretical prediction for thermal photon from QGP, thermal photon from hadron gas, and prompt photon (denoted as initial pQCD) [40] in central Au + Au collisions.

at low p_{T} region, and prompt photon is dominant at higher p_{T} .

Direct Photon from the Interaction Between Hard Scattered Partons And Hot And Dense Medium

Another production source of direct photons has been suggested in [44] which is emitted from the passing through the produced hard scattered partons in the hot and dense medium. As well as energetic charged particles lose their energy in charged medium due to the interaction with other charged particles, colored partons would lose their energy in colored medium due to the interaction with other partons via strong interaction. A hard scattered partons passing through the QGP will produce photons by Compton scattering with thermal gluons and annihilation with the thermal anti-quarks. As a attractive feature, photons resulting from this process would be reflected the jet properties because the leading hard scattered partons would formed jet after leaving collision area. Therefore photons originated from this process are named as "jet-photon conversion". On the other hand, photons would be also produced from parton energy loss in QGP by inelastic scattering. Photons resulting from parton energy loss in QGP are named as "jet-Bremsstrahlung photon".

The invariant yield of direct photon in high p_{T} including jet-photon conversion and jet-Bremss. photon processes is shown in Fig. 1.14 in central Au + Au collisions at $\sqrt{s_{\mathrm{NN}}} = 200$ GeV/c as a function of p_{T}.

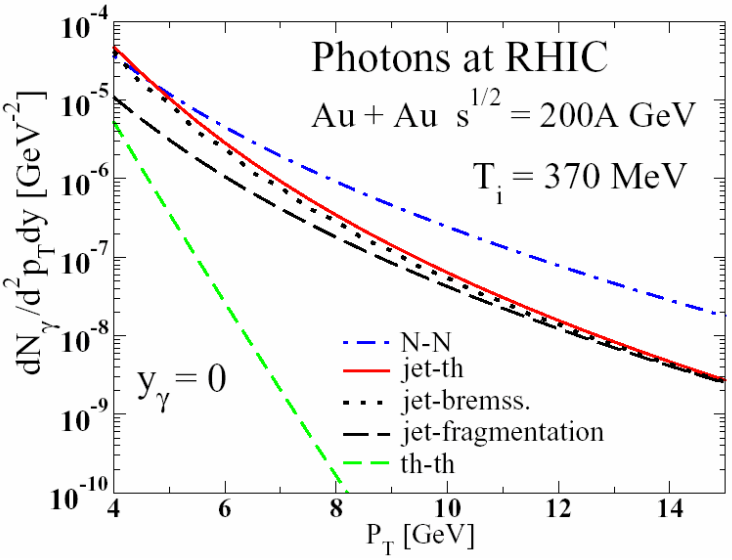

Figure 1.14: Theoretical prediction of direct photon spectra in Au + Au $\sqrt{s_{\mathrm{NN}}} = 200$ GeV/c as a function of p_{T} [40]. The prompt photon (N-N), jet-photon conversion (jet-th), jet-Bremsstrahlung photon (jet-Bremss.), photons from fragmentation of hard scattered parton (jet-fragmentation), and thermal photon (th-th) are drawn.

1.4.2 Invariant Yield of Direct Photon

Measurement of direct photon in heavy-ion collisions has been performed in the world experiments since CERN-SPS with various heavy-ion species and energies. High-p_{T} direct photon

invariant yield in Au + Au collisions at RHIC energy has been reported by RHIC-PHENIX experiment [29], and the result of direct photon measurement has been updated recently with large statistics. Figure 1.15 shows the direct photon invariant yield measured by subtracting the

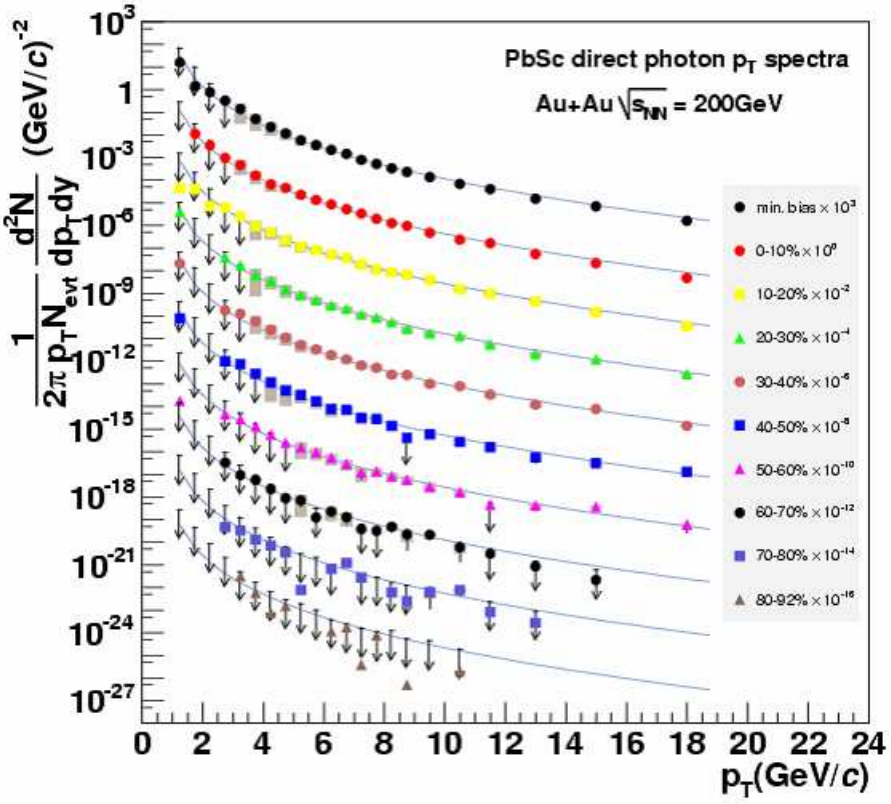

Figure 1.15: Direct photon invariant yield measured on PHENIX with PbSc EMCal (Sec. 2.6.1) in $\sqrt{s_{\rm NN}} = 200$ GeV Au + Au collisions for 9 centrality selections (as PHENIX preliminary result [63]). The solid curves are binary scaled NLO pQCD calculation.

hadronic decay photon from inclusive photon with binary scaled NLO pQCD calculation. The high $p_{\rm T}$ direct photon yield has a good agreement with the theoretical prediction curves.

1.4.3 Nuclear Modification Factor

The ratio between cross section yield in N+N collisions and number of binary scaled yield in A+A collisions indicates the nuclear medium effect. The nuclear modification factor is defined by,

$$R_{\rm AA} = \frac{d^2N_{\rm AA}/dp_{\rm T}d\eta}{T_{\rm AA}(b) \cdot d^2\sigma_{\rm NN}/dp_{\rm T}d\eta}, \tag{1.26}$$

where, $d^2N_{\rm AA}/dp_{\rm T}d\eta$ is the invariant yield in unit rapidity and $p_{\rm T}$ in A+A collisions, and $d^2\sigma_{\rm NN}/dp_{\rm T}d\eta$ is the cross section in the p + p collisions. $T_{\rm AA}(b)$ is Glauber scaling factor defined

as,

$$T_{\rm AA}(b) = \langle N_{\rm coll}\ (b) \rangle / \sigma_{\rm NN}, \tag{1.27}$$

where, b is impact parameter, and $\langle N_{\rm coll}\ (b) \rangle$ is the average number of binary nucleon-nucleon collisions at b. If the nuclear effect does not affect to the yield in $N + N$ collisions, $R_{\rm AA}$ should be equal to 1. Figure 1.16 shows the measured $R_{\rm AA}$ for direct photon, π^0, and η in $\sqrt{s_{\rm NN}}$ =

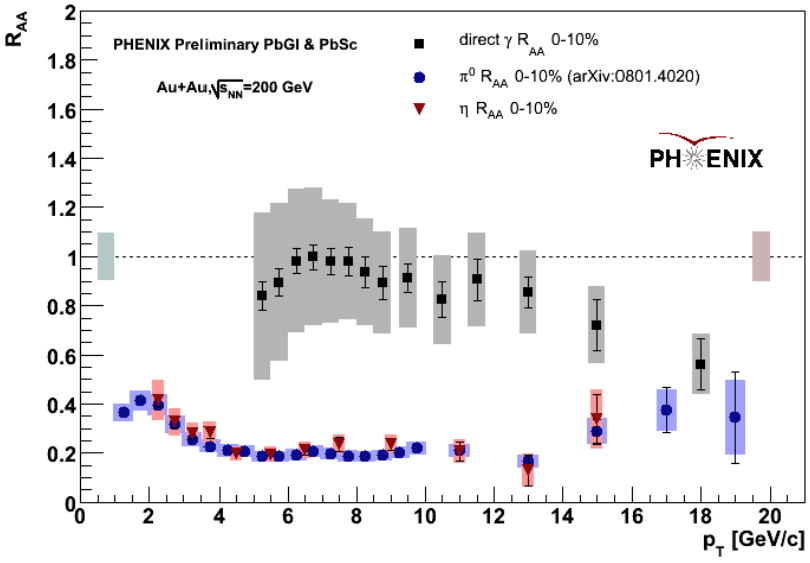

Figure 1.16: The $R_{\rm AA}$ of direct photon, π^0 , and η meson at $\sqrt{s_{\rm NN}} = 200$ GeV in central Au + Au collisions.

200 GeV Au + Au central collisions. In high-$p_{\rm T}$ region, suppression of hadron yields in A+A collisions is observed compared with the cross section in p+p. In A+A collisions, the yield of jets resulting from hard scattered partons is expected to be suppressed due to the energy loss by the multiple interactions passing through the extreme density matter. Therefore, $R_{\rm AA}$ would be observed less than 1 for emission hadrons. This phenomena is called "jet-quenching".

On the contrary, $R_{\rm AA}$ for direct photons is expected equal to 1 even high $p_{\rm T}$ since photons do not interact strongly with any other particles. At high-$p_{\rm T}$, prompt photon and jet fragmentation photon are considered as the dominant processes of direct photon production. If the contribution of jet fragmentation photon is large, nuclear effect would be not negligible even measurement of photon due to jet-quenching. According to the results of experimental measurement, yield in Au+Au collisions is corresponding to binary scaled cross section within error bar. Therefore, the experimental results suggest that the dominant source of high $p_{\rm T}$ direct photon is prompt photon.

1.4.4 Thermal Photon and Dilepton

The yield of thermal photon provides the various information of QGP, however it is difficult to measure the low-$p_{\rm T}$ direct photon spectra due to huge background of hadronic decay photons and worse energy resolution of detectors. Instead of direct measurement of real photons, an

alternative approach using low mass lepton pairs was introduced in 1970's at CERN ISR to set a limit on direct photon production [42], and is taken over at PHENIX experiment [45] [61].

In general, any source of high energy direct photons can also emit virtual photon which convert to low mass e^+e^- pairs. For instance, Compton scattering ($g+q \rightarrow g+\gamma$) produces high $p_{\rm T}$ real photon. A Feynman diagram of real photon in this process has an associated process of virtual photon production ($g+q \rightarrow g+\gamma^*$). The difference between real and virtual photon production processes is only the conversion of the virtual photon into an e^+e^- pairs, which is a pure QED process. Therefore, the yield of real photon production is able to related to the yield of the e^+e^- as,

$$\frac{d^3n_{ee}}{dmdp_{\rm T}dy} = \frac{2\alpha}{3\pi}\frac{1}{m}\sqrt{1-\frac{4m_e^2}{m^2}}\left(1+\frac{2m_e^2}{m^2}\right)S\frac{d^2n_\gamma}{dp_{\rm T}dy}, \tag{1.28}$$

where, α is fine structure constant, m is mass of e^+e^- pair, m_e is mass of electron, and S is a process dependent factor. If m is large compared with the electron mass m_e, this relation can be described simply as,

$$\frac{d^3n_{ee}}{dmdp_{\rm T}dy} = \frac{2\alpha}{3\pi}\frac{1}{m}\frac{d^2n_\gamma}{dp_{\rm T}dy}, \tag{1.29}$$

here, process dependent factor S goes to 1 as $m_{ee} \ll p_{\rm T}$.

Equation 1.28 also describes the relation between the photons originated from hadronic decay, and the e^+e^- pairs from Dalitz decays. The factor S for a hadrons is zero for $m_{ee} > M_h$. If we choose the mass region for $m_{ee} > M_{\pi^0} = 135$ MeV/c^2, the signal-to-background ratio for virtual photon greatly improves because $\sim$ 80 % of hadronic decay photons are resulting from π^0.

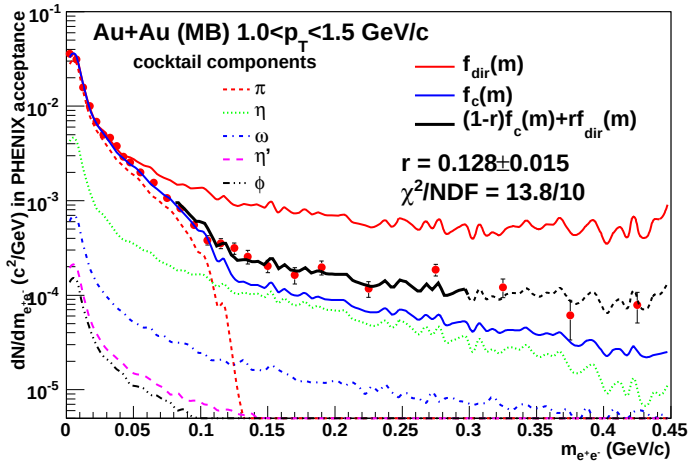

Figure 1.17: Mass distribution of e^+e^- at Au + Au minimum bias collisions for $1.0 < p_{\rm T} < 1.5$ GeV/c [45]. Two-component fit is applied to the experimental data from the shape of cocktail mass distribution and the expected direct photon via internal conversion. The fit range is 80 $< m_{ee} <$ 300 MeV/c^2. Distribution function for cocktail and direct photon is normalized to the experimental data for $m_{ee} <$ 30 MeV/c^2, separately.

Figure 1.17 shows the mass distribution of all electrons and positrons pairs with $p_{\rm T} > 0.2$ GeV/c in Au + Au collisions with expected yields of hadron decays estimated using a Monte Carlo

simulation. Other contributions of background in e^+e^- distribution such as $\pi^+\pi^- \rightarrow e^+e^-$ are expected small in low mass region ($m_{ee} < 450$ MeV/c^2). A two-component fit is applied to the measured distribution for estimation of the excess as,

$$f(m_{ee}) = (1-r)f_{\rm c}(m_{ee}) + r f_{\rm dir}(m_{ee}), \tag{1.30}$$

where, $f_{\rm c}(m_{ee})$ is the shape of background by cocktail, $f_{\rm dir}(m_{ee})$ is the expected shape of direct photon via internal conversion and r is the fraction of direct photon.

Figure 1.18 shows the fraction r of the direct photon determined by two-component fit in p + p and Au + Au respectively. The largest source of systematical error is the particle composition in

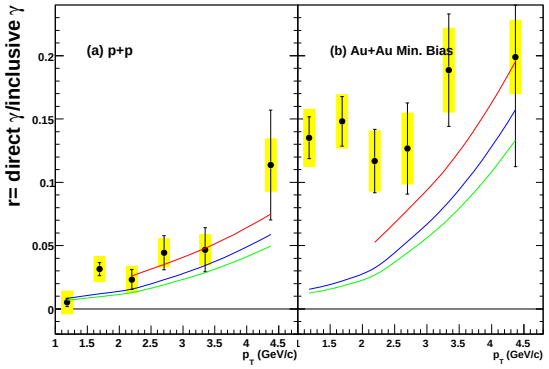

Figure 1.18: The fraction of direct photon and inclusive photon as a function of $p_{\rm T}$ in Au + Au minimum bias [45]. The theoretical prediction curves from NLO pQCD calculation are also shown.

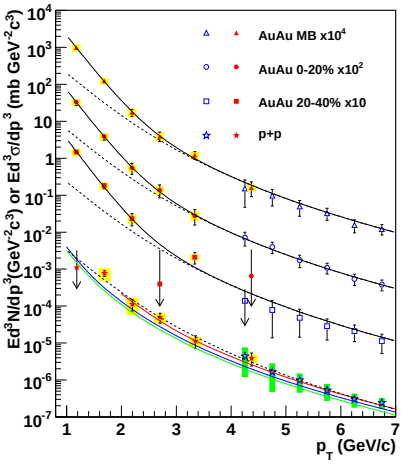

Figure 1.19: Invariant cross section of direct photon and invariant yield of Au + Au as a function of $p_{\rm T}$ [45]. The open symbols are calculated in [29] [30].

the hadronic cocktail. The η/π^0 ratio is estimated as 0.48 ± 0.08 at high $p_{\rm T}$ in PHENIX [31], it is corresponding to ∼ 17 % uncertainty in Au + Au cocktail for $100 < m_{ee} < 300$ MeV/c^2.

Since ratio of direct photon and inclusive photon using real photon is corresponding to the ratio using virtual photon, direct photon spectra is estimated from the yield of inclusive photon and fraction r,

$$\frac{N_\gamma^{\rm direct}}{N_\gamma^{\rm inclusive}} = \frac{N_{\gamma^*}^{\rm direct}}{N_{\gamma^*}^{\rm inclusive}}, \tag{1.31}$$

$$N_\gamma^{\rm direct} = \frac{N_{\gamma^*}^{\rm direct}}{N_{\gamma^*}^{\rm inclusive}} \cdot N_\gamma^{\rm inclusive} = r \cdot N_\gamma^{\rm inclusive}. \tag{1.32}$$

Figure 1.19 shows the direct photon spectra in low $p_{\rm T}$ region via e^+e^- analysis [45] in Au + Au with invariant cross section. The curves on the p+p data represent the theoretical predictions using a NLO pQCD calculation and dashed curves shows a modified power-law fit to the p+p data, scaled by Glauber nuclear overlap function for Au + Au .

As the result of exponential plus scaled p + p fitting (solid curves on Fig. 1.19), the inverse slope T of the exponential term is estimated as $T = 221 \pm 23(\text{stat}) \pm 18(\text{sys})$ MeV for central collisions.

1.4.5 Azimuthal Anisotropy of Direct Photon

As described in Section 1.3.2, a large azimuthal anisotropy has been observed at RHIC experiments for identified $\pi^{\pm}$, $K^{\pm}$, p, $\bar{p}$ [33], and π^0 [34]. In general, azimuthal anisotropy of hadrons indicates the final state of collisions rather than initial state in transverse space, since hadrons are produced when the temperature of system began to fall, and initial spatial anisotropy disappeared.

On the contrary, photons are emitted from every stage of system development and carried out the information of state of their production source, because they do not interact strongly with other particles. Since the azimuthal anisotropy of emission with respect to reaction plane depends on the purely spatial shape of hot and dense medium, azimuthal anisotropy measurement of direct photon is a powerful tool to investigate the photon source and system development.

The photons from initial hard scattering (prompt photon) are expected to show zero v_2 if they do not interact with the hot dense matter. The v_2 of photons from hard scattered parton fragmentation (jet-fragmentation photon) would make the similar v_2 to the hadron's v_2 because parton fragmentation is expected to occur in final state of collisions. Furthermore, jet-quenching effect (Section 1.4.3) would be observed in the high-p_{T} yield of jet-fragment photon. On the other hand, the photons resulting from energy loss of hard scattered parton in the hot dense medium caused by elastic scattering (jet-photon conversion photon) or Bremsstrahlung (jet-Bremsstrahlung photon) are expected to make negative v_2 because they are sensitive to the shape of hot and dense matter. The v_2 of photons from thermal radiation is expected to have small value but non-zero. Since the thermal radiation is expected to be emitted from both the QGP state and late hadron gas state, the v_2 is observed as total effect.

The expected processes and v_2 of direct photon emission is summarized in Table 1.2.

Table 1.2: Expected production process and v_2 of direct photon in high energy heavy-ion collisions.

name	emission phase	process	dominant p_{T}	anisotropy	v_2
prompt	initial state	hard-hard	high	none	$v_2 = 0$
thermal-QGP	QGP phase	soft-soft	middle	spatial expansion	$v_2 \geq 0$
thermal-hadron gas	hadronic gas phase	soft-soft	low	collective flow	$v_2 > 0$
jet-fragmentation	mixed phase	hard-soft	high	quenching	$v_2 > 0$
jet-photon conversion	mixed phase	hard-soft	high	path length	$v_2 < 0$
jet-Bremsstrahlung	mixed phase	hard-soft	low	path length	$v_2 < 0$

In Table 1.2, the initial hard scattering and the interaction process of hard scattered partons

are denote as "hard", the others denotes as "soft". We focus on these 6 entries as production processes of direct photon in heavy-ion collisions for the following discussions in this thesis.

Theoretical predictions of direct photon v_2 have been performed in [32] for low-p_{T} and [41] for high-p_{T}. Figure 1.20 and 1.21 show the predicted v_2 of direct photon in mid-central $\mathrm{Au}+\mathrm{Au}$ collisions at $\sqrt{s_{\mathrm{NN}}} = 200$ GeV as a function of p_{T} .

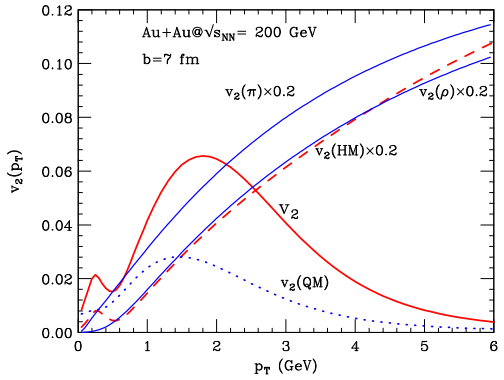

Figure 1.20: Theoretical prediction curve of low-p_{T} direct photon v_2 in mid-central $\mathrm{Au}+\mathrm{Au}$ collisions at $\sqrt{s_{\mathrm{NN}}} = 200$ GeV [32]. The contribution of quark matter flow and hadronic matter are shown respectively. In addition, the scaled v_2 of π and ρ are also shown for comparison.

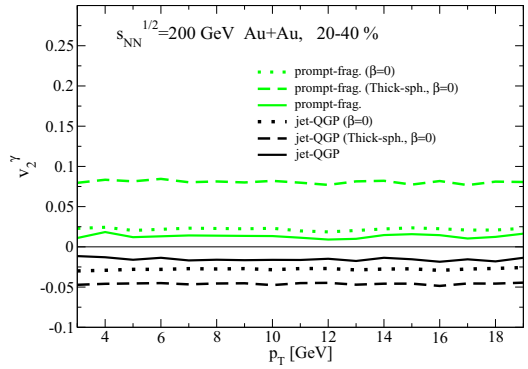

Figure 1.21: Theoretical prediction curves of high-p_{T} direct photon v_2 in mid-central $\mathrm{Au}+\mathrm{Au}$ collisions at $\sqrt{s_{\mathrm{NN}}} = 200$ GeV [41]. The jet-fragmentation photon denotes "prompt-frag", and the jet-photon conversion photon denotes "jet-QGP" in this figure. The influence of the thick sphere geometry for photon production from jets and flow dynamics are also examined.

1.5 Thesis Motivation

The extreme high temperature and energy density has been realized in heavy-ion collisions at the Relativistic Heavy-Ion Collider (RHIC) since 2000. The primary goal of RHIC is the experimental study of the QCD phase transition. Studies are now possible for the most basic interactions predicted by QCD at high energy densities enough to excite the expected phase transition to QGP. RHIC experiments have provided the various signatures of QGP, such as strong anisotropic collective flow of hadrons [33] and suppression of high-p_{T} hadron yields [28].

The space-time development of hot and dense medium which is generated by heavy-ion collisions involves the complicated processes, however we are only able to observe the emitted particles experimentally at the final state of system development, mainly using hadron measurements. On the contrary, photons emitted from heavy-ion collisions carry out the information of their produced state because photons do not interact strongly with any other hadrons (their mean free path is approximately 20 times larger than quarks one). Especially, photon emissions from early stage of collisions are a powerful probe to explore the properties of initial state of hot and dense medium.

In the nucleus-nucleus collisions, the ellipsoidal shape and anisotropic pressure gradient of participant part non-central collisions makes an azimuthal anisotropy distribution of emission particle yields with respect to reaction plane. As the penetrating property of photons, azimuthal anisotropy of direct photon allows us more reliable study of QGP and hot and dense medium since photons are emitted from every stage of system development, and reflected the state of production source in the extreme density matter to azimuthal distributions.

In this thesis, the contributions of direct photon emission is categorized into 6 sources according to production processes as summarized in Section 1.4.5. From the results of R_{AA} analysis, strong suppression is observed in high-p_{T} hadrons [28], while non-suppression is observed in direct photon yield [63]. This results indicate that there is no nuclear effect in high-p_{T} direct photon. Therefore, we concluded the dominant source of direct photon production in high-p_{T} is initial parton-parton hard-scattering (prompt photon). This statement is expected to be established in direct photon v_2 analysis. We will discuss about dominant source in high-p_{T} from the experimental results of direct photon v_2. Furthermore, photons resulting from jet-fragmentation and jet-photon conversion have opposite sign of v_2 in high-p_{T} , more detailed structure might be revealed by precise v_2 measurement. Contribution ratios of high-p_{T} direct photon from prompt, jet-fragmentation, and jet-photon conversion will be argue by using measured v_2. Recently, low-p_{T} direct photon invariant spectra are measured at RHIC-PHENIX via internal conversion of dilepton [45], and presented the significant statement about established temperature in initial state. Since the accuracy of direct photon to inclusive photon ratio estimated from virtual photon is better than real photon analysis, the v_2 in low-p_{T} is also expected to improve. Direct photon v_2 in low-p_{T} will improve by using the ratio of direct photon and inclusive photon estimated by virtual photon analysis.

In this thesis, we present the v_2 measurement of neutral pion and direct photon as a function of transverse momentum p_{T} with various centrality selections in $\sqrt{s_{\mathrm{NN}}} = 200$ GeV $\mathrm{Au}+\mathrm{Au}$ collisions at RHIC-PHENIX.

Chapter 2

Experiment

2.1 RHIC

The Relativistic Heavy Ion Collider (RHIC) at Brookhaven National Laboratory (BNL) is a world class scientific experimental facility that began operation in 2000. One of the main physics topics in RHIC is the study of extreme energy density which is enough even to create the Quark Gluon Plasma (QGP). RHIC is the first machine in the world capable of colliding heavy ions which accelerated to 200 GeV at each nucleons.

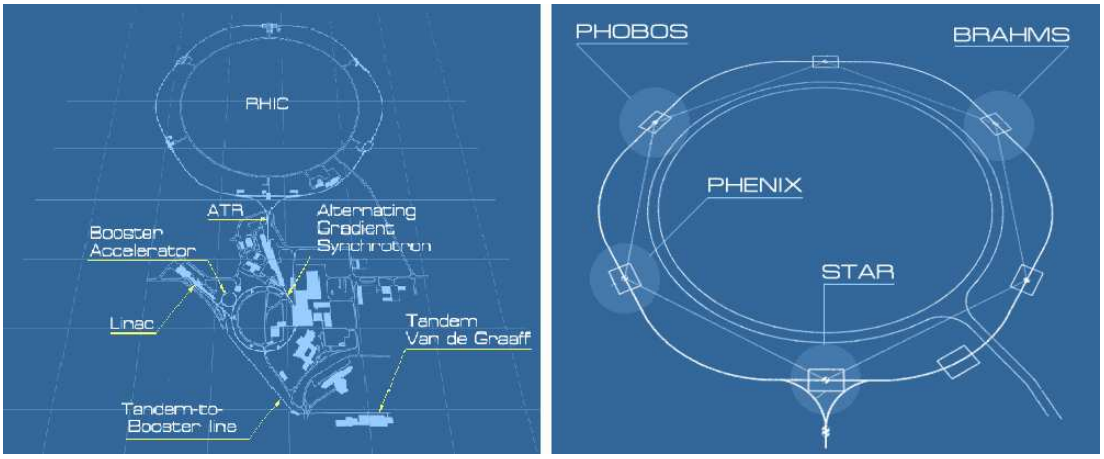

Figure 2.1: (Left) The accelerator facilities in BNL. (Right) The layout of interaction points and experiments at RHIC.

RHIC drives two beams of gold nuclei to opposite direction at 99.95% the speed of light. Accelerated two beams appear flat shape, instead of spherical, due to the Lorenz contraction which occur at such speeds. The two beams intersect at six intersection points, smashing into one another and then passing through each other. Some of energy they had before the collision is transformed into intense heat and new particles.

If the collision region has enough deposited energy for transition to QGP, quark and gluon are liberated from strong interaction of their nucleons just after collisions. In the QCD calculation, the first observation of QGP on the earth is achieved in heavy ion collisions at RHIC. Since theory predicted that there were free quark and gluon at the beginning of the universe, RHIC is

the one of instrument to study how matter behaved at the early stage of universe.

Nuclei receive initial acceleration by several boosters before RHIC (Fig. 2.1). At first, atoms are removed their outer cloud of electrons by Tandem Van de Graaff which uses static electricity, then remains which call nuclei have a strong positive charge. Nuclei are accelerated to 1 MeV energy by Tandem, sending them on their way towards the Booster along to Tandem-to-Booster line. At this point, they are traveling at about 5% the speed of light. After leaving Tandem-to-Booster line, nuclei are accelerated to 95 MeV at each nucleons by the Booster Synchrotron which is a powerful and compact circular accelerator. And then, boosted beams of heavy ion are sent to the Alternating Gradient Synchrotron (AGS). In the AGS, nuclei from the booster get more energy, then they are traveling at 99.7% the speed of light. Beams of accelerated nuclei until top speed by AGS take down another beam line called the AGS-to-RHIC (ATR) sending to RHIC. At the entrance of RHIC, there are two beam lines with opposite direction and settled two magnets. Beams are selected their directions by these magnets, traveling to opposite directions each other, then collide into one another at interaction points in 200 GeV energy at each nucleons.

At interaction points, the emitted particles from the collisions are detected by RHIC's experimental detectors. The four current experiments are proceeded, called STAR, PHENIX. PHOBOS, and BRAHMS (Fig. 2.1).

RHIC operates for taking the physics data from winter to early spring among the several kinds of collision particles and energies. And the maintenance and installation of new subsystems are performed during the rest period. A typical RHIC performance is shown in Table 2.1. And the collision species, energy, and integrated luminosity at PHENIX are summarized in Table 2.2.

Table 2.1: The performance at RHIC for heavy-ion collisions.

Injection energy	9.5 GeV/c/nucleon
Storage energy	100.0 GeV/c/nucleon
Bunch intensity	1.0×10^9 Au ions/bunch
Number of bunches	56 filled bunches
Interaction diamond length	20cm
Bunch length	15cm

Table 2.2: Experiment summary at RHIC.

Run	Species	$\sqrt{S_{NN}}$ (GeV)	$\int Ldt$	N_{tot}	Year
01	Au + Au	130	1 μb^{-1}	10 M	2000
02	Au + Au	200	24 μb^{-1}	170 M	2001/2002
	p + p	200	0.15 pb^{-1}	3.7 G	
03	d + Au	200	2.74 nb^{-1}	5.5 G	2002/2003
	p + p	200	0.35 pb^{-1}	6.6 G	
04	Au + Au	200	241 μb^{-1}	1.5 G	2003/2004
	Au + Au	62.4	9 μb^{-1}	58 M	
	p + p	200	0.35 pb^{-1}	6.6 G	
05	Cu + Cu	200	3 nb^{-1}	8.6 G	2004/2005
	Cu + Cu	62.4	0.19 nb^{-1}	0.4 G	
	Cu + Cu	22.5	2.7 μb^{-1}	9 M	
	p + p	200	3.8 pb^{-1}	85 G	
06	p + p	200	10.7 pb^{-1}	230 G	2005/2006
	p + p	62.4	0.1 pb^{-1}	28 G	
07	Au + Au	200	813 μb^{-1}	5.1 B	2006/2007

2.2 Overview of PHENIX experiment

The PHENIX, the Pioneering High Energy Nuclear Interaction eXperiment, is one of the largest experiments that have taken data at the RHIC. The primary goal of PHENIX is to study the physics properties of hot and dense matter and detect the Quart-Gluon Plasma. The PHENIX is designed specifically to measure direct probes of the collisions such as hadrons, leptons and photons with good resolution.

The PHENIX detectors are composed of two central arms, two muon arms, event characterization detectors and a set of three huge magnets. Central arms which settled in mid-rapidity consist of tracking detectors (Pad Chambers (PC), Drift Chambers (DC)) and particle identification detectors (Time-of-Flight (TOF), Electro Magnetic Calorimeters (EMCal), Ring Imaging Cerenkov detectors(RICH)). In forward-rapidity, muon detectors are placed on the muon arms in order to provide the position, momentum and identification of muon particles. The global detectors which provide the event characterized values such as a collision time, vertex position, event trigger, and centrality are consist of Beam-Beam Counters (BBC) and Zero Degree Counters (ZDC). In addition, the Reaction Plane detectors (RxNP) have been installed since RHIC Year-7 for the improvement of performance of reaction plane determination which have better resolution compared to that by using BBC only. The PHENIX detector subsystems used in this thesis are summarized in Table 2.3, and detector configuration is shown in Fig. 2.2.

Table 2.3: Summary of the PHENIX detector subsystems.

Component	$\Delta\eta$	$\Delta\phi$	Purpose and Special Feature
Magnet: central (CM)	$\|\eta\|$ <0.35	360°	Up to 1.15 T·m
muon (MMS)	-1.1 to -2.2	360°	0.72 T·m for η=2
muon (MMN)	1.1 to 2.4	360°	0.72 T·m for η=2
BBC	$3.0 < \|\eta\| < 3.9$	360°	start timing, fast vertex
ZDC	±2 mrad	360°	Minimum bias trigger
DC	$\|\eta\| < 0.35$	90°×2	Good momentum and mass resolution
			$\Delta m/m$=0.4% at m=1.0 GeV
PC	$\|\eta\| < 0.35$	90°×2	Pattern recognition,
			tracking for nonbend direction
RICH	$\|\eta\| < 0.35$	90°×2	Electron identification
TOF	$\|\eta\| < 0.35$	45°	Good hadron identification, σ_{TOF} ~120ps
PbSc EMCal	$\|\eta\|$ <0.35	90°+45°	For both calorimeters, photon and
			electron detection
PbGl EMCal	$\|\eta\|$ <0.35	45°	Good $e^{\pm}/\pi^{\pm}$ separation $p > 2.0$ GeV/c
			by EM shower and $p < 0.35$ GeV by TOF
			$K^{\pm}/\pi^{\pm}$ separation up to 1 GeV/c by TOF
μ tracker(μTS)	-1.15 to -2.25	360°	Tracking for muons
μ tracker(μTN)	1.15 to 2.44	360°	Muon tracker north installed for Year-3
μ identifier(μIDS)	-1.15 to -2.25	360°	Steel absorbers and Iarocci tubes for
μ identifier(μIDN)	1.15 to 2.44	360°	muon/hadron separation
RxNP	$1.0 < \|\eta\| < 2.8$	360°	Good resolution for reaction plane

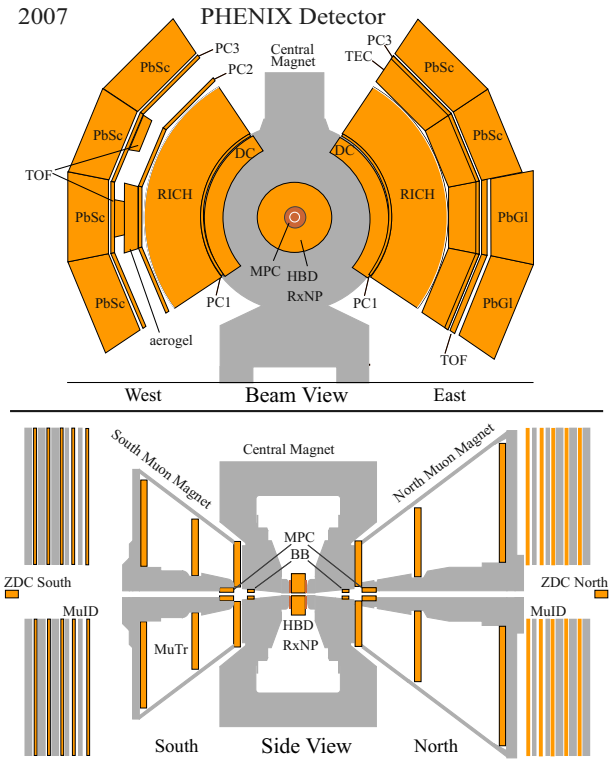

Figure 2.2: Detector configuration of PHENIX detectors at Year-7.

2.3 Beam Beam Counter

The Beam-Beam Counter (BBC [17]) are installed on both north and south sides of the collisions point along the beam axis. The north BBC (BBCN) and south BBC (BBCS) are located at 144 cm away from the center of the interaction point and covered a pseudo-rapidity range from 3.0 to 3.9 over the full azimuth. Since the BBC is placed in a very high-level radiation area and magnetic field around the beam pipe, it is required to work well in a high radiation and a magnetic field environment. The main role of BBC for physics experiment is to provide following information,

- the trigger signal for the PHENIX Local Level-1 (Sec. 2.8.1),
- the collision vertex point along the beam axis and the collision time,
- the centrality (Sec. 3.2) and the azimuthal angle of reaction plane (Sec. 3.3).

Each counter consists of 64 one-inch diameter mesh-dynode photomultiplier tubes (Hamamatsu R6178) equipped with 3 cm quartz on the head of the PMT as a Cherenkov radiator. Figure 2.3 shows one BBC array composed of 64 BBC elements and the single BBC counter element. The number of charged particles for a central Au+Au collisions at $\sqrt{s_{NN}} = 200$ GeV is expected to hit 15 particles per BBC element. The monitoring and calibration for individual BBC elements are provided by laser signal which is also used for Time-of-Flight and Electromagnetic Calorimeter (Sec. 2.6).

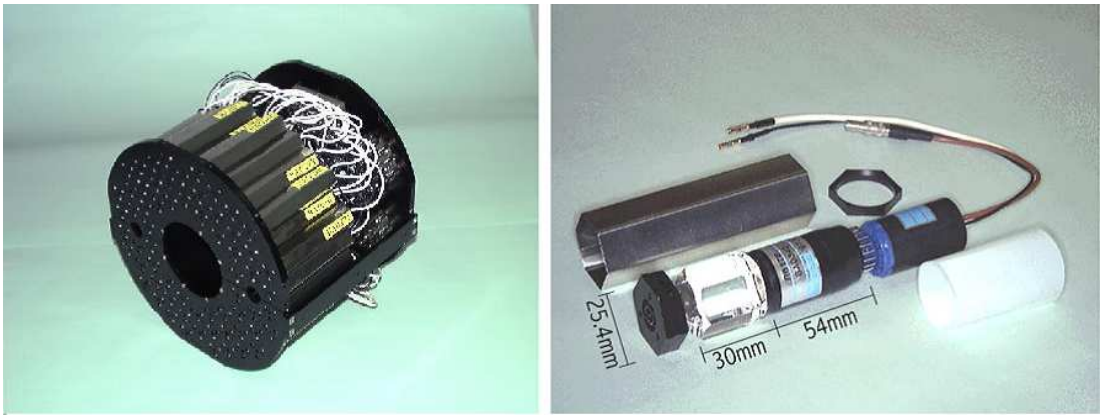

Figure 2.3: (Left) One BBC array comprising 64 elements. (Right) Single BBC counter composed of one-inch mesh dynode photomultiplier tubes equipped with a 3 cm quartz radiator.

The front-end electronics for BBC consist of discriminators, pre-amplifiers, TVC (Time-to-Voltage Converters), and flash ADC (Analog-to-Digital Converters). The measured timing and pulse height of each collision event are stored in digital buffer memories. The gains of BBC elements are calibrated by using the MIP peak in the pulse height distribution. Typical MIP peak of PHENIX BBC elements are appeared at approximately 75 pC.

The collision time and vertex position are reconstructed from the arrival time of leading charged particles for BBCN and BBCS. The systematic shifts caused by the time walk of the

discriminator and time offset are adjusted for each individual BBC element. The collision time (T_0) and vertex position (z_{vtx}) are given by,

$$T_0 = (T_{\mathrm{BBCN}} + T_{\mathrm{BBCS}})/2, \quad (2.1)$$

$$z_{vtx} = c \cdot (T_{\mathrm{BBCN}} - T_{\mathrm{BBCS}})/2, \quad (2.2)$$

where, T_{BBCN} and T_{BBCS} are the corrected average timing and c is the speed of light. The typical timing resolution of BBC is 40 ps, and vertex position is 0.6 cm.

2.4 Zero Degree Calorimeter

The Zero Degree Calorimeter (ZDC [18][19]) is small transverse-area hadron calorimeter with an angular acceptance of $|\theta| < 2$ mrad which is placed in the beam line behind magnets. The main

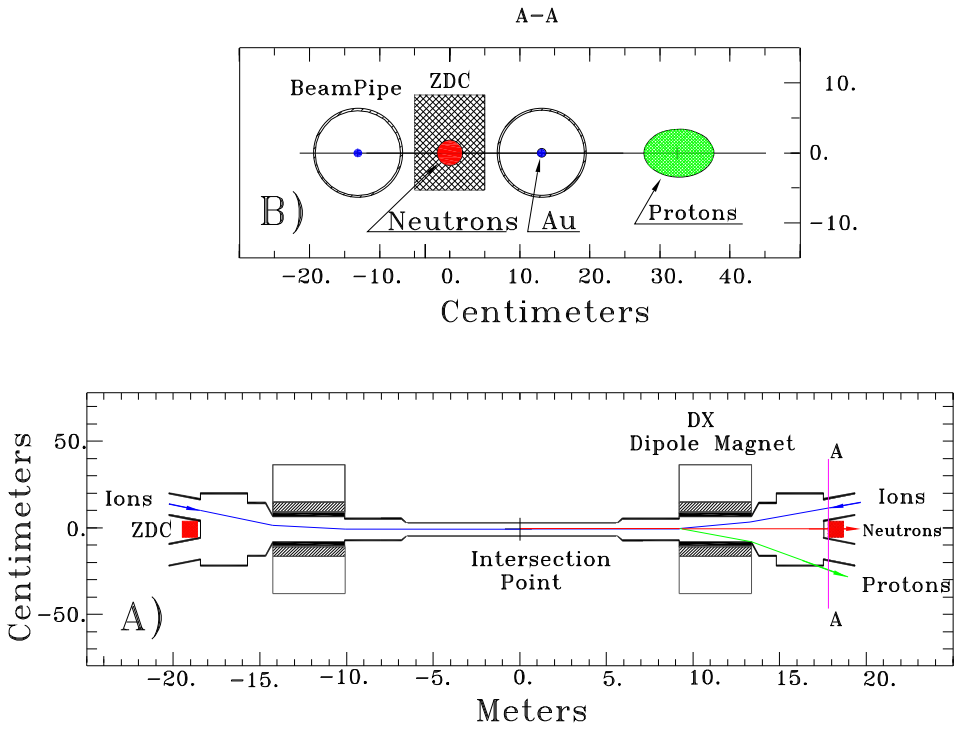

Figure 2.4: (A) The ZDC location view of along the beam axis. The north ZDC and south ZDC are located in $\sim$ 18m from interaction point and covered full azimuth. (B) The indication of deflection for neutrons, Au ions, and protons [18].

purpose of ZDC is to detect the unbound neutrons emitted within the ZDC acceptance along beam directions which corresponds to $|\eta| > 6$, and measure their total energy. The coincidence of detectors placed in north ZDC (ZDCN) and south ZDC (ZDCS) provides a minimum bias trigger and a luminosity monitor of heavy ion collisions. Charged particles in the beam fragments are deflected out from the ZDC acceptance by the beam bending magnet leading to a detection of neutrons with good resolution. Figure 2.4 shows the location view of along the beam axis (A),

and top view (B) indicating deflection of neutrons, Au ions, and protons.

Each ZDC module is composed of Tungsten plates and ribbons of optical fibers in the sampling layer. These fibers generate the collect the Cherenkov lights to a PMT. Figure 2.5 shows the mechanical design of the ZDC module.

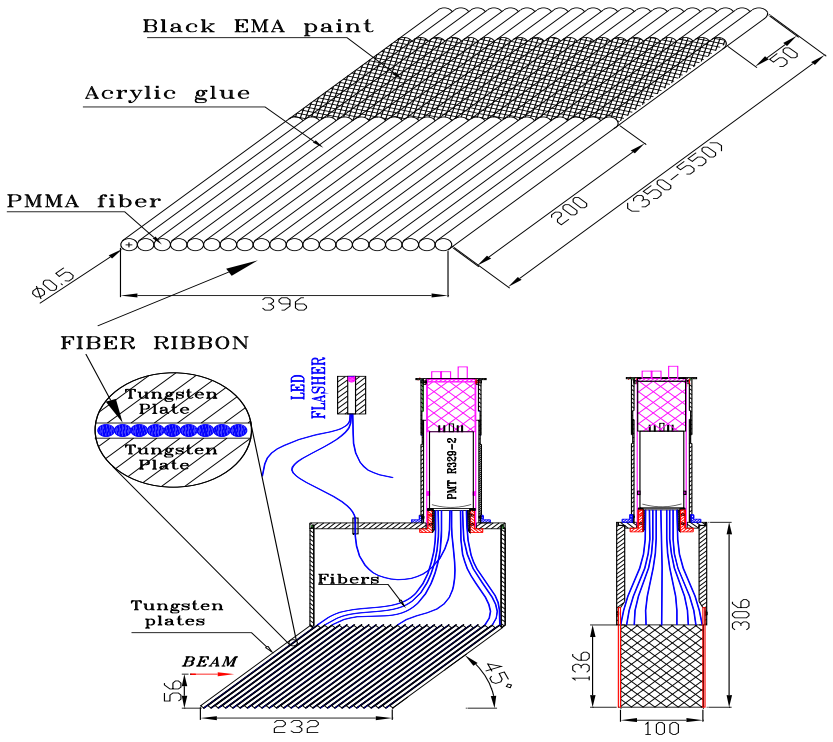

Figure 2.5: Mechanical design of the ZDC module. Dimensions are shown in mm [18].

2.5 Pad Chamber

The Pad Chamber (PC [21]) is multi-wire proportional chamber. The three layers of pad chambers are installed in the central arm for charged particle tracking. Figure 2.6 shows the geometry view of the pad chamber, drift chamber (DC), and time expansion chamber (TEC).

The first layer, called PC1, has 8 chambers in each arm placed 2.5m from the interaction region where behind the DC and in front of the RICH. The second and third layers (PC2 and PC3) are placed behind the RICH, on both sides of the TEC. The total area of the PC in the central arms exceeds 100m^2.

A size of segmentation of the cathode readout (cells) is 8×8mm^2 (Fig. 2.7(a)), and the pad size corresponds to 3×3 cells. Each pad has been divided into nine copper electrodes, called pixels, connected each other (Fig. 2.7(d)). By shifting the three pads by one cell relative to each other in both layers, each cell belonging to three different pads without geometrical overlap (Fig. 2.7(c)). Because of charge sharing among three pads in each cell, the number of channels are

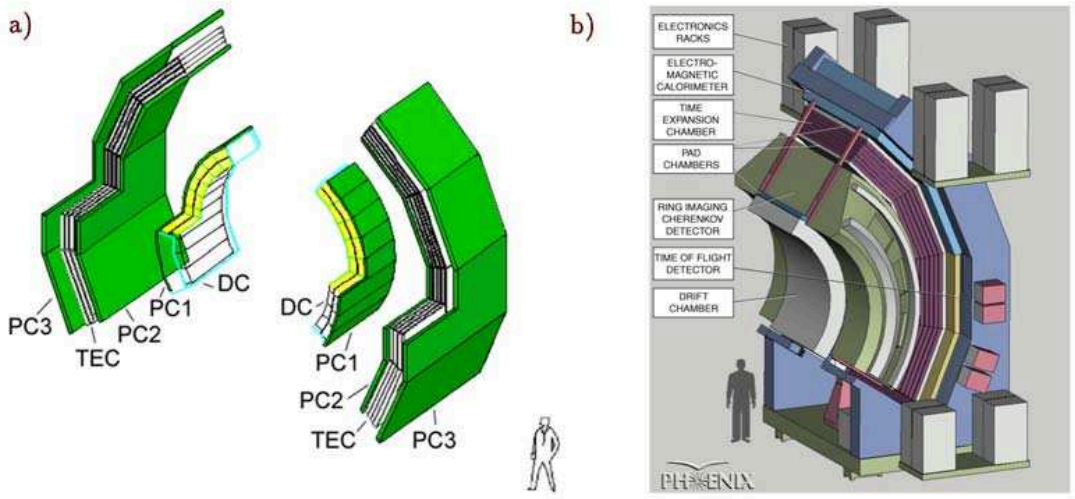

Figure 2.6: (A) The geometry view of the pad chamber, drift chamber, and time expansion chamber. (B) The geometry view of east arm with all subsystems [20].

able to be decreased while keeping the position resolution of such a system (Fig. 2.7(b)). The width of a pixel is selected that the same amount of charge is detected, since the center pixels would sense a larger charge than the side pixels. The position resolution for z direction of PC1, PC2, and PC3 is about 1.7mm, 3.1mm, and 3.6mm respectively.

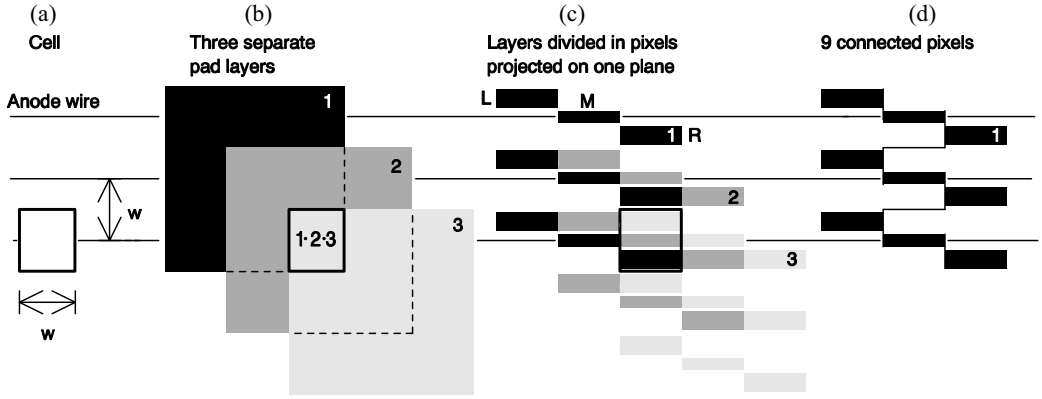

Figure 2.7: The layout of the PHENIX pad chamber [21].

2.6 Electromagnetic Calorimeter

The PHENIX Electromagnetic Calorimeter (EMCal) provides a measurement of the energies and spatial positions photons and electrons produced in heavy ion collisions. The EMCal system consists of two type detectors. One is the Lead-Scintillator calorimeter which provides six sectors of azimuthal coverage and another is the Lead-Glass calorimeter comprised of two sectors. The properties of the two detectors are very different, which the Lead-Scintillator is a sampling

calorimeter while the Lead-Glass is a Cherenkov detector. For example the Lead-Glass has the better granularity and energy resolution but the Lead-Scintillator has the better linearity and timing and the response to hadrons is better understood.

2.6.1 Lead-Scintillator Calorimeter

The Lead-Scintillator Calorimeter is a shashlik type sampling calorimeter consisting of 15552 individual towers. Each tower is composed of 66 sampling cells consisting of alternating tiles of lead and scintillator. These cells are optically connected by 36 fibers to collect the light to phototubes at the back of towers. Four towers are mechanically brought together, and form a module. Thirty six modules are attached to a backbone and held together by welded stainless steel skins on the outside to form a rigid structure called a super-module. Eighteen super-modules make a sector, a $2 \times 4\text{m}^2$ plane with its own rigid steel frame. Details of the design and methods of construction of the Lead-Scintillator modules have been given in [36]. Parameters for Lead-Scintillator are summarized in Table 2.4.

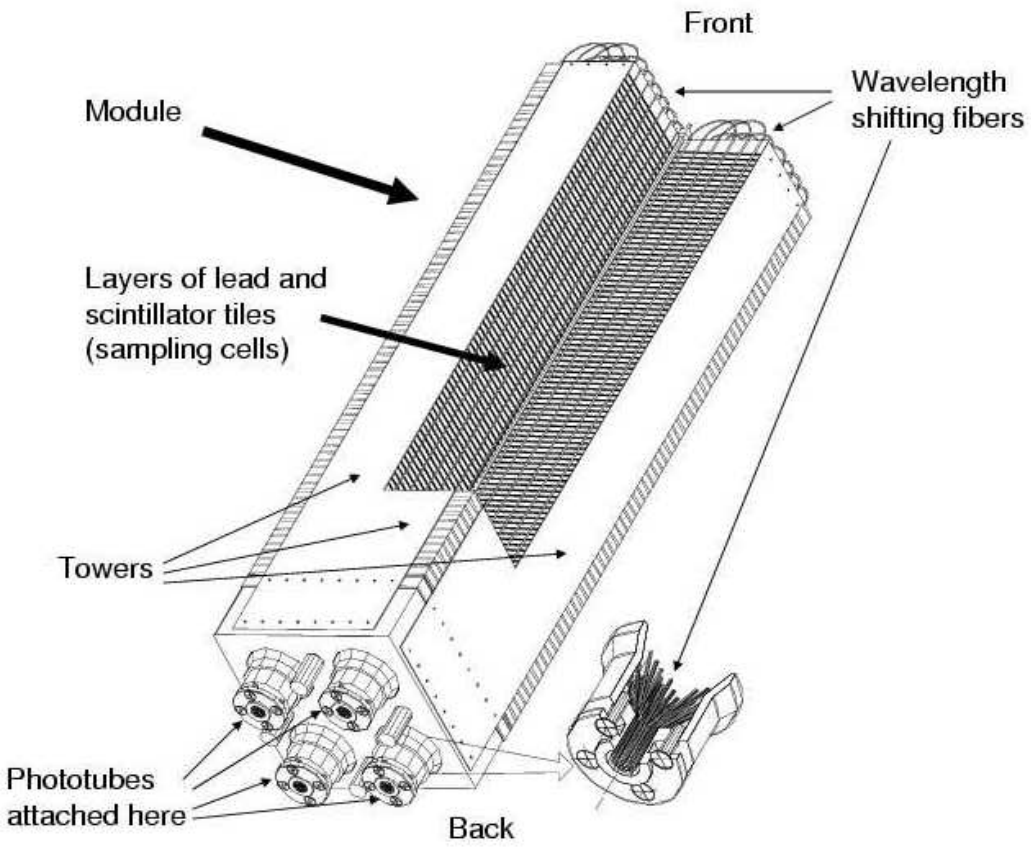

Figure 2.8: Interior view of a Lead-Scintillator calorimeter module showing a stack of scintillator and lead plates, wavelength shifting fiber readout and leaky fiber inserted in the central hole [16].

Calibration by YAG Laser

The calibration and monitoring system is based on a UV laser which supplied light to the calorimeter through a series of optical splitters and fibers. Light from a high power YAG laser is initially split into six equal intensity beams using a set of partially reflecting mirrors. The beam from each mirror passes through a quartz lens and is focused to a point just in front of a quartz fiber which is connected to one sector of the calorimeter. The plastic fiber which penetrates the center of the module is grated such that light exits along its length simulating the depth profile of a 1 GeV electromagnetic shower in the four surrounding towers. Given that the calorimeter has an intrinsic light output of about 1500 photoelectrons per GeV.

Detector Response via Test Beam

The energy linearity and resolution of energy and position as a primary basic performance of calorimeter have been measured with the particle test beams from AGS (BNL) and SPS (CERN). Figure 2.9 shows the correlation plot between the indicant energy and the energy measured in the calorimeter. Data are normalized to 1 GeV. The finite light attenuation length (100cm) in the WS fibers is a major contributor to the response non-uniformities at the low end of the energy scale, although this effect is mitigated by the fact that each fiber is looped back (Fig. 2.8), and the light collected always has a short and a long path to the phototube. Other contributors at low energies are coarse sampling and energy leakage at the front face. At high momenta the positive effect of the light attenuation in the fibers is overcompensated by the negative effect of energy leakage from the back of the calorimeter. The resulting nonlinearity is about a factor of 2 lower than what one would expect from the effect of light attenuation alone.

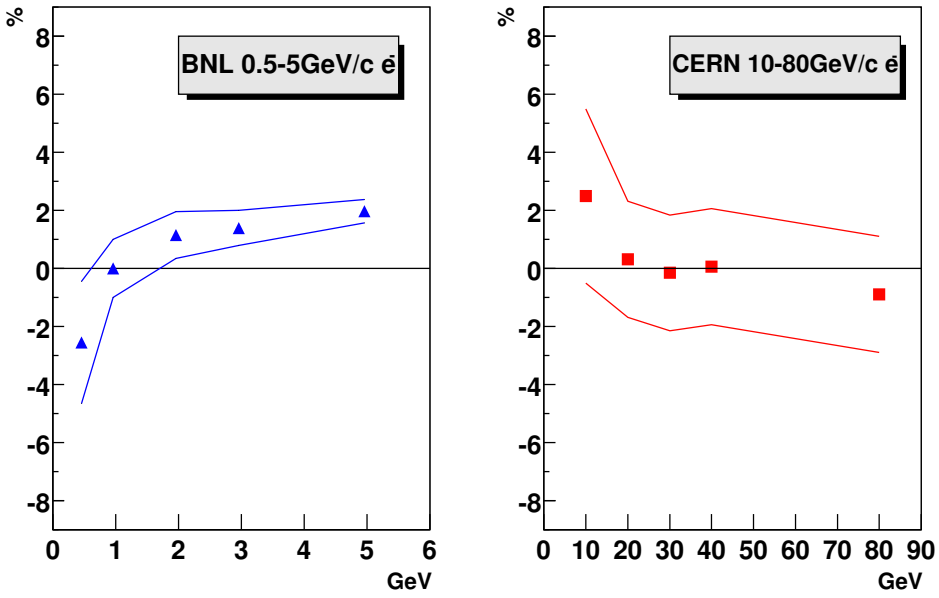

Figure 2.9: The energy linearity of Lead-Scintillator calorimeter obtained from both beam tests at BNL (left) and CERN (right). The solid lines shows total systematic uncertainties in the analysis.

Energy Resolution

The energy resolution of Lead-Scintillator is obtained by the beam test at BNL and CERN as shown in Fig. 2.10. The resolution is given by fitted with a liner (A) or quadratic (B) formula as following;

$$\left(\frac{\sigma_E}{E}\right)_{\rm A} = 1.2\% + \frac{6.2\%}{\sqrt{E(\rm GeV)}}, \tag{2.3}$$

$$\left(\frac{\sigma_E}{E}\right)_{\rm B} = 2.1\% \oplus \frac{6.2\%}{\sqrt{E(\rm GeV)}}. \tag{2.4}$$

The angular dependence of the resolution is negligible.

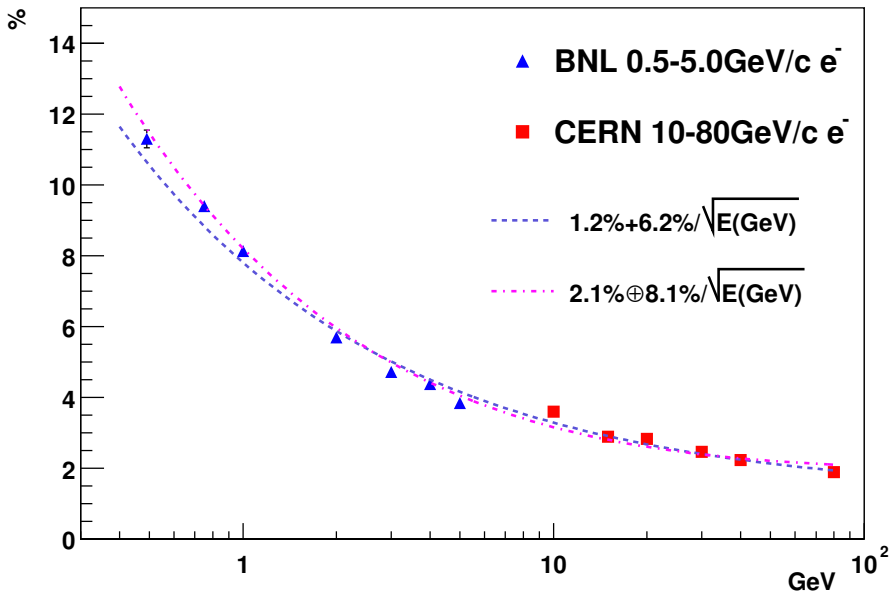

Figure 2.10: The Lead-Scintillator calorimeter energy resolution obtained by beam tests at CERN and BNL. The dashed line shows a fit to the linear function $\sigma_E/E = 1.2\% + 6.2\%/\sqrt{E(\rm GeV)}$. The dashed-dotted line shows the fit to the quadratic formula $\sigma_E/E = 2.1\% \oplus 8.1\%/\sqrt{E(\rm GeV)}$.

Both GEANT simulation and experimental data which taken at different impact angles show that the measured shower shape (the projection onto the front face of the calorimeter) becomes skewed for non-normal angle of incidence. The data also show a gradual spread of the shower core mainly related to the longitudinal shower fluctuations contributing to the observed width, which in turn depends on impact angle θ as,

$$b(\theta) = b_0 \oplus a(E) \times \sin^2(\theta) \tag{2.5}$$

where b_0 is the average width of 1 GeV electromagnetic showers for $\theta = 0$. All available data on position resolution can be well described by,

$$\sigma_x(E,\theta) = \sigma_x(E,0) \oplus (20.0[\rm mm] \cdot \sin(\theta)), \tag{2.6}$$

where $\sigma_x(E,0)$ is the position resolution for normal incidence. The position resolution obtained from both beam tests at CERN and BNL.

$$\sigma_x(E,0) = 1.4[\text{mm}] + \frac{5.9[\text{mm}]}{\sqrt{E(\text{GeV})}}. \tag{2.7}$$

2.6.2 Lead-Glass Calorimeter

The Lead-Glass calorimeter is consistent of 9216 modules of a system previously used in CERN experiment WA98 [7]. Each Lead-Glass sector comprises 192 super-modules and each super-module comprises 24 modules. Figure 2.11 shows the mechanical design of the Lead-Glass super-module.

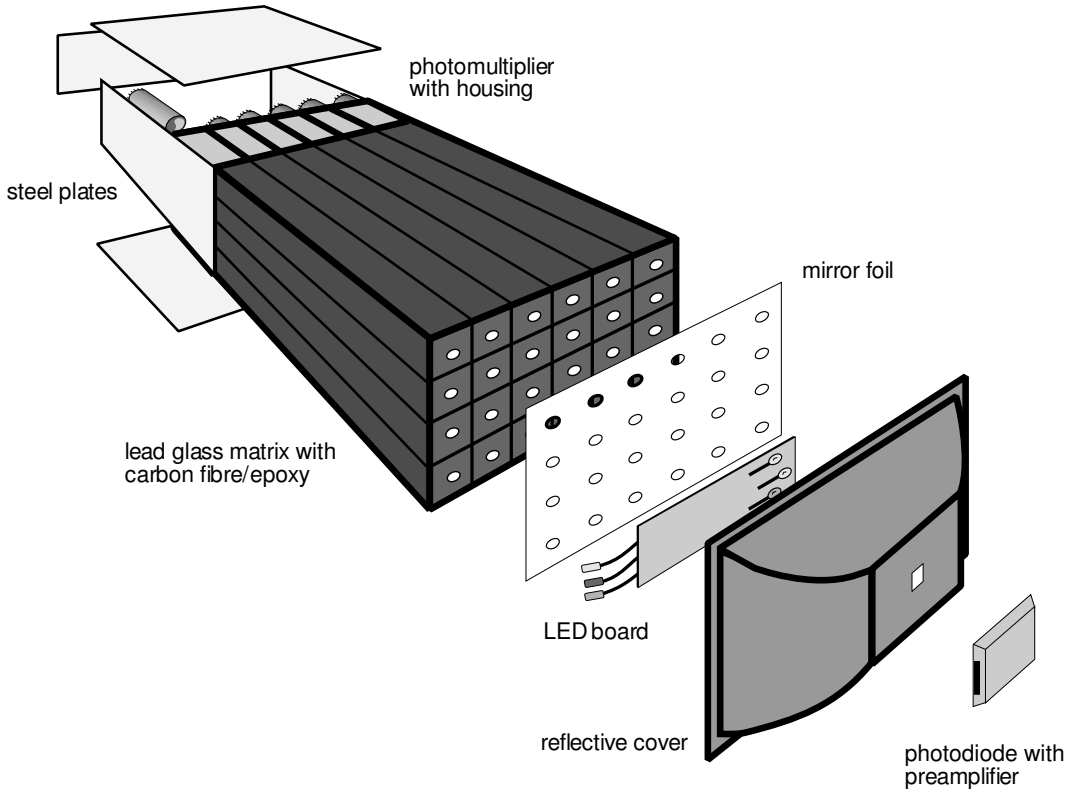

Figure 2.11: Exploded view of a Lead-Glass calorimeter super-module. Each module is read out with an FEU-84 photomultiplier.

Each super-module has its own gain monitoring system based on a set of 3 LEDs which are viewed by all 24 Lead-Glass modules within a super-module. The absolute light yields of the LEDs of each super-module are monitored by a photo-diode which, together with preamp, is permanently attached to the super-module. The Lead-Glass calibration has been maintained to within approximately 10% for PHENIX using the LED / photo-diode system.

The response of the Lead-Glass has been studied in test beams at the AGS (BNL) and SPS (CERN). The energy resolution of e^+ showers versus the incident energy is obtained the fitted

parameter for the result of test beams,

$$\frac{\sigma(E)}{E} = (0.8 \pm 0.1)\% \oplus \frac{(5.9 \pm 0.1)\%}{\sqrt{E(\mathrm{GeV})}}, \tag{2.8}$$

and the measured position resolution can be obtained by,

$$\sigma_x(E) = (0.2 \pm 0.1)[\mathrm{mm}] \oplus \frac{(8.4 \pm 0.3)[\mathrm{mm}]}{\sqrt{E(\mathrm{GeV})}}. \tag{2.9}$$

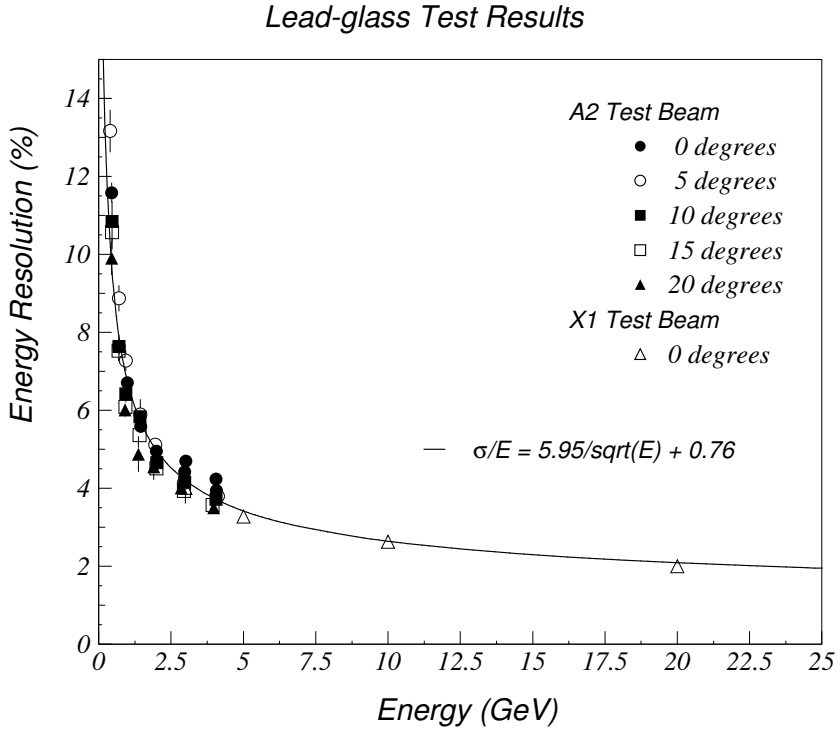

Figure 2.12: The correlation plot between Lead-Glass energy resolution and incident energy.

2.7 Reaction Plane Detector

The measurements of azimuthal anisotropy v_2 of the light hadrons in low p_{T} at the early RHIC experiment provide us a greatly information on the properties of extreme hot and dense medium. As a next stage, we have to observe more reliable study by using rare particles in broader p_{T} range, such as high p_{T} π^0, single electrons from heavy quark decay, and heavy hadrons. In order to improve the resolution of reaction plane for measurement of the rare particles, Reaction Plane Detector (RxNP) has been installed since PHENIX Year-7.

Before Year-7, the reaction plane angle is determined by using BBC in PHENIX, and the values of $\langle \cos 2\Delta\Psi \rangle$ are approximately 0.4 for minimum bias Au+Au collisions at 200 GeV. This relatively poor resolution provided by the BBC is a major limiting factor of v_2 measurement. The new detector, RxNP, has a reaction plane resolution of $\langle \cos 2\Delta\Psi \rangle$ approximately 0.7, therefore

Table 2.4: Physical parameters of the Lead-Scintillator (PbSc) and the Lead-Glass (PbGl) [16].

Parameter	PbSc	PbGl
Active Sampling Cells	66	
Scintillator [cm]	0.4	
	Polystyrene	
	(1.5% PT / 0.01% POPOP)	
Absorber [cm]	Pb, 0.15	
Index of refraction ($\bar{n}$)		1.648
Lateral Segmentation [cm^2]	5.535 × 5.535	4.0 × 4.0
Radiation length (X_0) [cm]	2.1	2.8
Moliere radius ($R_{\rm M}$) [cm]	3.0	3.68
Active depth [cm]	37.5 ($18X_0$)	40.0 ($14X_0$)
Number of super-module per sector	18 (6×3)	192 (16×12)
Number of modules per super-module	144 (12×12)	24 (6×4)
Number of total sectors	6	2
Total number of modules	15552	9216

the RxNP will improve the statistical power of v_2 measurement by about a factor if $(0.7/0.4)^2 \sim 3$.

The RxNP is composed of plastic scintillator and PMT divided by 12 × 2 sectors in each north and south side. The scintillators have a thickness of 2cm and placed at $38 < |z| < 40$cm, and covered a pseudo-rapidity range of $1.0 < |\eta| < 1.5$ (by inner ring) and $1.5 < |\eta| < 2.8$ (by outer ring). Figure 2.13 shows the front view of the reaction plane detector and size of its elements.

2.8 Data Taking Flow

The PHENIX On-Line system manages the processing of event data from the Front End Modules (FEM) on each detector subsystems for the purpose of providing events for physics analysis. The Data Collection Modules (DCM) receive data via fiber optic links from FEM's, apply the zero suppress to data and generate data packets. These packets go to the Event Builders (EvB) that assemble the events in the PHENIX Raw Data Format (PRDF). The Level-1 trigger (LVL1) generates a decision for each beam crossing and eliminates uninteresting events. All of this is controlled by the Master Timing System (MTS) that distributes the RHIC clocks. The general schematic for the PHENIX On-Line system is shown in Fig. 2.14.

2.8.1 Level-1 Trigger

The Level-1 trigger provides the potentially interesting events for all colliding species and event rejection sufficient to reduce the data rate. It consists of two separate subsystems. The Local Level-1 system communicates directly with participating detector systems such as BBC, ZDC,

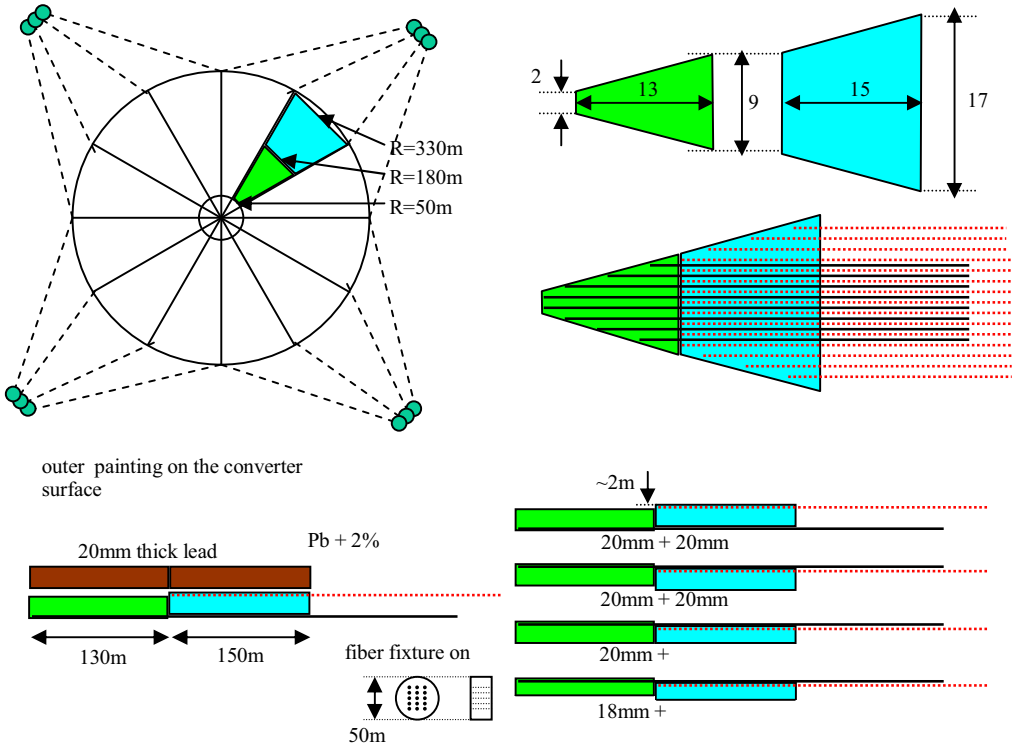

Figure 2.13: Front view of the reaction plane detector [22].

and EMCal. The input data from these detector systems are processed by the Local Level-1 algorithms to produce a set of reduced-bit input data for each collisions. The Global Level-1 system receives and combines this data to provide a trigger decision. In addition, busy signals are managed by the Global Level-1.

2.8.2 Data Collection System

The maximum average LVL1 trigger rate is 25 kHz and the RHIC beam crossing clock runs at 9.4 MHz. The FEMs send over 100 Gbytes of data per second at the maximum LVL1 trigger rate. The PHENIX Data Collection Modules (DCM) are designed to receive this large uncompressed event fragment data volume, provide data buffering, perform zero suppression for all detector system data, perform error checking, perform data formatting and output the compressed data to the PHENIX Event Builder (EvB).

2.8.3 Front End Modules

Signals from the various PHENIX subsystems are processed by Front End Electronics (FEE) that convert detected signals into digital event fragments. FEE modules in a physics experiment require a high level of control. This is accomplished for PHENIX using a large number of microprocessor based Front End Modules (FEM) located on the each detector. The functions of the FEM's are controlled by a Heap Manager (HM) [11] that performs all the functions associated with FEE control such as mode interpretation and execution, FEE timing and control, receipt of

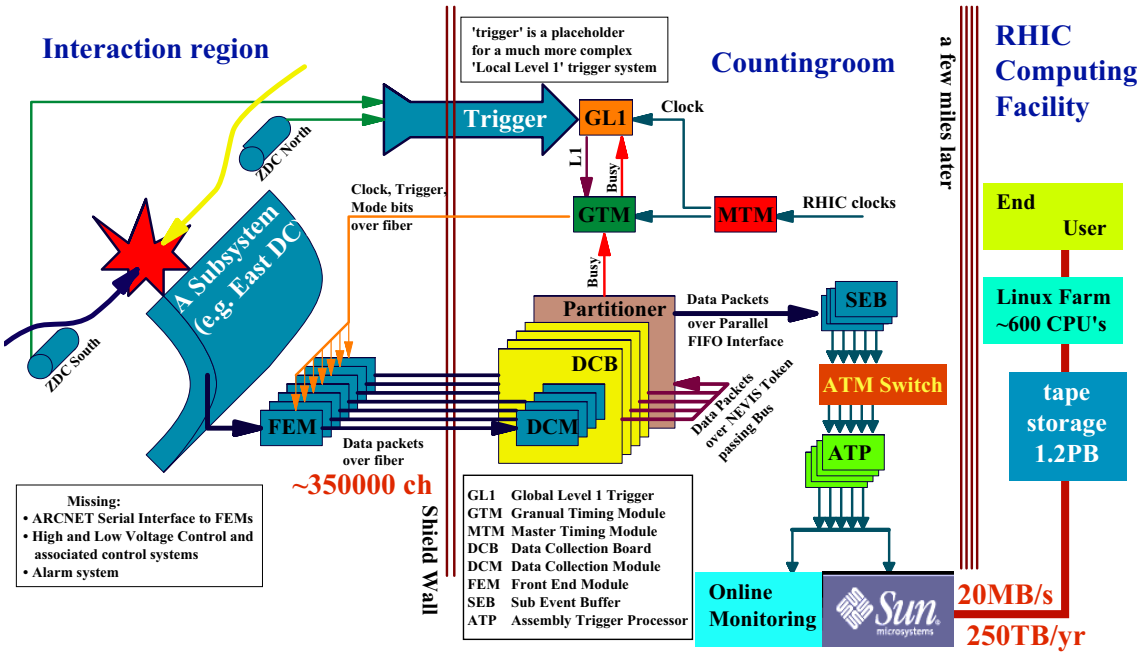

Figure 2.14: Schematic diagram of the PHENIX On-Line system.

LVL1 trigger and generation of test pulses, collection and formatting of the data, packet forming and communication of LVL1 accepted data to the DCM.

Chapter 3

Data Analysis

The experimental data of Au+Au collisions at $\sqrt{s_{\rm NN}} = 200$ GeV which is based on this analysis have been collected in the RHIC Year-4 (2004) and Year-7 (2007). In this chapter, we presented the event selection for analysis (Section 3.1), procedure of centrality determination present the event selection for the analysis (Section 3.2) and reaction plane determination (Section 3.3). The clustering algorithm for photons and electrons (Section 3.4) and the particle identification criteria using the PHENIX-EMCal are described in Section 3.5. Direct photons which are defined as photons emitted from the collisions events but not originated from the hadronic decays are measured by subtraction method of hadronic decay photons. The analysis procedure of measurement for inclusive photon , neutral pion, and direct photon are described in Section 3.6, 3.7, and 3.8.

3.1 Event Selection

All raw data detected by each subsystems are assembled by the Event Builder in the PHENIX Raw Data Format (PRDF). The information in a PRDF are reconstructed as physics meaningful values such as energy, momentum, hit position and collision time, then generated the another format file (nano-DST).

The minimum bias trigger is required a coincidence between north and south BBC with at least two PMT hits and at least one forward neutron in north and south ZDC. And also we required the event z vertex position within 38 cm in the BBC Local level-1.

- BBC north $> 2 \cap$ BBC south > 2
- |BBC z-vertex| < 38 cm (required by BBC Local Level-1)
- ZDC north $> 1 \cap$ ZDC south > 1

The BBC trigger efficiencies have been evaluated by HIJING events and the BBC Local Level-1 logic [62]. The result of estimated BBC trigger efficiency is $92.3\% \pm 0.4\%$(stat.) $\pm 1.6\%$(sys.), when we required |BBC z-vertex| < 30 cm (this value has been determined by the bunch length) in the offline analysis for reduction of the accidental background.

3.2 Centrality Definition

Although a particle multiplicity is expected to sensitive to the impact parameter in the nucleus-nucleus collisions, it is not easy to measure a true impact parameter experimentally at given event. In the PHENIX, BBC charge sum and ZDC energy sum can be related to an impact parameter, since BBC charge sum reflects the participant energy and ZDC energy sum reflects the spectator energy. Therefore, the centrality which is defined by BBC charge sum and/or ZDC energy sum allows us the meaningful physics discussion without direct measurement of impact parameter.

3.2.1 Correlation between BBC and ZDC

The collision centralities are defined from the correlation between the charge deposit in BBC (Sec. 2.3) and the energy deposit in ZDC (Sec. 2.4). Figure 3.1 shows each centrality region with

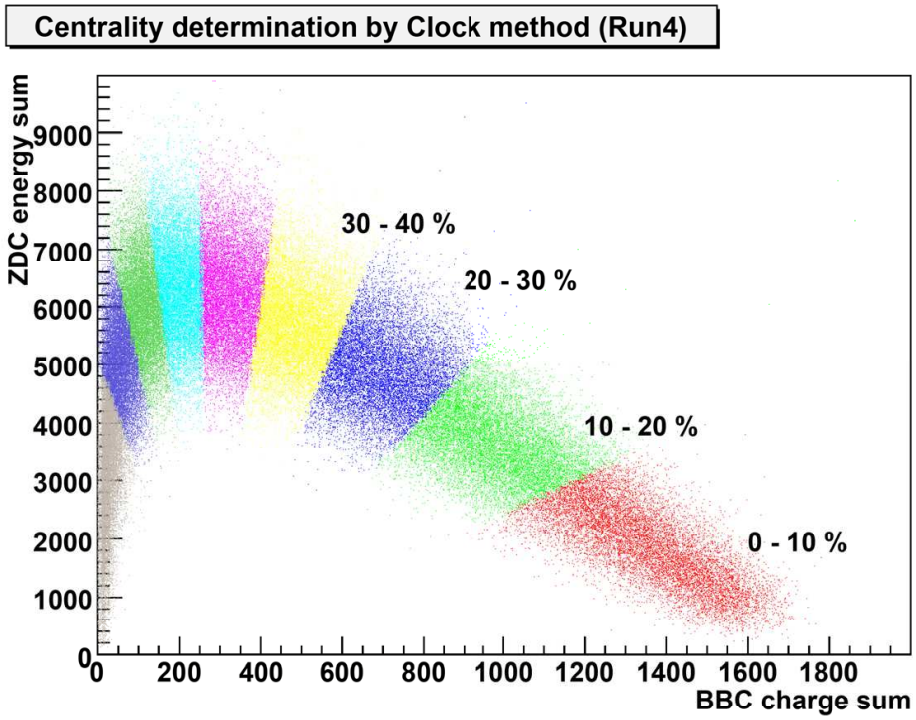

Figure 3.1: The centrality determined by the correlation between the BBC charge sum and the ZDC energy sum at PHENIX Year-4.

different color in the measured correlation BBC charge sum and ZDC energy sum in PHENIX Year-4 (Table 2.2). The angular position $\phi_{\rm cent}$ of a given event defined as,

$$\phi_{\rm cent} = \tan^{-1}\left(\frac{(Q^{\rm BBC} - Q_0^{\rm BBC})/Q_{\rm max}^{\rm BBC}}{E^{\rm ZDC}/E_{\rm max}^{\rm ZDC}}\right) \tag{3.1}$$

where, $Q^{\rm BBC}$ and $E^{\rm ZDC}$ are the measured charge sum in BBC and the energy sum in ZDC. $Q_{\rm max}^{\rm BBC}$ and $E_{\rm max}^{\rm ZDC}$ are the maximum measured charge sum in BBC and the maximum measured

total energy deposit in ZDC. The base position as $Q_0^{\mathrm{BBC}} \sim 250$ is determined by simple Glauber simulation in Au + Au collisions.

The boundaries angle ϕ_{cent} is calibrated to make flat centrality distribution. In the analysis using PHENIX Year-4 data, the centrality is divided from 0 to 93% instead of 0 to 100% because of the detector efficiency for the minimum bias trigger [65].

3.2.2 BBC Charge Sum Method

There is a possibility that the resolution of obtained centrality by using the correlation of BBC charge sum and ZDC total energy is deteriorated by the performance of ZDC because the resolution of ZDC is worse than BBC. In addition, there is no physics reason critically to determine

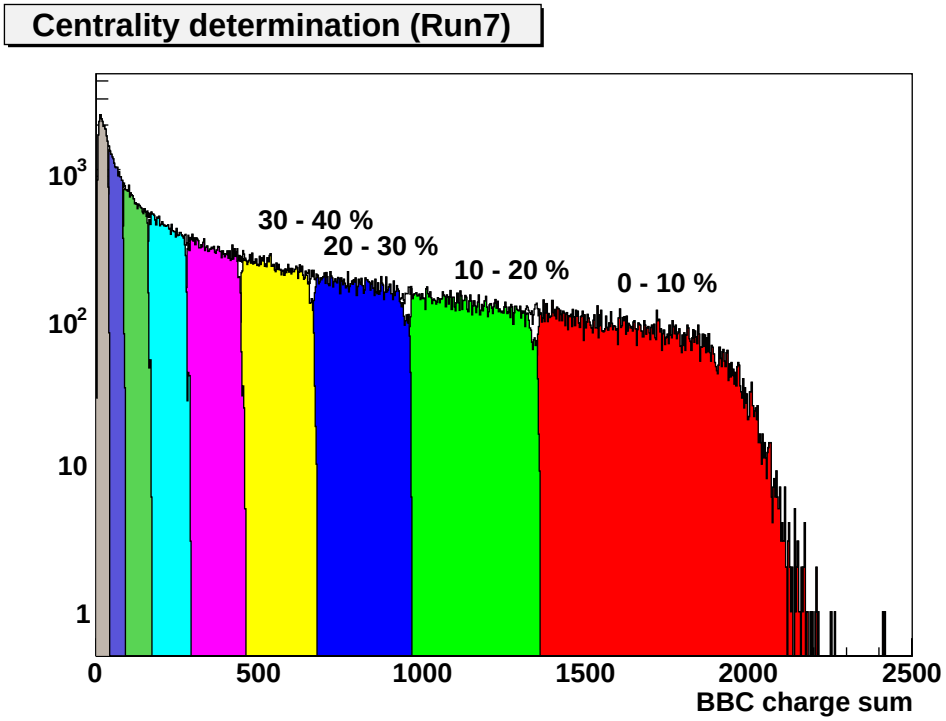

Figure 3.2: The centrality determined by the BBC charge sum method at PHENIX Year-7.

the centrality using ϕ_{cent} based on Q_0^{BBC}. Therefore the experimental data analysis in PHENIX Year-7 switched to the method to using BBC charge sum only for the centrality definition. The centrality defined by this method would allow us think instinctively compared to the BBC-ZDC correlation method, due to the simplicity.

Figure 3.2 shows the BBC charge sum distribution with the determined centrality classes as shown in the different colors. The boundaries of n% centrality (x_n) are determined as,

$$x_n = \sum_{i=0}^{n} i \cdot \left(\frac{Q_{\mathrm{all}}^{\mathrm{BBC}}}{A_{\mathrm{eff.}}^{\mathrm{BBC}}} \right), \tag{3.2}$$

where, $Q_{\mathrm{all}}^{\mathrm{BBC}}$ is the total charge sum in BBC and $A_{\mathrm{eff.}}^{\mathrm{BBC}}$ is efficiency of BBC which applied the same value as PHENIX Year-4. The data taking period of PHENIX Year-7 is divided into 13

regions in order to calibrate the centrality boundaries at each period for the reduction of the run-by-run fluctuations.

3.3 Reaction Plane Determination

An azimuthal angle distribution of particle emissions is measured relative to the reaction plane angle at an each given event. In this section, a Fourier expansion of azimuthal distribution, the extraction procedure of v_2, and the method of reaction plane calibration are described.

3.3.1 Fourier Expansion

The azimuthal distribution of produced particles is studied by using reaction plane which is determined by the direction of impact parameter and horizontal plane in an each event. Since the azimuthal distribution ($r(\phi)$) is a cyclic function with 2π period, it can be written in the form of Fourier expansion;

$$\begin{aligned} r(\phi) &= \frac{x_0}{2\pi} + \frac{1}{\pi}\sum_{n=1}^{\infty}[x_n\cos(n\phi) + y_n\sin(n\phi)], \\ &= \frac{x_0}{2\pi}\left\{1 + 2\sum_{n=1}^{\infty}\left(\frac{x_n}{x_0}\cos(n\phi) + \frac{y_n}{x_0}\sin(n\phi)\right)\right\}, \end{aligned} \tag{3.3}$$

where, n is the event number, x_n and y_n are the integral components of the r for x and y directions. For the case of only a finite number of particles in the event, the integral components become simple summations over particles;

$$x_n = \int_0^{2\pi} r(\phi)\cos(n\phi)d\phi = \sum_i r_i\cos(n\phi_i), \tag{3.4}$$

$$y_n = \int_0^{2\pi} r(\phi)\sin(n\phi)d\phi = \sum_i r_i\sin(n\phi_i), \tag{3.5}$$

where, i runs over all particles generated by collisions and ϕ_i is the azimuthal angle of particle. A volume of the n-th harmonic parameter (v_n) and an azimuthal angle of reaction plane (Ψ_n) are defined as;

$$v_n = \frac{\sqrt{x_n^2 + y_n^2}}{x_0}, \tag{3.6}$$

$$\Psi_n = \frac{1}{n}\tan^{-1}\left(\frac{y_n}{x_n}\right). \tag{3.7}$$

If we assume the azimuthal angle in Eq.(3.3) is defined relative to the reaction plane, the integration of y_n terms in the $r(\phi)$ would be zero since the $r(\phi)$ becomes an even function;

$$r(\phi) = \frac{x_0}{2\pi}\left\{1 + 2\sum_{n=1}^{\infty}\left(\frac{x_n}{x_0}\cos(n\phi)\right)\right\}. \tag{3.8}$$

The coefficient x_n and y_n are written by using the v_n and Ψ_n;

$$x_n = x_0 \cdot v_n\cos(n\Psi_n), \tag{3.9}$$

$$y_n = y_0 \cdot v_n\sin(n\Psi_n). \tag{3.10}$$

Then, the azimuthal angle of emitted particles are given by,

$$\begin{aligned} r(\phi) &= \frac{x_0}{2\pi}\left\{1+2\sum_{n=1}^{\infty}\left(\frac{x_n}{x_0}\cos(n\phi)\right)\right\} \\ &= \frac{x_0}{2\pi}\{1+2\sum_{n=1}^{\infty}[v_n\cos(n\Psi_n)\cos(n\phi)]\} \\ &= \frac{x_0}{2\pi}\{1+2\sum_{n=1}^{\infty}[v_n\cos(n(\phi-\Psi_n))]\}. \end{aligned} \tag{3.11}$$

The harmonic coefficients v_n which indicates the strength of the n-th anisotropy is calculated by,

$$v_n = \langle\cos(n(\phi-\Psi_n))\rangle\,. \tag{3.12}$$

3.3.2 Reaction Plane Method

In the experiment, an angle of reaction plane is determined by the azimuthal distribution of emitted particles at the given event, since a true reaction plane is not able to determine directly. The measured azimuthal angle of reaction plane is given by,

$$\Psi_n^{\text{meas.}} = \frac{1}{n}\tan^{-1}\left(\frac{Q_y^{\text{meas.}}}{Q_x^{\text{meas.}}}\right), \tag{3.13}$$

$$Q_x^{\text{meas.}} = \sum_i w_i\cos(n\phi_i), \tag{3.14}$$

$$Q_y^{\text{meas.}} = \sum_i w_i\sin(n\phi_i), \tag{3.15}$$

where w_i is the charge information of i-th particles which is detected by each PMT of detectors, and ϕ_i is the azimuthal angle.

The measured reaction plane angle ($\Psi^{\text{meas.}}$) which is reconstructed by experimental detectors is not corresponding to the true reaction plane (Ψ^{true}) exactly. Therefore measured Fourier coefficient ($v_n^{\text{meas.}}$) should be related to the true one (v_2^{true}) using $\Psi^{\text{meas.}}$ and Ψ^{true} [37].

$$\begin{aligned} v_n^{\text{meas.}} &= \langle\cos\{2(\phi-\Psi^{\text{meas.}})\}\rangle \\ &= \left\langle\cos[2\{(\phi-\Psi^{\text{true}})-(\Psi^{\text{meas.}}-\Psi^{\text{true}})\}]\right\rangle \\ &= \left\langle\cos\{2(\phi-\Psi^{\text{true}})\}\right\rangle\left\langle\cos\{2(\Psi^{\text{true}}-\Psi^{\text{meas.}})\}\right\rangle \\ &\quad + \left\langle\sin\{2(\phi-\Psi^{\text{true}})\}\right\rangle\left\langle\sin\{2(\Psi^{\text{true}}-\Psi^{\text{meas.}})\}\right\rangle \\ &= \left\langle\cos\{2(\phi-\Psi^{\text{true}})\}\right\rangle\left\langle\cos\{2(\Psi^{\text{true}}-\Psi^{\text{meas.}})\}\right\rangle \\ &= v_n^{\text{true}}\left\langle\cos\{2(\Psi^{\text{true}}-\Psi^{\text{meas.}})\}\right\rangle \end{aligned} \tag{3.16}$$

Therefore, the coefficient in the Fourier expansion of the azimuthal distributions with respect to the true reaction plane is given by,

$$v_n^{\text{true}} = \frac{v_n^{\text{meas.}}}{\langle\cos\{2(\Psi^{\text{true}}-\Psi^{\text{meas.}})\}\rangle}. \tag{3.17}$$

The value of $\left\langle\cos\{2(\Psi^{\text{true}}-\Psi^{\text{meas.}})\}\right\rangle$ is called "reaction plane resolution" in the following section.

3.3.3 Reaction Plane Calibration

Observed azimuthal angle of reaction plane which determined by experimental detectors has an anisotropic bias. The causes of asymmetric response of detectors are categorized as follows;

- Uninformed response of BBC's PMTs,
- Difference between center of BBC and the beam line,
- Anisotropic installed position of BBC's PMTs.

In order to correct the response of PMTs, we calibrated the gains based on observed MIP peak, selected the pedestal and charge-to-channel conversion factor of ADC and TDC, and applied the slewing correction. After that, PMT hit distribution of Q_x and Q_y are re-centered to correct the bias caused by shift of beam line as,

$$Q_x^{\text{corr.}} = \frac{Q_x - \langle Q_x \rangle}{\sigma_x}, \tag{3.18}$$

$$Q_y^{\text{corr.}} = \frac{Q_y - \langle Q_y \rangle}{\sigma_y}, \tag{3.19}$$

where $\langle Q_i \rangle$ is the mean of Q_i, and σ_i is the width of Q_i. The mean and width are extracted by fitting Q_x and Q_y distribution with gaussian. Finally, to calibrate the remaining non-flatness of reaction plane caused by configuration of detectors or something, we perform flattening calibration which is defined by [38],

$$n\Psi = n\Psi^{\text{corr.}} + \Delta\Psi, \tag{3.20}$$

$$\Delta\Psi = \sum_n A_n \cos(2n\Psi^{\text{corr.}}) + B_n \sin(2n\Psi^{\text{corr.}}) \tag{3.21}$$

The coefficients A_n and B_n are obtained by requiring the n-th Fourier moment of the Ψ distribution,

$$A_n = -\frac{2}{n} \langle \sin(2n\Psi^{\text{corr.}}) \rangle \tag{3.22}$$

$$B_n = \frac{2}{n} \langle \cos(2n\Psi^{\text{corr.}}) \rangle . \tag{3.23}$$

3.3.4 Reaction Plane Resolution

The reaction plane resolution can be expressed as [49],

$$\left\langle \cos[2(\Psi^{\text{true}} - \Psi^{\text{meas.}})] \right\rangle = \frac{\sqrt{\pi}}{2\sqrt{2}} \chi_m \exp(-\chi_m^2/4)[I_0(\chi_m^2/4) + I_1(\chi_m^2/4)], \tag{3.24}$$

where $\chi_m = v_m/\sigma = v_m\sqrt{2N}$ and I_ν is the modified Bessel function of order ν. If we estimate the reaction plane by using two sub-events (A and B), the resolutions of these plane are described

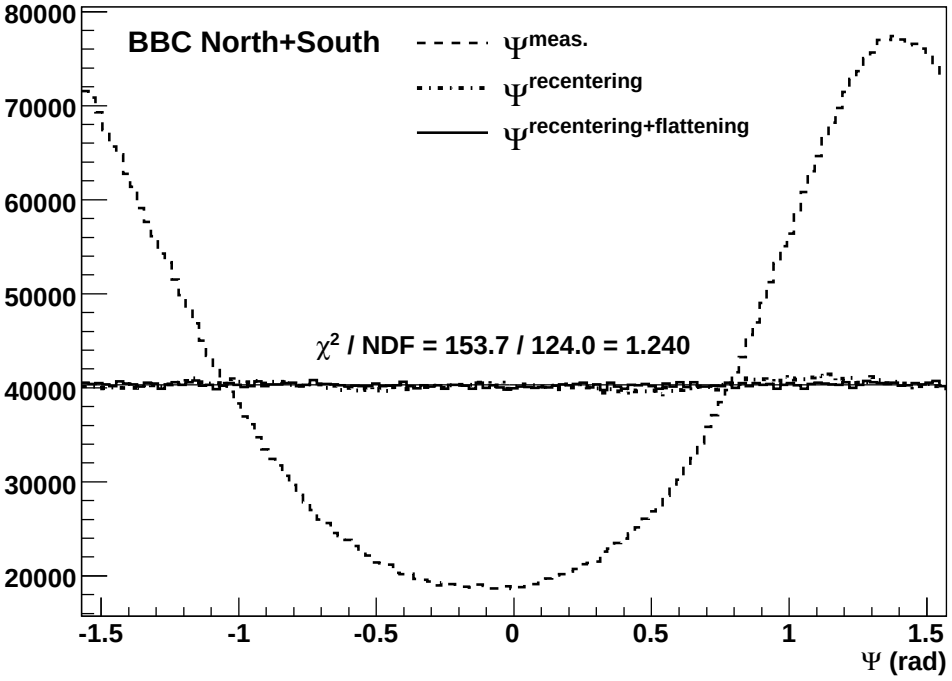

Figure 3.3: Reaction plane distribution for BBC north+south. Dashed line; applied the BBC calibration only. Solid line; applied the re-centering and flattening correction. The value of χ^2 on this figure shows the linear fitting result for calibrated distribution.

as,

$$\sigma_{\rm A} = \left\langle \cos[2(\Psi^{\rm true} - \Psi_{\rm A})] \right\rangle \tag{3.25}$$

$$\sigma_{\rm B} = \left\langle \cos[2(\Psi^{\rm true} - \Psi_{\rm B})] \right\rangle \tag{3.26}$$

$$\begin{aligned} \sigma_{\rm AB} &\equiv \langle \cos[2(\Psi_{\rm A} - \Psi_{\rm B})] \rangle \\ &= \left\langle \cos[2(\Psi^{\rm true} - \Psi_{\rm A})] \right\rangle \left\langle \cos[2(\Psi^{\rm true} - \Psi_{\rm B})] \right\rangle \\ &= \sigma_{\rm A} \cdot \sigma_{\rm B} \end{aligned} \tag{3.27}$$

If we assumed the resolution of two sub-events are same, the reaction plane resolution of sub-event A(B) or combined sub-event C(=A$\oplus$B) are able to estimate by the angle of sub-event A and B.

$$\sigma_{\rm A} = \sigma_{\rm B} = \sqrt{\sigma_{\rm AB}} = \sqrt{\langle \cos[2(\Psi_{\rm A} - \Psi_{\rm B})] \rangle} \tag{3.28}$$

$$\sigma_{\rm C} = \sqrt{\sigma_{\rm A}^2 + \sigma_{\rm B}^2} = \sqrt{2 \left\langle \cos[2(\Psi_{\rm A} - \Psi_{\rm B})] \right\rangle} \tag{3.29}$$

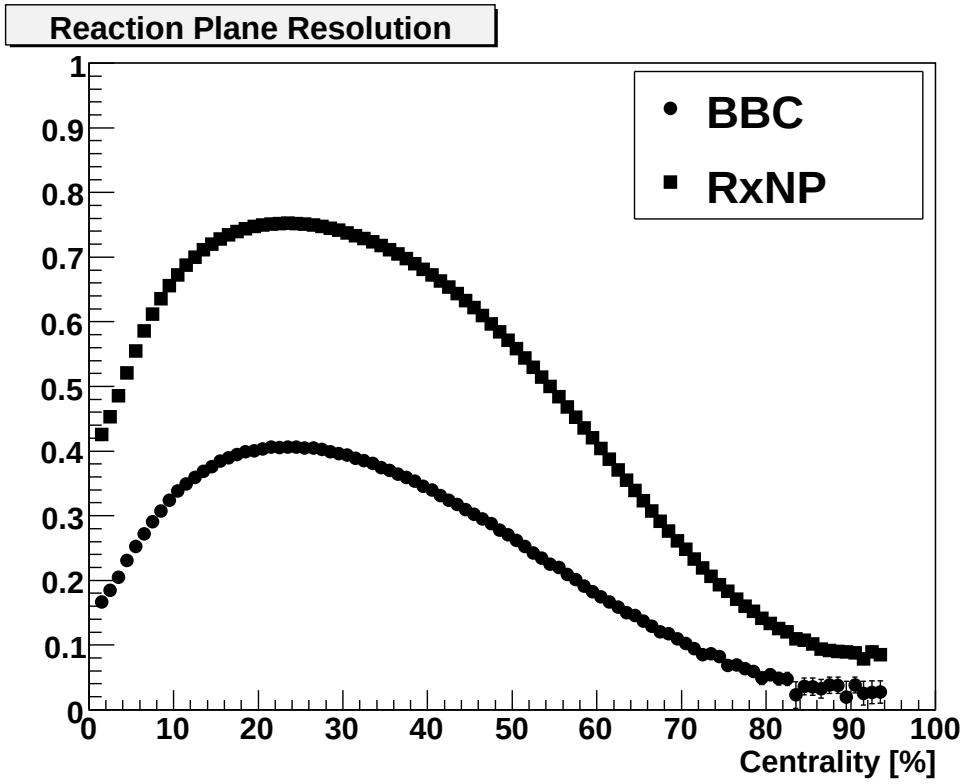

Figure 3.4: Reaction plane resolution determined by BBC north⊕south and RxNP north⊕south with Eq 3.24 as a function of centrality.

In the PHENIX experiment, two BBCs and RxNPs are placed on the north and south sides of the collision point respectively. The centrality dependence of reaction plane resolution which determined by BBC north⊕south and RxNP north⊕south is shown in Fig. 3.4, if we assume the resolution of north/south BBC and north/south RxNP are same, respectively.

3.4 EMCal Clustering

Electromagnetic shower in the EMCal deposits their $\sim$ 90% energy to a lateral corn of the Moliere Radius ($R_{\rm M}$) which is characterized by a radiation length (X_0) and an atomic number of the matter. The $R_{\rm M}$ of PHENIX EMCals are calculated about $3 \sim 4$ cm by using the typical value of X_0 as 2.1 cm (for PbSc) and 2.8 cm (for PbGl). Therefore, electromagnetic shower generally deposits the energy over two towers or more. If only one particle goes in the EMCal, electromagnetic shower corresponds to an energy of cluster towers which satisfied the back ground threshold. Actually we execute the high multiplicity experiment in PHENIX, detected cluster might be consisted of two or more showers. In this section, clustering algorithm and energy reconstruction of PHENIX EMCal for the photon measurements are described.

3.4.1 Clustering Algorithm

The following step is adopted as the general analysis procedure for clustering and energy reconstruction in PHENIX Year-4 and Year-7 data sets.

1. Applying the energy threshold (10 MeV) for all towers to reduce the noise. The neighboring towers which satisfied the noise threshold made a group mutually, and the cluster is formed. These clusters are called "isolated cluster".

2. Finding a "local maximum tower" which contained the maximum amplitude in 3×3 around towers and satisfied the additional energy threshold (80 MeV). The towers in 5×5 around the local maximum tower are called "peak area".

3. If there is a tower with contribution from two or more peak areas, the tower energy divided into each peak areas according to parameterized shower profile (Sec. 3.4.3). Then splitting the peak area.

4. Redefining the cluster area as "core cluster" by the towers which contained more than 2% of energy sum in the belonging peak area.

Loss energy caused by some thresholds and core clustering is corrected by Monte-Carlo simulation, the study of detector response by using test beam data, and energy scale calibration in the offline analysis.

3.4.2 Correction of Hit Position

The hit position of particle on the surface of EMCal is estimated by the center of amplitude gravity for each peak area,

$$x_{\rm cent} = \frac{1}{E_{\rm tot}} \sum_{i=0}^{n} E_i x_i, \tag{3.30}$$

$$y_{\rm cent} = \frac{1}{E_{\rm tot}} \sum_{i=0}^{n} E_i y_i, \tag{3.31}$$

where, $x_{\rm cent}$ and $y_{\rm cent}$ denote the x and y position of the center of gravity, and E_i is its energy. $E_{\rm tot}$ is the energy sum in peak area ($E_{\rm tot} = \sum_{i=0}^{n} E_i$). In the experiment, the center of gravity is not corresponding to the hit position because shower development angle depends on the angular incidence. The relation between the center of gravity $(x_{\rm cent}, y_{\rm cent})$ and true hit position $(x_{\rm true}, y_{\rm true})$ is studied by using the test beam data,

$$\begin{pmatrix} x_{\rm true} \\ y_{\rm true} \end{pmatrix} = \begin{pmatrix} x_{\rm cent} - (1.05 + 0.12 \ln E_{\rm tot}) \sin^2 \alpha_x \\ y_{\rm cent} - (1.05 + 0.12 \ln E_{\rm tot}) \sin^2 \alpha_y \end{pmatrix}, \tag{3.32}$$

$$\sin \alpha_x = \frac{v_x}{\sqrt{v_x^2 + v_z^2}}, \tag{3.33}$$

$$\sin \alpha_y = \frac{v_y}{\sqrt{v_y^2 + v_z^2}}, \tag{3.34}$$

where, (v_x, v_y, v_z) is defined as the vector from collision vertex to the center of gravity. Figure 3.5 shows the definitions of vectors and the method of hit position correction.

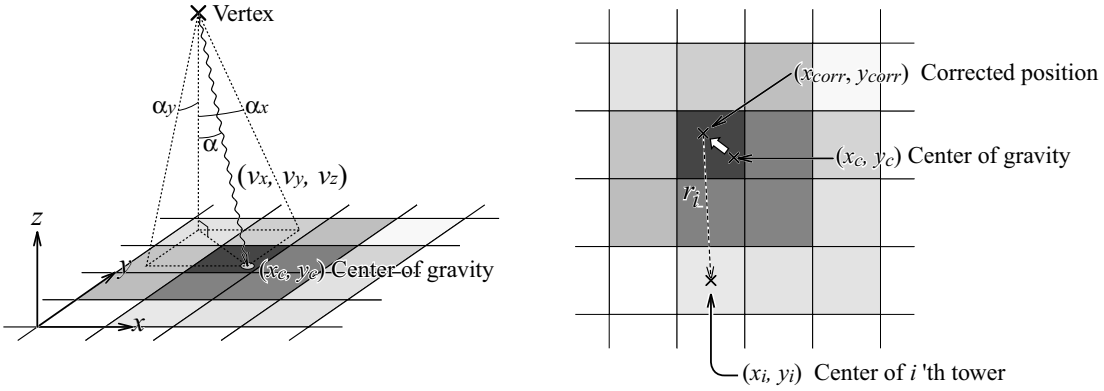

Figure 3.5: Definitions of vectors and impact angles [55]. The impact position is corrected by using the test beam data. The amplitude of each tower is represented by gray scale.

3.4.3 Reconstruction of Core Energy

In order to reduce the shower overlap effect in each peak area, the cluster areas are redefined into "core" towers.

Function of Shower Energy

The energy deposit from photon and hadronic shower in each tower of EMCal are predicted by using the a full hit level simulation with detector response called PISA which is based on GEANT [51] and tuned by the result of test beam. The predicted shower shape function of i-th tower (F_i) which is 2-D exponential in the tower distance from local maximum tower is parametrized

by,

$$F_i = \frac{E_i^{\rm pred}}{E_{\rm tot}}, \tag{3.35}$$

$$= P_1(E_{\rm tot},\alpha)\exp\left\{-\frac{(r_i/r_0)^3}{P_2(E_{\rm tot},\alpha)}\right\} + P_3(E_{\rm tot},\alpha)\exp\left\{-\frac{(r_i/r_0)}{P_4(E_{\rm tot},\alpha)}\right\}, \tag{3.36}$$

where, $E_i^{\rm pred}$ is the predicted energy of $i-$th tower, r_i is the distance between the center of $i-$th tower and corrected hit position, and r_0 is the surface size of a EMCal cell (5.5 cm). P_{1-4} are the parametrized functions which depend on the total energy $E_{\rm tot}$ and impact angle α defined as the angle of incidence. These functions are obtained from the performance at the beam test;

$$P_1 = 0.59 - (1.45 + 0.13\ln E_{\rm tot})\sin^2\alpha, \tag{3.37}$$

$$P_2 = 0.27 + (0.80 + 0.32\ln E_{\rm tot})\sin^2\alpha, \tag{3.38}$$

$$P_3 = 0.25 + (0.45 - 0.036\ln E_{\rm tot})\sin^2\alpha, \tag{3.39}$$

$$P_4 = 0.42. \tag{3.40}$$

For instance, if a photon hits at the center of a tower perpendicularly, the electromagnetic shower deposits about 84% of own energy in the hit tower. Figure 3.6 shows the example of shower energy fraction display in neighborhood towers.

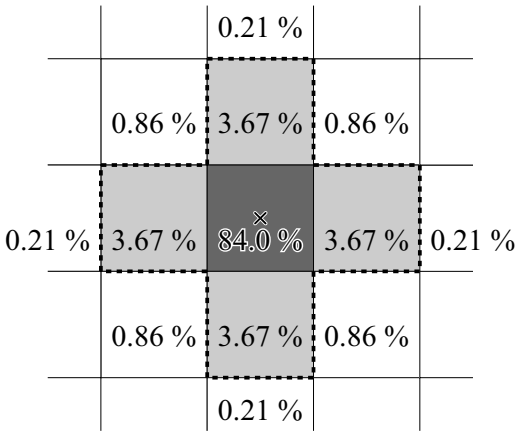

Figure 3.6: Example of the shower energy fraction in EMCal towers under assuming that a photon hit in the center of tower perpendicularly [55]. The core clusters formed by the towers contained more than 2% of total energy. In this case, surrounded five towers by dotted line is formed a core cluster.

The $E_i^{\rm pred}$ is calculated for all towers in the peak area. If the tower is belonging to plural peak area, the energy are divided into each peak area according to the ratio of each E_i which is calculated from the position and angle of local maximum tower.

Core Clustering

Naturally, the probability of hitting particle on the towers increases with the particle multiplicities. In the central Au+Au collisions at $\sqrt{s_{\rm NN}} = 200$ GeV, a hit occupancy is expected about

15% for the PbSc EMCal. The towers belonging to split peak area are reformed to a few towers which satisfied the energy threshold to total energy sum in the peak area ($E_i^{\rm pred} > 0.02 E_{\rm tot}^{\rm meas.}$) for the reduction of shower overlap effect in the high multiplicity experiment. These towers called "core" cluster. The towers belonging to core cluster is defined by,

$$E_{\rm core} = \sum_{E_i^{\rm pred}/E_{\rm tot}^{\rm meas.}>0.02} E_i^{\rm meas.}, \tag{3.41}$$

where, $E_i^{\rm meas.}$ is the measured energy deposit in the $i-$th tower and $E_i^{\rm pred}$ is its predicted energy deposit by shower shape profile. Figure 3.6 shows the example of core clustering by dotted line. Remaining tower energy around core towers are neglect in this procedure.

The variance of the predicted energy function σ_i is parametrized with the angle of incidence and losses to the total energy due to the clustering thresholds, $q(E_{\rm tot}) = 0.005^2 + 0.0014^2 \cdot E_{\rm tot}^2$ (GeV^2),

$$\sigma^2 = A \cdot E_i^{\rm pred} \left(1 + B\sqrt{E_{\rm tot}}\sin^4\alpha\right)\left(1 - \frac{E_i^{\rm pred}}{E_{\rm tot}}\right) + q(E_{\rm tot}), \tag{3.42}$$

where, constant $A = 0.03$ (GeV^2) is the scale for energy fluctuations of the shower and constant $B = 4.0/0.03 \sim 133$ is the amplitude of correction function for impact angle $B\sqrt{E_{\rm tot}}\sin^4\alpha$ given by the test beam data. For example, when one 1 GeV photon entered to EMCal perpendicularly, the predicted energy deposit on the central tower is about 840 MeV and this energy fluctuation variance is 64 MeV.

Correction for $E_{\rm core}$

The number of towers used for $E_{\rm core}$ calculation depends on the particle hit position and angle on the tower surface. In this procedure, the contribution from the shower tail is definitely neglected from $E_{\rm core}$. In the case of Fig. 3.6, at least $4 \times 0.86\% + 4 \times 0.21\% \sim 4\%$ of shower energy is missing. Therefore the measured $E_{\rm core}$ has to correct the energy fraction. The correction factor depends on the hit angle α and energy is estimated based on the Monte Carlo simulation which uses the parameterization given by test beam data as follows:

$$\frac{E_{\rm core}}{E_{\rm core}^{\rm corr}} = A \cdot (1 - B\sin^4\alpha \cdot (1 - C \cdot \ln E_{\rm core})), \tag{3.43}$$

where, $A = 0.918$, $B = 1.35$, and $C = 0.003$. $E_{\rm core}^{\rm corr}$ is the corrected core energy by using Eq. 3.43. The corrected core energy $E_{\rm core}^{\rm corr}$ denotes $E_{\rm core}$ simply in following discussions.

3.4.4 Calibration of Energy Scale

The remaining contribution on the energy resolution caused by clustering and correction algorithm is not still negligible because a few % deviation of the energy scale corresponds to the large contamination in the invariant yield due to the energy spectrum is falling steeply. The additional energy corrections for the PbSc EMCal have been determined by the identified π^0 and MIP peak using p+p data in each individual towers. The run by run correction factor is calculated for the MIP and π^0 peak position to correct the fluctuations of the stability. After that, additional

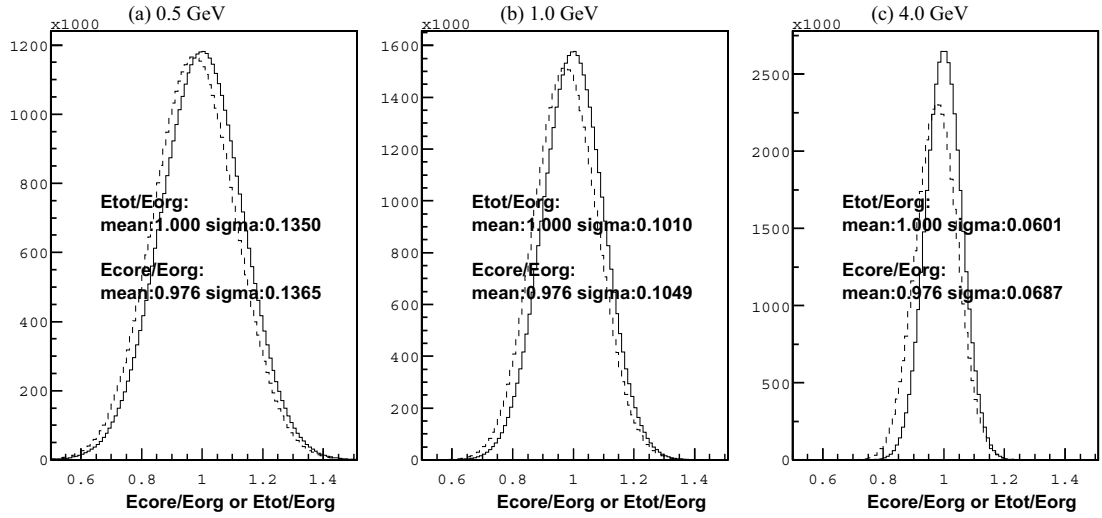

Figure 3.7: The resolution of reconstructed photon energy is studied by using GEANT simulation [55]. The ratio of core energy $E_{\rm core}$ and total energy $E_{\rm tot}$ to the true photon energy on the simple Gaussian distribution ($E_{\rm org}$) with intrinsic energy resolution of EMCal for 0.5, 1.0 and 4.0 GeV is shown. Solid lines show the $E_{\rm tot}/E_{\rm org}$ and dashed lines show the $E_{\rm core}/E_{\rm org}$.

correction process are applied for the towers which failed the detection of π^0 peak position by using the exponential fitting parameter of $E_{\rm core}$ slope.

The basic idea of energy scale by using π^0 is that the invariant mass of decay photon pairs from a π^0 would have an invariant mass equal to the π^0 mass. The invariant mass is assumed that evenly divided into two decay photons, the correction factor for measured cluster energy is extracted from the ratio between measured invariant mass and the π^0 mass. However we might need to know the influence of the unequal energy distribution of actual two decay particles, and failed identification of π^0 caused by low statistics on several towers. Therefore, the calibration method of $E_{\rm core}$ slope is suggested by using only photons. In this method, the shape of the hit tower spectrum at low $p_{\rm T}$ assumed constant over all towers. A typical tower spectrum is fitted at low $p_{\rm T}$ by a simple falling exponential form ($dN/dE = \exp(E/k_i)$), then spectrum fitting for all towers and scale correction factor is applied to each tower energy.

Figure 3.8 and 3.9 show the π^0 peak position and width applied the energy scale calibration in east and west arm, respectively. The $p_{\rm T}$ threshold is required for the target of calibration towers ($p_{\rm T} > 0.8$ GeV/c) and for associate towers ($p_{\rm T} > 0.2$ GeV/c). The failing towers both π^0 peak and $E_{\rm core}$ slope corrections are marked as "dead tower", then removed from the analysis. Number of calibrated towers is summarized in Table 3.1. The detail result of energy scale calibration is described at [60].

3.4.5 Shower Merging Effect

There is a possibility of forming the same cluster by the two emission particles resulting from the decay of a high $p_{\rm T}$ parent particle due to the clustering algorithm and the limited size of each segment of EMCal. The opening angle between the pair particles narrows by rising of parent $p_{\rm T}$.

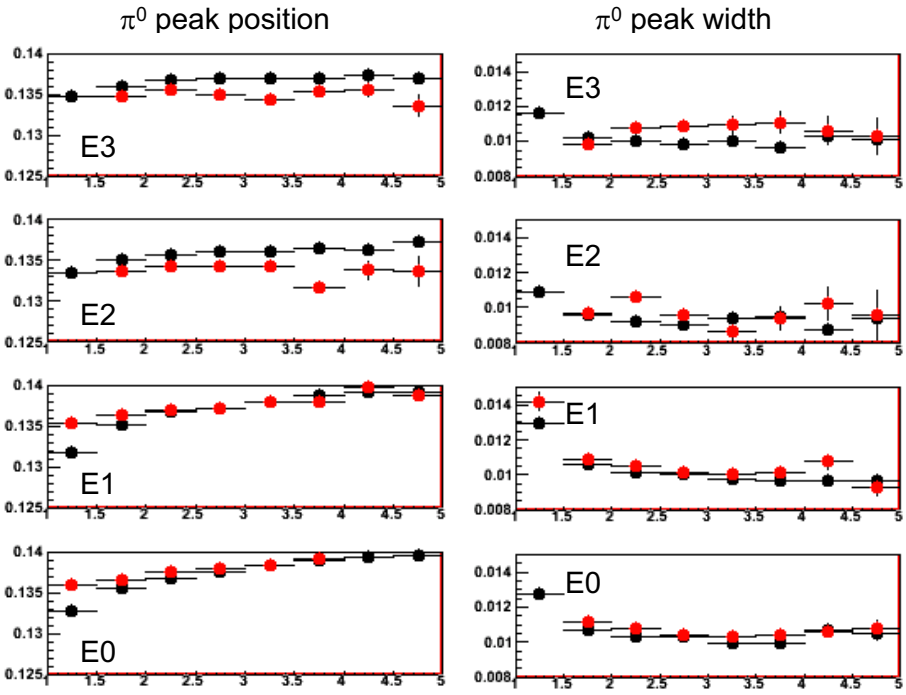

Figure 3.8: The calibrated π^0 peak position and width at each sectors in east arm [60]. Black markers show the calibrated by π^0 method, and red markers indicate that the $E_{\rm core}$ slope correction is included.

Table 3.1: Number of calibrated tower of PHENIX EMCal at Year-7.

Sector	π^0 peak correction	Applied the slope slop correction	Dead towers	Total towers
W0	2247	341	4	2592
W1	2231	347	14	2592
W2	2258	304	30	2592
W3	1669	540	383	2592
E0	2170	2208	230	4608
E1	2678	1838	92	4608
E2	2170	348	74	2592
E3	2023	477	92	2592

Roughly when the distance of hit position less than 11 cm (which is corresponding to $p_{\rm T} > 12$ GeV/c,) on the surface of EMCal, two particles formed the same peak area because the segment size of PbSc is 5.5 cm $\times$ 5.5 cm and the Moliere radius ($R_{\rm M}$) is about 3 $\sim$ 4 cm.

The effect of shower merging for the π^0 decay photons ($\pi^0 \rightarrow \gamma\gamma$) has been studied by using π^0 single simulation based on GEANT. Figure 3.10 shows the π^0 survival probability from merging effect at each detectors. Although the shower merging effect is negligible in low $p_{\rm T}$ region, the influence gradually grows above 12 GeV/c, then π^0 detection efficiency becomes 30% or less at 20GeV/c. In the π^0 v_2 analysis, the influence of shower merging in high $p_{\rm T}$ is considered as a

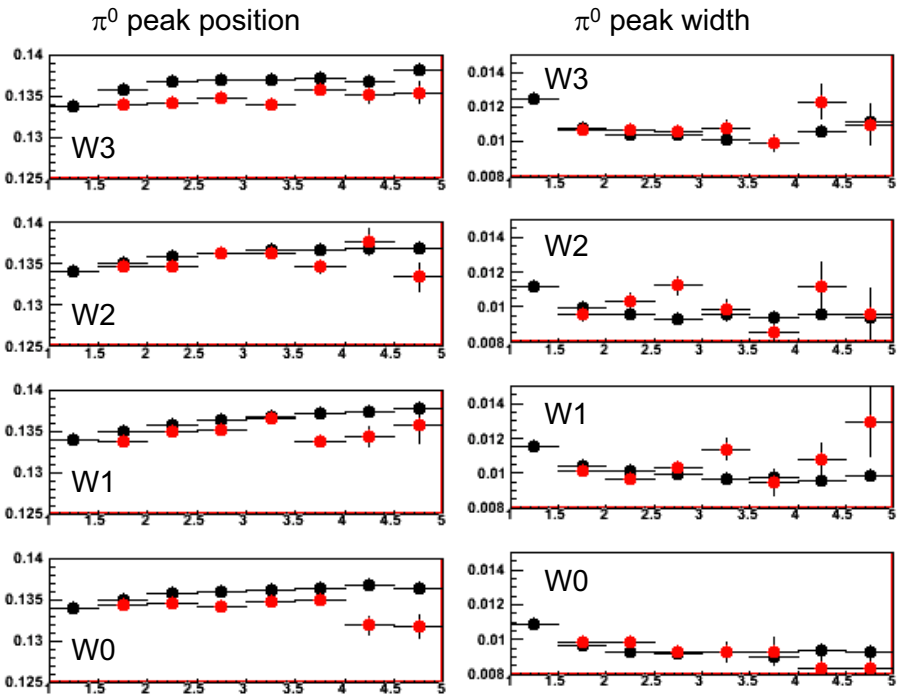

Figure 3.9: The calibrated π^0 peak position and width at each sectors in west arm [60]. Black markers show the calibrated by π^0 method, and red markers indicate that the $E_{\rm core}$ slope correction is included.

systematic error, and described later (Sec. 3.7.5).

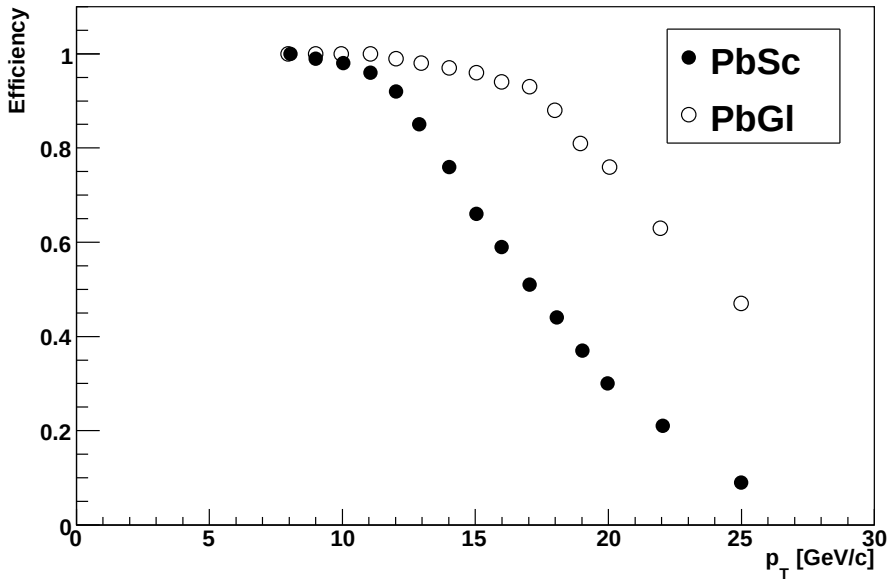

Figure 3.10: The π^0 efficiency from shower merging effect calculated by GEANT simulation for PbSc (filled circle) and PbGl (opened circle).

3.5 Photon Identification

The energy of particles is measured by using EMCal based on the core cluster algorithm which is described in the previous section. In the following photon analysis, additional cuts are required to reconstruct the core energy ($E_{\rm core}$) for photon identification.

- Energy threshold for $E_{\rm core}$,
- Bad tower rejection,
- Shower shape profile test using χ^2,
- Charged particle rejection.

At first a loose energy threshold cut (E>0.2 GeV) is applied to exclude the dust clusters, since a lot of small fragment clusters which have energy of about 100 MeV are constructed due to the PHENIX clustering algorithm. The bad condition towers which have been identified on the online analysis should be removed from analysis. Then, electromagnetic showers are distinguished between photons/electrons and hadrons by using the shower shape profile, because the pattern of energy deposit is quite different. After that, photon candidate clusters are selected by associating the photon candidates with charged particle hits in PC3 (Section 2.5) in front of EMCal for the charged particle rejection.

3.5.1 Warm, Hot and Dead Towers

In the PHENIX EMCal, bad condition towers are recognized by the "bad tower map", which is defined by following rules,

Warn map	;	high frequency of hits in the low energy (< 2 GeV) region
Hot map	;	high frequency of hits in the high energy region
Dead map	;	low frequency or no hits

The "bad tower map" is identified online analysis before data reconstruction by the total number of hits, the integrated energy, and the average per event energy for each tower. The high frequency towers which hit higher than 5σ of the hit frequency per tower in the belonging sector is tagged as "Warn tower" (in low energy region), or "Hot tower" (in high energy region). Low frequency towers which hit lower than 5σ of the hit frequency per tower is tagged as "Dead tower". The towers that failed in energy scale calibration are also added to "Dead tower" map. The "bad" towers and their around 3×3 towers are excluded from following analysis because the 3×3 towers are used for core clustering in the clustering algorithm. In addition, the towers on edge of each sector are also removed from analysis because a shower shape is not able to reconstruct correctly from these towers.

3.5.2 Shower Shape Profile Test for EM Shower

Since the shower shape of deposit energy resulting from photons/electrons and hadrons is quite different, electromagnetic showers can be identified by using a shower shape profile. The shower

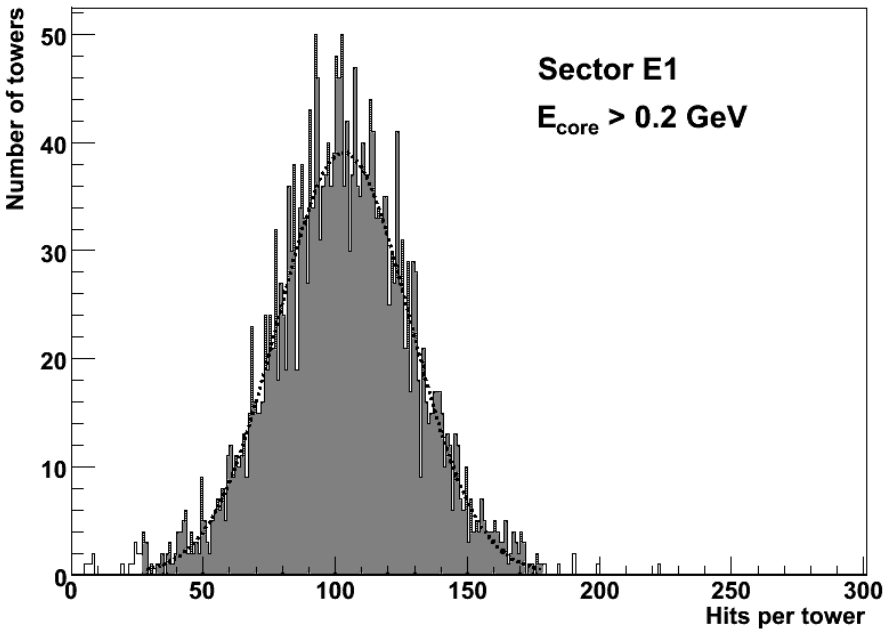

Figure 3.11: Hit distribution per tower in east sector 1. Line shows the fitting function by gaussian. The towers out of 5σ denote as bad towers.

shape parameter is given by,

$$\chi^2 = \sum_i \frac{(E_i^{\text{pred.}} - E_i^{\text{meas.}})^2}{\sigma_i^2} \tag{3.44}$$

where $E_i^{\text{meas.}}$ is an energy in $i-$th tower after calibration and $E_i^{\text{pred.}}$ is a predicted energy which is parametrization by Eq. (3.36). The variance of the predicted energy function (σ_i) is estimated by Eq. (3.42) as a function of $E_i^{\text{pred.}}$, E_{tot} and hit position. This χ^2 value reflects how a particular shower is a "electromagnetic" one. An important new feature of this model is that the fluctuations are also parameterized. Therefore the resulting χ^2 distribution is close to the theoretical one and it is nearly independent of the energy or the impact angle of electron. The χ^2 distributions for 2 GeV/c electrons and pions are shown in Fig. 3.12. The arrows indicate the χ^2 cut corresponding to 90% electron efficiency, and corresponding to $\sim$ 20% pion efficiency. The shower shape of photon is well known to be the almost same as electron shower excepting the starting point of energy deposit in the EMCal. This difference causes a small disagreement in the energy scale ($\sim$2%) because of the attenuation in the WLS fiber, then the correction for this contribution was performed. According to determination based on the signal-to-noise ratio and detection efficiency, the $\chi^2 < 3$ is required for photon identification.

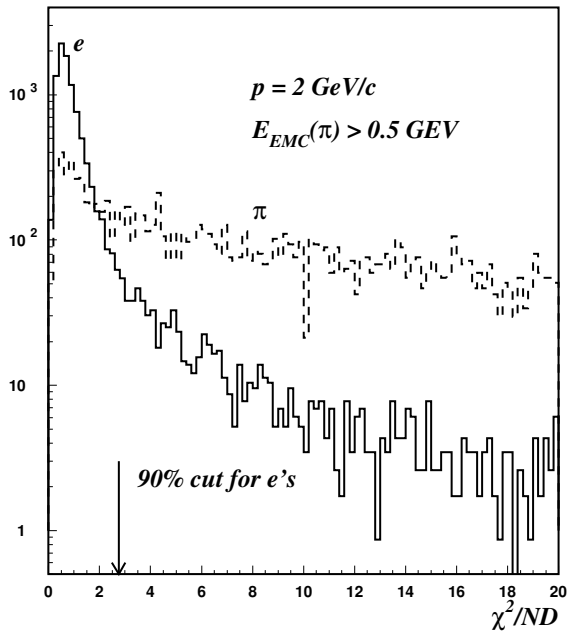

Figure 3.12: The shower shape parameter χ^2 distribution induced by 2 GeV/c electrons and pions in the PbSc.

3.5.3 Charged Particle Rejection

The deposit energy in EMCal from charged particles such as electrons from photon conversions and remaining hadrons after particle identification cuts are removed from photon candidates by using the charged particles tracking on the Pad Camber (PC3) which sit 5 cm away in front of EMCal. A distance of hit position between EMCal hits and PC3 hits is given by,

$$r^{\rm veto}_{\rm emc-pc3} = \sqrt{dx^2_{\rm emc-pc3} + dy^2_{\rm emc-pc3} + dz^2_{\rm emc-pc3}}. \tag{3.45}$$

The threshold value for charged particles veto cut sets 6.5 cm which is defined referring to Moliere radius ($R_{\rm M}$). Systematical uncertainties from remaining charged particles after particle identification cuts are determined by Monte-Carlo simulation, and estimated as systematical error of inclusive photon yields in Section 3.6.4.

3.5.4 Efficiency of Photon Identification Cut

The efficiency of photon identification cuts is determined by using PISA [50] based on GEANT simulation. Figure 3.13 shows the ratio of simulation input and reconstructed spectra which satisfied the photon identification cut for the photon, election, and hadron (pion). The results of

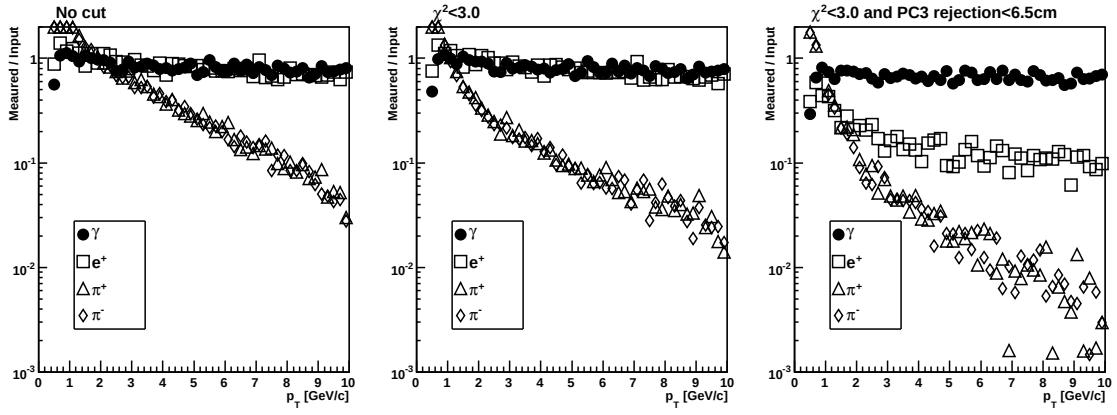

Figure 3.13: The yield ratio of input and reconstructed particles produced by Monte-Carlo for efficiency test of photon identification cuts. (Note, since the flat p_{T} distribution is assumed for the input parameter of this simulation, we have to take the amount of yield into account before particle comparison each other.)

this simulation perform good separation between photons and other particles at mid-to-high p_{T}, while there is still a remaining charged particle contamination at low-p_{T} region. The contamination of remaining particles are determined by Monte-Carlo simulation again, and subtracted in the final results.

3.6 Measurement of Inclusive Photon

Photons in the heavy-ion collisions are coming from all stages in the space-time evolution of the system, and the dominant production source of photons is the hadronic decay. Now, we start from a measurement of inclusive photon which is all identified photon experimentally by using clustering algorithm of PHENIX-EMCal, as a first step of the direct photon analysis. In this section, the procedure of raw spectra measurement, efficiency estimation and v_2 measurement of inclusive photon are described. The uncertainty of measured v_2 due to the particle identification, v_2 calculation methods, and reaction plane determination are evaluated as systematical uncertainties.

3.6.1 Raw Energy Measurement

An event trigger and centrality definition are provided by Beam-Beam Counters (BBC). Collision events for analysis are required the minimum bias trigger (Section 3.1). The invariant yield of inclusive photon per event is given by,

$$E\frac{d^3n}{dp^3} \simeq \frac{1}{2\pi p_{\rm T}} \cdot \frac{1}{N_{\rm event}} \cdot \frac{d^2N_{\rm photon}}{dp_{\rm T}dy}, \tag{3.46}$$

where, $N_{\rm event}$ is number of total event, and y is rapidity. The number of photon denoted as $N_{\rm photon}$ is given by,

$$N_{\rm photon} = \frac{1}{\epsilon_\gamma \cdot a_\gamma \cdot (1-p_{\rm c})} \cdot \left(1 - \frac{f_{\rm hadron}}{f_{\rm cluster}}\right) \cdot N_{\rm cluster}, \tag{3.47}$$

where $N_{\rm cluster}$ is a the number reconstructed clusters using the clustering algorithm and photon identification cuts, $f_{\rm hadron}/f_{\rm cluster}$ is the ratio of remaining hadron clusters to the all clusters, ϵ_γ is the efficiency, a_γ is the geometrical acceptance parameter and $p_{\rm c}$ is the probability of photon conversion.

The number of photon candidate clusters ($N_{\rm cluster}$) are counted by the selection of corresponding shower profiles for a hadronic shower rejection, and identified by associating the photon candidates with charged particle hits in the Pad Chamber (PC3) in front of the EMCal for charged particle rejection. The default values of photon selection for this analysis are;

- Bad towers : removed towers based on the bad tower map, around 3×3 area of bad tower, and sector edge
- Shower shape : $\chi^2 < 3$
- Charged particle veto : $r^{\rm veto}_{\rm emc-pc3} > 6.5$ cm

Figure 3.14 shows the cluster energy spectra of inclusive photon up to $p_{\rm T} = 16.0$ GeV/c at 10% centrality step. The spectra of each centrality are scaling as shown in legend for the clarity.

3.6.2 Correction for Inclusive Photon Yield

The measured photon yield has to be corrected for the geometrical acceptance, remaining hadrons, efficiency of photon identification cut, photon conversion at the material in front of

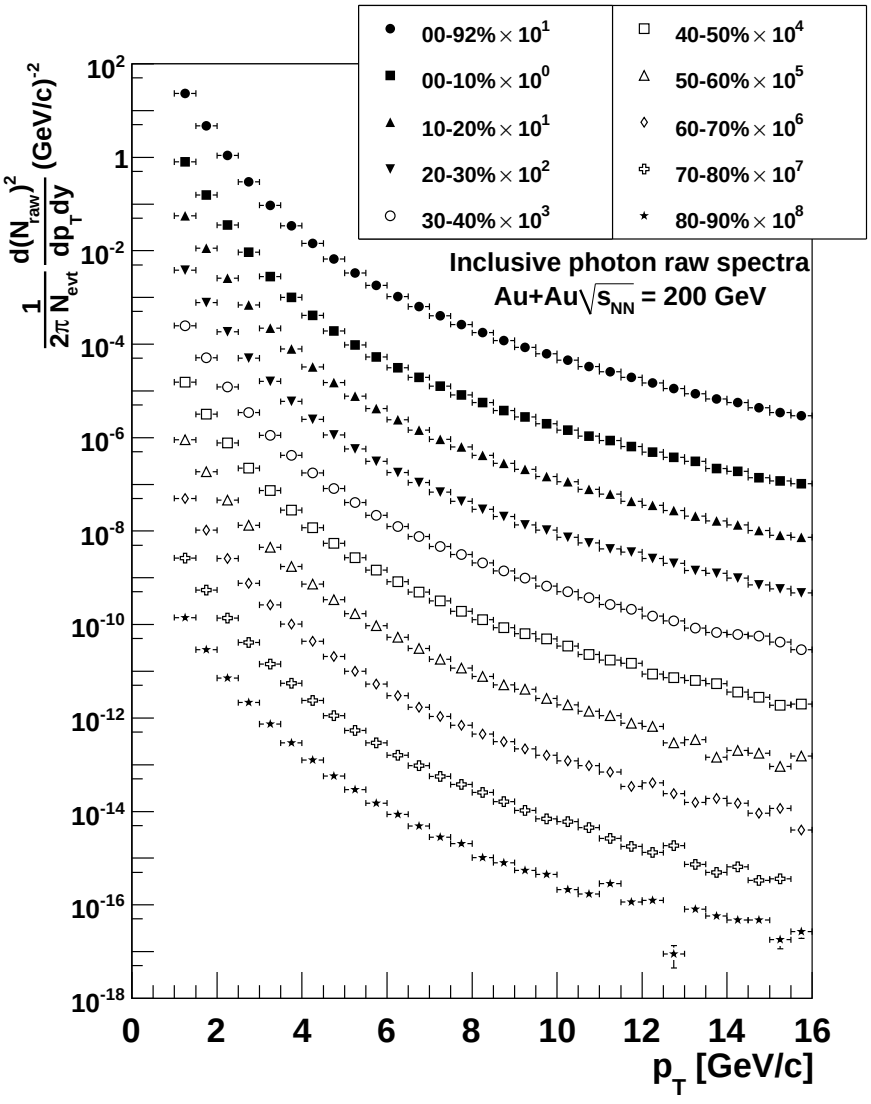

Figure 3.14: The raw energy spectra is extracted by PHENIX EMCal up to 16 GeV/c . Although it is possible to actually measure to a higher $p_{\rm T}$ range in Year-7 statistics, the data below 16 GeV/c is used for v_2 analysis, because v_2 measurement needs at least $\sim$2000 statistics in each $p_{\rm T}$ and centrality window.

EMCal, fluctuation due to the uncertainty of energy scale correction, and photons from off-vertex. The detailed study for these correction items has already been performed by using Monte-Carlo simulation and an experimental data at PHENIX Year-4.

Geometrical Acceptance Correction

A geometrical acceptance parameter (a_γ) is estimated by the GEANT simulation for the measurement of photon yield per $d\phi$. The covered area of PHENIX-EMCal in azimuth is $3\pi/4$ (for PbSc) + $\pi/4$ (for PbGl). Figure 3.15 shows the fraction of number of reconstructed single

photons by using detector response simulation for PHENIX detectors provided by PISA. The influences of dead/hot/warn towers (Section 3.5.1) are also included to the estimation of a_γ.

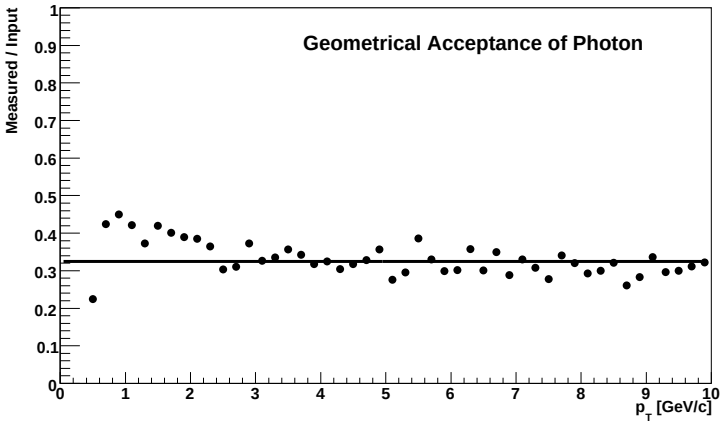

Figure 3.15: Acceptance of single photon in PHENIX-EMCal.

Remaining Hadron Correction

The hadronic contamination is rejected by using shower shape profile (χ^2) cut and charged track rejection cut effectively, but the remnant of hadronic shower still remains after photon identification cut especially in the low-$p_{\rm T}$ region as shown on Fig. 3.13. In general, hadrons have large v_2 in the Au+Au collision experiments at RHIC energy. Therefore estimated v_2 of photon candidate would be also contaminated by the hadron v_2. The relation among measured photon, hadron, and true inclusive photon is given by,

$$N^{\rm meas.} v_2^{\rm meas.} = N^{\rm inc.} v_2^{\rm inc.} + N^{\rm hadron} v_2^{\rm hadron} \tag{3.48}$$

$$v_2^{\rm inc.} = \frac{N^{\rm meas.} v_2^{\rm meas.} - N^{\rm hadron} v_2^{\rm hadron}}{N^{\rm inc.}} \tag{3.49}$$

$$= \frac{v_2^{\rm meas.} - (N^{\rm hadron}/N^{\rm meas.}) \cdot v_2^{\rm hadron}}{1 - N^{\rm hadron}/N^{\rm meas.}} \tag{3.50}$$

where, N^X denotes the number of inclusive, remaining hadron, and measured photon ($N^{\rm meas.} = N^{\rm inc.} + N^{\rm hadron}$), and v_2^X is its v_2 for the particle type X. The ratio of number of hadrons and measured photon is estimated by PISA simulation (which is emulated the PHENIX detectors) based on GEANT as shown in Fig 3.16. The experimental results of $\pi^{\pm}$,$K^{\pm}$, p, $\bar{p}$, and neutron are used for input parameters of event generator. From the results of Monte-Carlo simulation, hadron contamination is remaining below 6 GeV/c about 10-20%. The v_2 of measured photon is corrected by this fraction and Eq. (3.50).

Photon Conversion

The amount of conversion losses in the materials are determined in the full GEANT simulation of the single photon samples. The conversion probability in Table 3.2 gives a summary of conversion loss. For instance, the 10.1% of all photons are converted to e^+e^- before entered

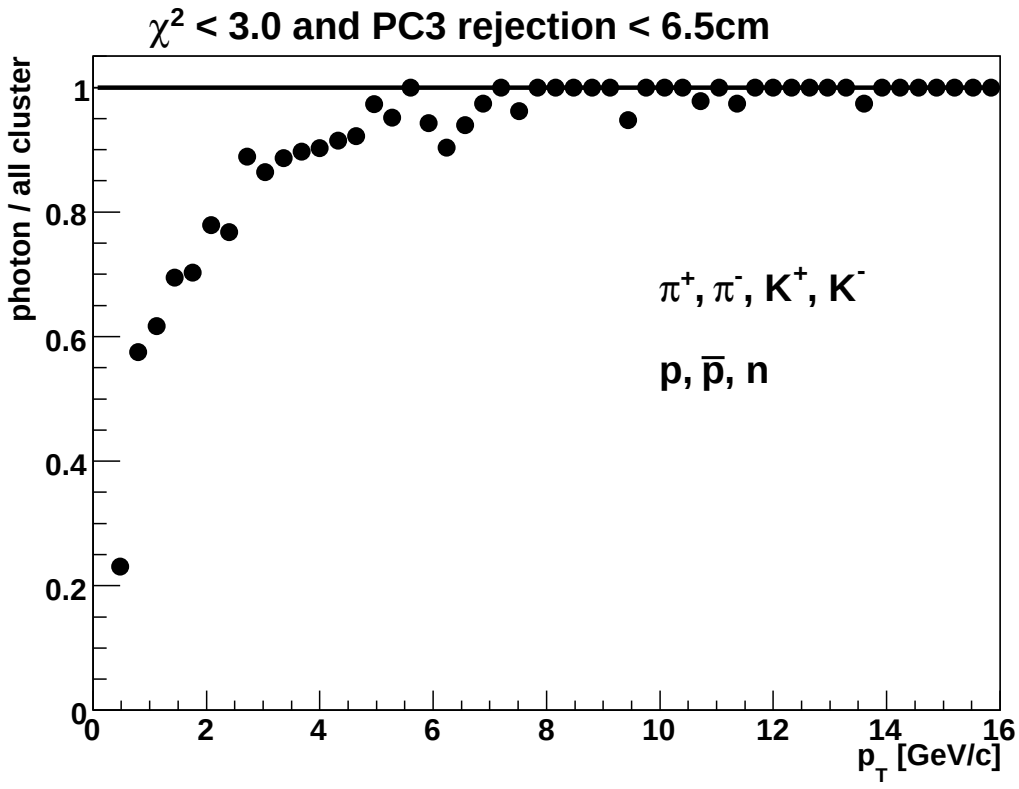

Figure 3.16: The fraction of photon candidate and clusters of $\pi^{\pm}$, $K^{\pm}$, p, $\bar{p}$, and neutron after photon identification selection.

Table 3.2: Material budget in front of EMCal

Material	Conversion probability in the West (East) arm (%)
Beam pipe + air/He bag + DC	1.3
PC1	1.2
RICH	3.2
PC2	2.1
AGEL	6.2
TEC	(5.6)
PC3	2.3
TOF	(1.2)

to sector W0. However, the majority of conversions conserve the energy of primary photon and satisfies the selection cuts for photons, because the opening angle of the e^+e^- pair is vary small and magnetic field is negligible in the detectors settled area. According to the result of the single photon simulation for the sector W0, 8.7% of all photon converted to e^+e^- pairs but reconstructed as photon. The only 1.4% of all photons are lost.

Energy Scale

The energy scale of energy deposit in each tower has been calibrated by using π^0 peak position and width, but a few % deviation of energy scale corresponds to the large shift in the invariant yield because of the steep falling of energy spectra. For instance, 1% uncertainly of energy scale corresponds to the uncertainty of the invariant yield of about 8%. According to the energy scale calibration using π^0 mass peak, energy scale of PHENIX-EMCal is stable within 1%, and it corresponds to less than 1% uncertainty in the v_2 analysis. Therefore, it is negligible in the v_2 measurement.

Off-Vertex Photon

Additional photons are emitted from the secondary particles (e.g. long lived particles) and secondary interactions. As a result of simulation study in Year-4 analysis [63] the contribution of off-vertex photon is estimated to be about 1% above 1.5 GeV/c in the invariant yield of photon. The uncertainty from off-vertex photon is negligible in v_2 analysis.

Bin Shift Correction

Strictly, the measured data point at a center of $p_{\rm T}$ bin is not a true $p_{\rm T}$ distribution due to the steeply falling shape of spectrum even within a small finite interval. Therefore, the data points should be shifted horizontally keeping their vertically value respecting to their average $p_{\rm T}$ (denoted as $\bar{p_{\rm T}}$), given by,

$$\bar{p_{\rm T}} = f'(\bar{p_{\rm T}})^{-1}, \tag{3.51}$$

$$= \left(\frac{1}{\Delta p_{\rm T}} \int_{p_{\rm T}^c - \Delta p_{\rm T}/2}^{p_{\rm T}^c + \Delta p_{\rm T}/2} f(p'_{\rm T}) dp'_{\rm T} \right)^{-1}, \tag{3.52}$$

where f is the measured functional form of spectra and f' is the corrected one. The $\Delta p_{\rm T}$ is the interval size of bin, and $p_{\rm T}^{\rm c}$ is the center of bin. Then corrected $p_{\rm T}$ is also represented in the results of v_2.

3.6.3 Extraction of Inclusive Photon v_2

The second harmonic coefficient parameter v_2 of the azimuthal distribution of the particles produced in heavy-ion collisions is defined by,

$$\frac{dN}{d(\phi - \Psi_{\rm RP})} \propto N_0[1 + 2v_2 \cos\{2(\phi - \Psi_{\rm RP})\}], \tag{3.53}$$

where, ϕ is azimuthal angle of emitted particles ($\phi = \tan^{-1}(p_y/p_x)$), and $\Psi_{\rm RP}$ is angle of reaction plane which is determined by BBC or Reaction Plane Detector (RxNP). Figure 3.17 shows the azimuthal distribution of inclusive photon in centrality 0 to 92%. The fitting function for v_2 extraction is also drawn in the same figure.

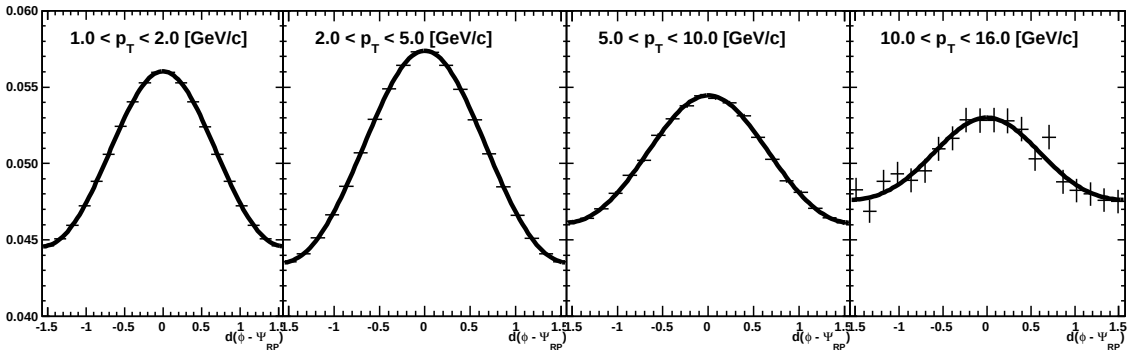

Figure 3.17: The azimuthal distribution of number of identified photon which normalized by the total count at each p_{T} bin in minimum bias. These distributions are fitted by Fourier expansion function given as $N_0[1 + 2v_2 \cos\{2(\phi - \Psi_{\mathrm{RP}})\} + 2v_4 \cos\{4(\phi - \Psi_{\mathrm{RP}})\}]$.

3.6.4 Systematical Uncertainties for Inclusive Photon v_2

In general, yield corrections for the absolute value of measured particles are unaffected to their v_2 because v_2 analysis by using the reaction plane which is calibrated to make flat in all azimuthal angle allows us physics discussions without an acceptance contamination, even if detector acceptance is not covered completely in full azimuth. Therefore, we can ignore the influence of systematical uncertainties on the particle yield estimation in the v_2 analysis if there is no bias in the azimuthal distribution of particle emissions. On the other hand, we have to estimate the remaining particle contamination included in the inclusive photon distribution, which passed the photon identification cut, because remaining hadrons expect to have a finite values for each particle species. In addition, due to the uncertainty of the reaction plane determination, it has to propagate to v_2 analysis.

Remaining Hadron Contamination

The systematical error of remaining hadrons is propagated from the v_2 error of hadrons and counting ratio, according to Eq. (3.50),

$$\Delta v_2^{\mathrm{inc.}} = \sqrt{\left(\frac{\partial(v_2^{\mathrm{inc.}})}{\partial(v_2^{\mathrm{meas.}})}\Delta(v_2^{\mathrm{meas.}})\right)^2 + \left(\frac{\partial(v_2^{\mathrm{inc.}})}{\partial(v_2^{\mathrm{hadrons}})}\Delta(v_2^{\mathrm{hadrons}})\right)^2 + \left(\frac{\partial(v_2^{\mathrm{inc.}})}{\partial R}\Delta R\right)^2} \quad (3.54)$$

where, R denotes the ratio of number of particles ($R = N^{\mathrm{hadron}}/N^{\mathrm{meas.}}$). Figure 3.18 shows the example of remaining hadron correction, and evaluated as systematical error. The contamination comes from remaining hadron is negligible above 6 GeV/c. The systematical error of remaining hadron is shown in Table 3.3.

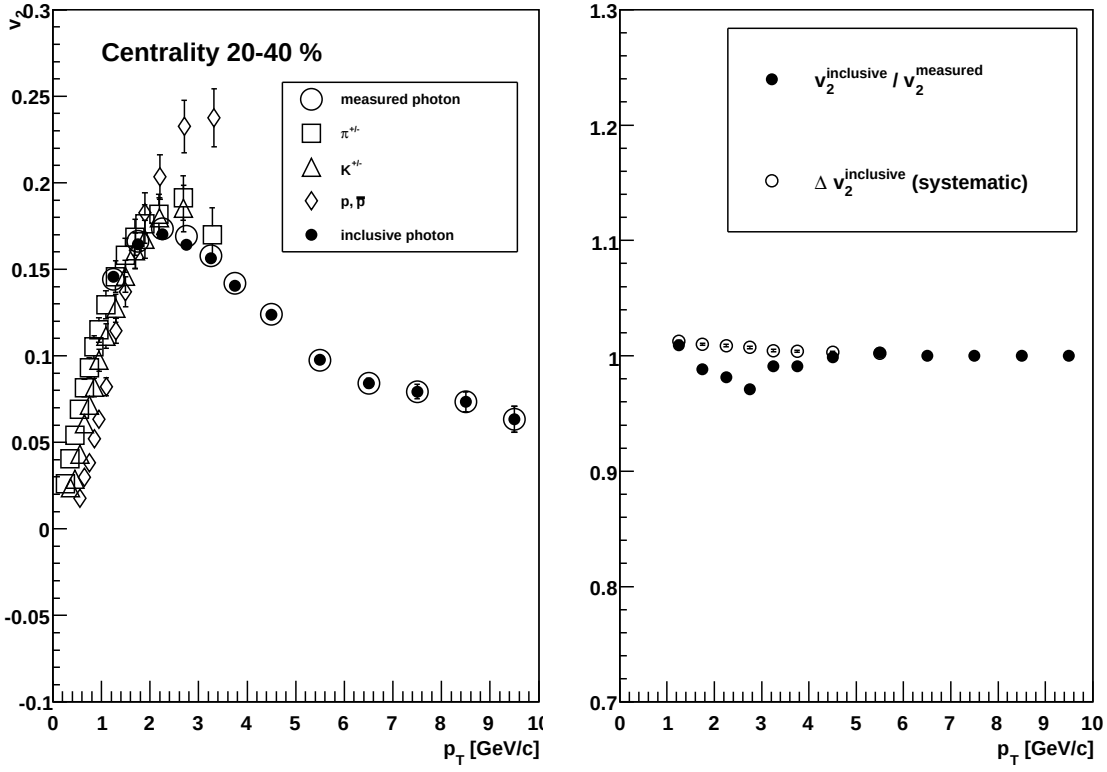

Figure 3.18: The systematical error of remaining hadron v_2. Absolute value of measured v_2 is corrected by the contamination of remaining hadron.

Table 3.3: Systematic error of remaining hadron which satisfied the photon identification cut

	p_{T}			
	$1.0 \sim 3.0$	$3.0 \sim 6.0$	$6.0 \sim 10.0$	$10.0 \sim 16.0$
$\Delta v_2^{\mathrm{inc.}}$ due to remaining hadrons	2.2%	0.9%	-	-

Uncertainty of Calculation Methods

Azimuthal anisotropy parameter v_2 of emission particles is defined by a second harmonic coefficient of Fourier expansion function as given by Eq. (3.53). The v_2 is extracted by fitted to azimuthal distribution of particles in Section 3.6.3, while it is also able to calculate from average value of cosine,

$$v_2^{\mathrm{obs.}} = \langle \cos\{2(\phi - \Psi_{\mathrm{RP}})\} \rangle \,, \tag{3.55}$$

where, $v_2^{\mathrm{obs.}}$ denotes observed v_2, experimentally. Basically, measured v_2 results from various methods should be corresponded each other, but we found a few % difference in the actual data analysis. The uncertainty of calculation methods is propagated as systematical error of final v_2 results of inclusive photon, in this thesis.

Reaction Plane Determination Error

Systematic error of reaction plane has been evaluated in [57] from following studies,

1. fluctuation of measured v_2 using the BBC south, north, and south+north combined
2. flattening procedure
3. the number of flattening coefficients
4. run-by-run dependence

First, influence of detectors which used for the reaction plane determination is estimated. Second, the errors comes from flattening correction (Section 3.3.3) are estimated by comparison of v_2 for the different flattening procedure. Third, the improvement of flattening accuracy. Finally, the stability of measured v_2 among the definite run period has studied. The systematical error of reaction plane determination is summarized in Table 3.4.

Table 3.4: Systematical error of reaction plane determination

Centrality [%]	Error [%]	Centrality [%]	Error [%]
00∼10	18.2	10∼20	7.4
20∼30	6.0	30∼40	5.7
40∼50	5.4	50∼60	5.9
00∼20	6.8	20∼40	5.9
40∼60	5.6	60∼92	16.0
20∼60	6.1	00∼92	6.3

3.6.5 Inclusive Photon v_2 Measurement

Inclusive photon v_2 is measured by PHENIX EMCal using Au+Au 200 GeV at Year-7 data set. Reaction plane is determined by BBC and RxNP, respectively. Observed v_2 has to correct by resolution of reaction plane angle as shown in Fig. 3.4,

$$v_2^{\mathrm{corr.}} = \frac{v_2^{\mathrm{obs.}}}{\sigma_{\mathrm{RP}}}. \tag{3.56}$$

The v_2 analysis is unaffected from yield corrections such as fluctuations of energy scale, detector acceptance, photon conversion and photon from off-vertex. The systematical errors for the inclusive photon v_2 are the determination of reaction plane, analysis methods and remaining hadron which satisfied the photon selection cut into account by quadratic-sum.

$$\Delta v_2^{\mathrm{inc.}} = \sqrt{(\Delta v_2^{\mathrm{Hadron}})^2 + (\Delta v_2^{\mathrm{Method}})^2 + (\Delta v_2^{\mathrm{RP}})^2} \tag{3.57}$$

The total systematical error for inclusive photon v_2 is summarized in Table 3.5, and the measured inclusive photon v_2 at $\sqrt{s_{\mathrm{NN}}} = 200$ GeV in minimum bias Au+Au collisions is shown in Fig. 3.19.

Table 3.5: Systematical error of inclusive photon v_2 in $\sqrt{s_{\rm NN}}$ = 200 GeV Au+Au collisions at PHENIX Year-7. The total error for a given $p_{\rm T}$ region is calculated by quadratic-sum of each categories.

Systematical error of inclusive photon v_2 [%]				
	$p_{\rm T}$ [GeV/c]			
centrality [%]	1.0 $\sim$ 3.0	3.0 $\sim$ 6.0	6.0 $\sim$ 10.0	10.0 $\sim$ 16.0
remaining charged hadron				
	2.2	0.9	-	-
Calculation method				
00-20	4.3	1.2	1.3	5.0
20-40	0.8	0.2	1.0	4.4
40-60	2.9	0.6	1.4	10.9
00-92	0.4	0.5	0.6	0.6
Reaction plane determination				
00-20	6.8			
20-40	5.9			
40-60	5.6			
00-92	6.3			

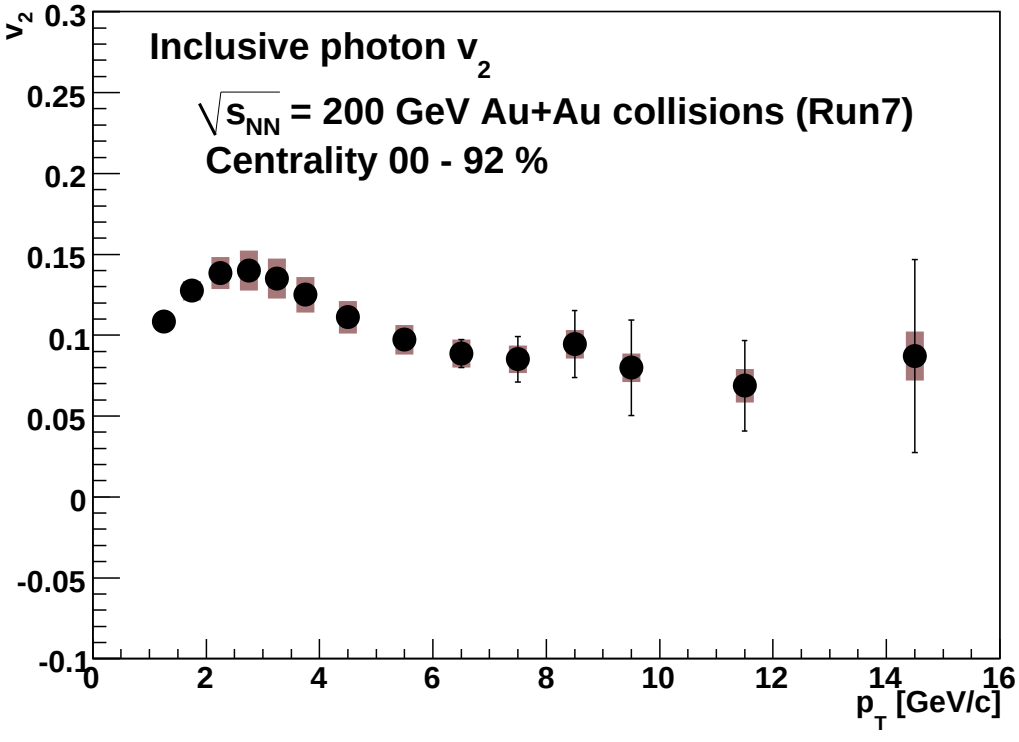

Figure 3.19: Inclusive photon v_2 at $\sqrt{s_{\rm NN}}$ = 200 GeV Au+Au collisions in centrality 0 to 92%. Black bars show the statistical errors, and boxes show the systematical errors.

3.7 Analysis For Neutral Pion

In high energy particle collision experiments, the most particles identified as photon are resulting from a π^0 decay, so we need to know the experimental π^0 distribution as a first contact for identification of the direct photon. In this section, the procedure of π^0 identification from photon candidate clusters that satisfied the photon selection cut is described. A π^0 decays two photons in the probability of 98.798±0.032% with mean-life-time τ=8.4±0.6×10^{-17}s. Since the decay particles conserve four-momentum of hadrons that are parent particles, the distribution of π^0 can be restructured by calculating the invariant mass of two photons.

3.7.1 Particle Selection Cut

The photon identification cut for π^0 v_2 analysis is basically same to the analysis of inclusive photon, such as the bad tower rejection, the low energy core cut $E_{\rm core} < 0.2$ GeV, the shower shape cut $\chi^2 < 3$, and the charged particle rejection cut. In the π^0 analysis, remaining particles in photon candidate clusters would be selected out automatically by the invariant mass calculation. For improvement of signal-to-noise ratio of a π^0 mass peak, an energy asymmetry limit is required to two photons,

$$\alpha = \frac{|E_1 - E_2|}{E_1 + E_2} < 0.8. \tag{3.58}$$

According to rejection $\alpha \approx 1$ of the angular distribution of two photons, combinatorial pairs in high-$p_{\rm T}$ are rejected effectively because the spectra of the photon candidate rapidly falling in high-$p_{\rm T}$.

3.7.2 Invariant Mass of Two Photons

The invariant mass of emission particles that is the amount of Lorentz invariance is very effective to the particle identification. The invariant mass of two photons ($m_{\rm inv.}$) is given by,

$$\begin{aligned} m_{\rm inv.} &= \sqrt{(E_1 + E_2)^2 - (\mathbf{p}_1 + \mathbf{p}_2)^2} & (3.59)\\ &= \sqrt{2E_1E_2\left(1 - \frac{x_1x_2 + y_1y_2 + z_1z_2}{l_1l_2}\right)} & (3.60)\\ &= \sqrt{2E_1E_2(1 - \cos\theta)} & (3.61) \end{aligned}$$

where, $(E_{1(2)}, \mathbf{p}_{1(2)})$ is a four-momentum of particle 1(2), $x_{1(2)}$, $y_{1(2)}$, and $z_{1(2)}$ are the hit position of emission particle 1(2), $l_{1(2)}$ is the path length from collision vertex which is determined by BBC, and θ is the opening angle of two photons.

The invariant mass and $p_{\rm T}$ are calculated for all pairs of two clusters in a given event (real event) within the same sector. In case of emitted two photons from a π^0 decay, the invariant mass of two photons in a real event makes sharp peak in the invariant mass area of π^0 ($\sim$ 135 MeV/c^2). The invariant mass distribution of two photons is calculated experimentally for each class of centrality, azimuthal angle with respect to the reaction plane $d(\phi - \Psi_{\rm RP})$, and $p_{\rm T}$. Figure 3.20 shows a sample of the invariant mass distribution of two photons.

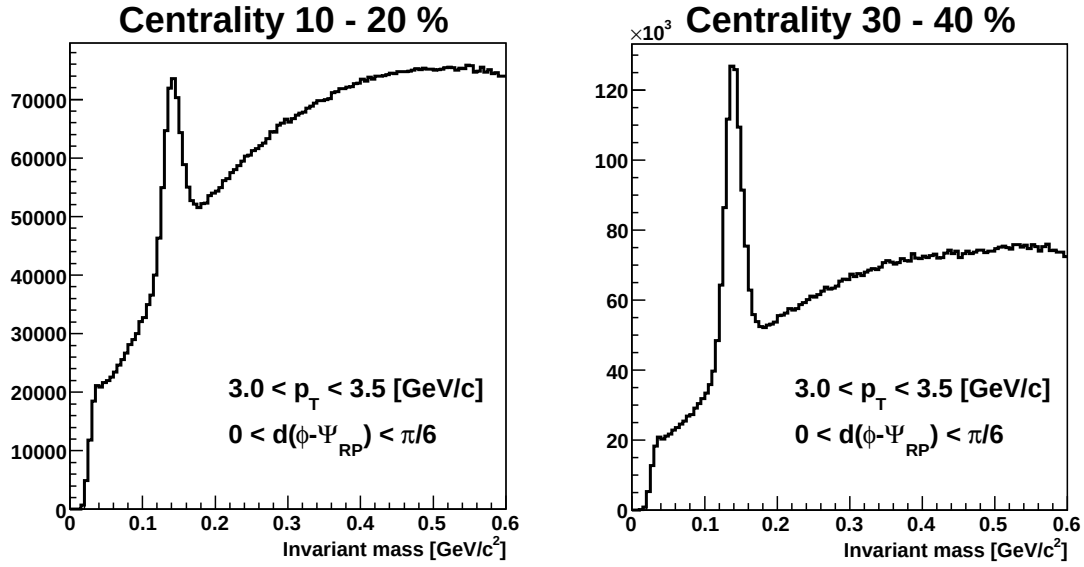

Figure 3.20: The invariant mass distribution of two photons in the $p_{\mathrm{T}} = 3.0$ to 3.5 GeV/c with centrality 10 to 20% and 30 to 40%, respectively.

3.7.3 Combinatorial Background by Event Mixing

In the invariant mass calculation, photon pairs resulting from different parent particles make a combinatorial background of a real event due to the values of invariant mass and p_{T} are calculated from all cluster pairs. For the reproduction of only the combinatorial background distribution, the distributions of two photons which are measured at different collision events each other are calculated (mixed event) in same time. The candidate events for using as the mixed calculation are selected by their event status such as centrality, reaction plane angle, and vertex position to corresponding to the real event for reproduce the accurate combinatorial background.

In this analysis, the centrality is divided to 9 bins for mixing (0-10%, 10-20%, 20-30%, 30-40%, 40-50%, 50-60%, 60-70%, 70-80%, and 80-92%), the reaction plane angle is divided to 30 bins from -$\pi/2$ to $\pi/2$, and the vertex position is divided to 30 bins from -30cm to 30cm. The mixed event distributions are normalized for matching to real event by using the histogram entry at below and above π^0 peak.

Figure 3.21 shows the sample of invariant mass distribution of two photons with normalized the mixed event histogram and subtracted the combinatorial background to reproduce the true π^0 distribution. The raw yields of extracted π^0 are counted within 2σ from the π^0 peak position. The invariant yield of π^0 per event is given by,

$$E\frac{d^3n}{dp^3} \simeq \frac{1}{2\pi p_{\mathrm{T}}} \cdot \frac{1}{N_{\mathrm{event}}} \cdot \frac{d^2N_{\pi^0}}{dp_{\mathrm{T}}dy}, \tag{3.62}$$

where N_{π^0} denotes the number of π^0 emissions, related to measured count $N_{\pi^0}^{\mathrm{raw}}$ as following,

$$N_{\pi^0} = \frac{1}{a_{\pi^0} \cdot \epsilon_{\pi^0}} \cdot N_{\pi^0}^{\mathrm{raw}}, \tag{3.63}$$

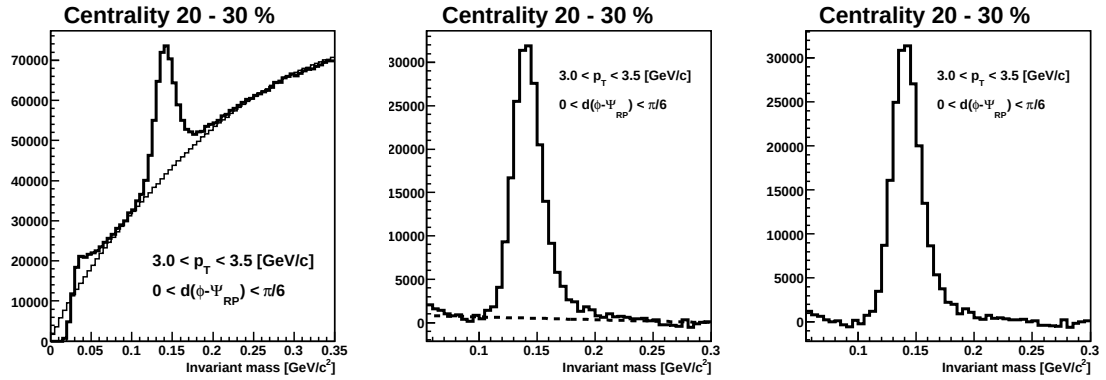

Figure 3.21: Extracted true π^0 peak from invariant mass distribution of two photons. Left figure shows the histograms of real event and normalized mix event. Middle figure shows the distribution of the combinatorial back ground is subtracted from the real histogram. The additional components are remaining in middle figure because of the hadron contamination, photon identification, or other effects. For removing this contamination, the histogram is fitted within near π^0 peak by using 1 polynomial + gaussian (dashed line). After that, true π^0 is extracted as shown in right figure.

where, a_{π^0} is the geometrical acceptance for π^0 and ϵ_{π^0} is the efficiency caused by the detector response and the procedure of particle identification.

In the v_2 measurements, we are released from the yield correction owing to flatten distribution of reaction plane when the target particles don't have the biased distribution in azimuth. Therefore $N_{\pi^0}^{\rm raw}$ is used for the estimation of azimuthal distribution of π^0. The fluctuations caused by the definition of normalized range for the mixed event and the counting procedure of the π^0 yield are included to systematical error in section 3.7.5.

3.7.4 Azimuthal Distribution of π^0

The strength of v_2 is extracted from the azimuthal distribution with respect to the reaction plane angle which is determined by using BBC or RxNP. The azimuthal angle of π^0, ϕ_{π^0}, is given by,

$$\phi_{\pi^0} = \tan^{-1}\left(\frac{p_y}{p_x}\right), \tag{3.64}$$

$$\Delta\Phi \equiv \phi_{\pi^0} - \Psi_{\rm RP} = \tan^{-1}\left\{\frac{\sin(2(\phi_{\pi^0} - \Psi_{\rm RP}))}{\cos(2(\phi_{\pi^0} - \Psi_{\rm RP}))}\right\}. \tag{3.65}$$

Definition range of azimuthal angle is turned up to $0 \sim \pi/2$ and divided to 6 bins. The measured distribution of π^0 is shown in Fig. 3.22, which is normalized by using the number of count for easy to see the magnitude dependence among each $p_{\rm T}$ bin.

The v_2 value is extracted from the Fourier expansion function and corrected using reaction plane resolution as described in Section 3.3. The fitting function is given by,

$$F(\phi - \Psi_{\rm RP}) = N_0[1 + 2v_2\cos\{2(\phi - \Psi_{\rm RP})\} + 2v_4\cos\{4(\phi - \Psi_{\rm RP})\}]. \tag{3.66}$$

For improvement the fitting accuracy (χ^2/NDF), including the v_4 term to the fit function, though it unaffected to the v_2 value itself. Measured coefficient, $v_2^{\rm obs.}$ is divided by $< \cos\{2(\Psi_1 - \Psi_2)\} >$

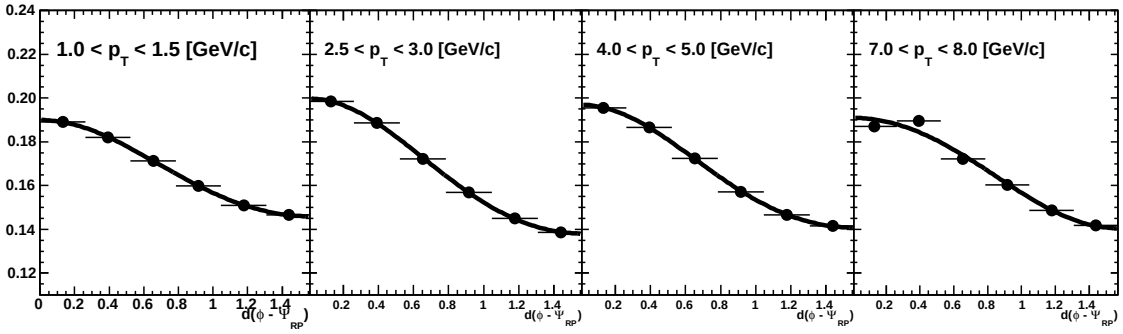

Figure 3.22: $dN/d(\phi - \Psi_{\rm RP})$ distribution for π^0 at minimum bias with 4 $p_{\rm T}$ selections. The solid lines show the fitting results of a Fourier function ($N_0[1 + 2v_2 \cos\{2(\phi - \Psi_{\rm RP})\} + 2v_4 \cos\{4(\phi - \Psi_{\rm RP})\}]$).

for the correction of reaction plane resolution (Section 3.3.2),

$$v_2^{\pi^0} = \frac{v_2^{\rm obs.}}{< \cos\{2(\Psi_1 - \Psi_2)\} >}, \tag{3.67}$$

where, $\Psi_{1(2)}$ is the reaction plane angle of detector 1(2). In this analysis, BBC north(south) or RxNP north(south) are used as detector 1(2), respectively.

3.7.5 Systematical Uncertainty of π^0

The sources of systematical error on v_2 for π^0 are evaluated from,

- Procedure of particle identification,
- Reaction plane determination,
- Cluster merging effect,

then, determine the total error by quadratic-sum.

Systematical Error from Particle Identification

The reconstructed photon candidate clusters are applied some of selection cuts such as shower shape cut χ^2, bad tower rejection cut, and charged particle rejection cut. The systematical error from the particle identification criteria are studied by the measured v_2 stability under changing of the cut definitions. In addition, we need to know the influence from the definition of normalization ranges of the event mixed distribution and the π^0 counting ranges.

Figure 3.23 (left) shows the measured v_2 by changing PID cut for π^0 and its ratio. The systematical error of PID from this study is summarized in Table 3.6. In order to get rid of the statistic contamination, actual error values are evaluated from exponential fitting function as shown in Fig. 3.23 (right).

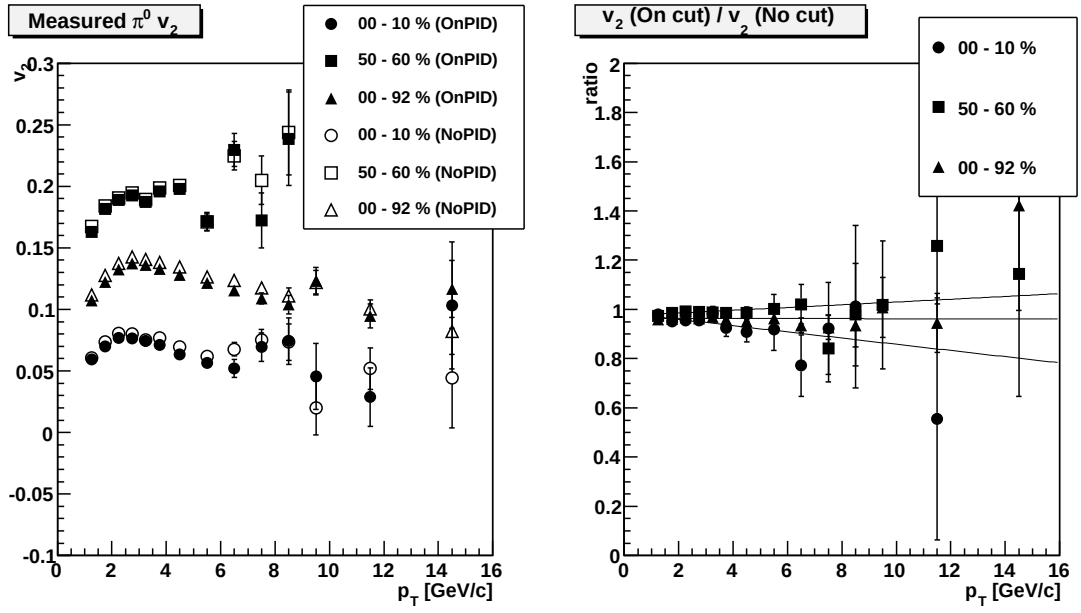

Figure 3.23: The measured π^0 v_2 with (filled symbol) and without (opened symbol) photon selection cut at each centrality selection as a function of $p_{\rm T}$ and its ratio.

Table 3.6: Systematical error from photon selection cut (χ^2 and charged particle rejection) for measured π^0 v_2.

Systematic error of photon selection cut (absolute) (relative [%]))				
	$p_{\rm T}$[GeV/c]			
centrality [%]	1.0 $\sim$ 3.0	3.0 $\sim$ 6.0	6.0 $\sim$ 10.0	10.0 $\sim$ 16.0
00 - 10	0.0031 (4%)	0.0047 (6.6%)	0.009 (17%)	0.025 (88%)
10 - 20	0.0068 (5.2%)	0.0078 (6.3%)	0.01 (14%)	0.019 (21%)
20 - 30	0.0062 (3.7%)	0.0059 (3.9%)	0.0059 (5.1%)	0.0059 (22%)
30 - 40	0.0051 (2.8%)	0.005 (2.9%)	0.005 (3.3%)	0.005 (3.3%)
40 - 50	0.0034 (1.8%)	0.0034 (1.9%)	0.0034 (2.2%)	0.0034 (4%)
50 - 60	0.002 (1%)	0.0018 (0.94%)	0.0018 (0.81%)	0.0018 (0.52%)
00 - 20	0.0047 (4.8%)	0.0061 (6.4%)	0.0086 (14%)	0.013 (21%)
20 - 40	0.0058 (3.3%)	0.0055 (3.4%)	0.0055 (4.2%)	0.0055 (7.1%)
40 - 60	0.0028 (1.5%)	0.0028 (1.5%)	0.0028 (1.5%)	0.0028 (1.7%)
20 - 60	0.0049 (2.8%)	0.0047 (2.8%)	0.0047 (3.1%)	0.0047 (4.2%)
60 - 92	0.0033 (1.6%)	0.0073 (2.9%)	0.02 (5.3%)	0.079 (16%)
00 - 92	0.0048 (3.7%)	0.0053 (4%)	0.0065 (5.7%)	0.012 (13%)

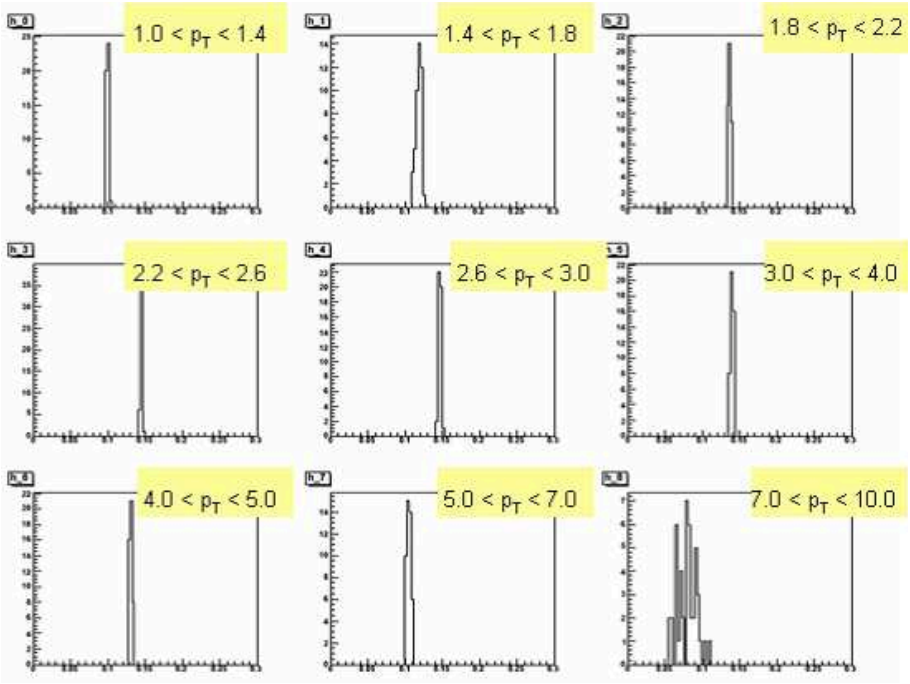

Figure 3.24: The fluctuation of measured v_2 when changing the normalized range of mixed distribution and particle counting range.

Table 3.7: Systematical error from normalization of event mixed distribution and particle counting range on the invariant mass for π^0 v_2.

Systematic error of normalization and counting range (absolute) (relative [%]))				
	p_{T}[GeV/c]			
centrality [%]	1.0 $\sim$ 3.0	3.0 $\sim$ 6.0	6.0 $\sim$ 10.0	10.0 $\sim$ 16.0
00 - 10	0.00099 (1.3%)	0.0017 (2.4%)	0.0042 (7.7%)	0.021 (54%)
10 - 20	0.00074 (0.57%)	0.0015 (1.3%)	0.0035 (4.9%)	0.011 (12%)
20 - 30	0.00072 (0.44%)	0.0015 (1%)	0.0041 (3.5%)	0.017 (1e+02%)
30 - 40	0.00071 (0.38%)	0.0012 (0.7%)	0.003 (1.9%)	0.013 (8.5%)
40 - 50	0.00094 (0.49%)	0.0014 (0.77%)	0.0031 (1.9%)	0.019 (30%)
50 - 60	0.00085 (0.45%)	0.0015 (0.78%)	0.0044 (1.8%)	0.028 (7.6%)
00 - 20	0.00083 (0.84%)	0.0015 (1.6%)	0.0037 (5.8%)	0.014 (21%)
20 - 40	0.00066 (0.38%)	0.0012 (0.77%)	0.0029 (2.2%)	0.01 (14%)
40 - 60	0.00082 (0.43%)	0.0011 (0.62%)	0.0026 (1.4%)	0.017 (10%)
20 - 60	0.00059 (0.33%)	0.00096 (0.57%)	0.0023 (1.5%)	0.012 (11%)
60 - 92	0.0012 (0.61%)	0.0029 (1.1%)	0.0093 (2.7%)	0.058 (12%)
00 - 92	0.00059 (0.45%)	0.0011 (0.87%)	0.0025 (2.1%)	0.0068 (7.2%)

Systematical Error from Reaction Plane Determination

The p_{T} independent systematical error from reaction plane determination has been summarized in previous section (Section 3.6.4) for the inclusive photon analysis. These values are also applied to v_2 of π^0 measurement.

Cluster Merging Effect of π^0 v_2

The photon pairs resulting from a high-p_{T} π^0 decay would form the same local maximum tower due to the segment size of EMCal and clustering algorithm, as a described already in section 3.4.5. The shower merging cluster would be rejected automatically from the analysis by the shower shape profile test, so the amount of the measured particle decreases. The systematical correction for cluster merging effect has to be considered above GeV/c, because the opening angle of the pair particles narrows less than discrimination possibility of detectors. Figure 3.25 shows the distance of hit positions between the two photons pair on the surface of EMCal (ΔR) as a function of p_{T} (left figure), and the merging probability if we define the merging threshold as 8cm (right figure). Although there is no merging effect below ∼12 GeV/c, about 30% of π^0 emissions are losses at 16 GeV/c.

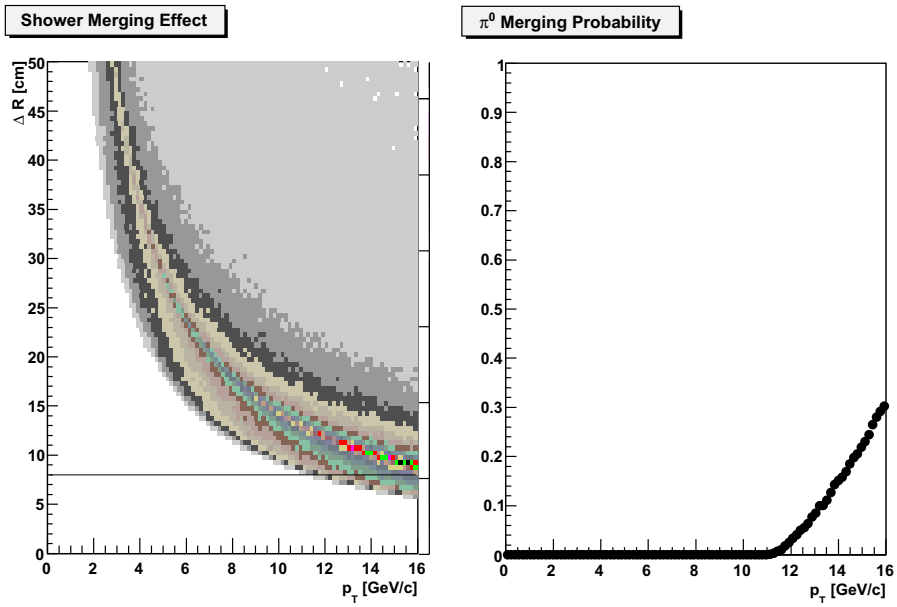

Figure 3.25: (Left) The distance on the EMCal surface between two particles emitted from same parent particle (ΔR) is shown as a function of p_{T}. Roughly when the distance of hit position less than 8cm, two particles formed a same peak area above 12 GeV/c. (Right) The cluster merging probability when the threshold of ΔR is defined as 8 cm.

In general, the number of shower merging clusters grows with a multiplicity of emission particles. Therefore, it might be produced the extra bias between in-plane and out-plane of the $dN/d\phi$ distribution. The estimated influence of cluster merging effects to $dN/d\phi$ of π^0 by using Monte-Carlo simulation is shown in Fig. 3.26. At first, the experimental $dN/d\phi$ distributions of parent

particles are parameterized using the measured π^0 v_2 for the input parameter of simulation. This input distributions are able to reconstructed correctly from simulated decay particles (shown as the solid histogram in Fig. 3.25). At the same time, another distribution is also reconstructed which is applied the threshold of ΔR to the two decay photons (shown as the dashed histogram). From the results of these processes, we obtained the π^0 dN/ϕ distribution with/without effects of merging cluster, there is apparent difference between them above 12 GeV/c.

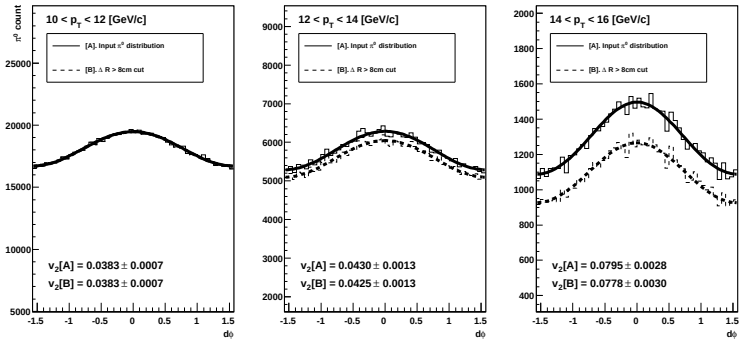

Figure 3.26: The reconstructed $dN/d\phi$ distributions of parent particle from $\pi^0 \to 2\gamma$ simulation are shown using the measured π^0 v_2 value for the input parameter. The solid histograms are the reconstructed π^0 distribution from simulated decay photons, and the dashed line histogram is generated by almost same process but applied of $\Delta R < 8$cm cut for reconstructed particle. The solid and dashed line is the fitting function to extract their v_2.

Figure 3.27 shows the calculated v_2 from reconstructed $dN/d\phi$ distributions and its ratio. There is no more than 4% difference between them around 14 GeV/c. The influence of cluster merging effect to π^0 v_2 is included to systematical error at only high-p_{T} region.

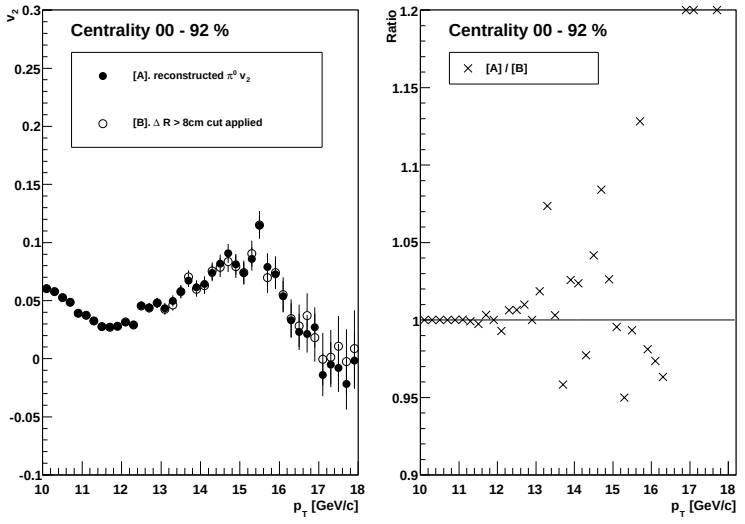

Figure 3.27: Re-estimated v_2 of π^0 from $\pi^0 \to 2\gamma$ simulation. The results are corresponding completely below 12 GeV/c so negligible of the influence from cluster merging effect in low-p_{T} region. On the other hand, there is about 4% difference around 14 GeV/c.

Summary of Systematical Error for π^0 v_2

Table 3.8 shows the summary of systematical error of π^0 v_2 from particle identification procedure, definition of normalization and particle counting range, shower merging effect, and determination of reaction plane. The values are presented as relative value. The total systematical error is estimated by quadratic-sum from these contaminations.

Table 3.8: Summary of systematical error of π^0 v_2 . The values are presented as relative value. The total systematical error is estimated by quadratic-sum from these contaminations.

Systematic error of π^0 v^2				
	p_{T} [GeV/c]			
centrality [%]	$1.0 \sim 3.0$	$3.0 \sim 6.0$	$6.0 \sim 10.0$	$10.0 \sim 16.0$
π^0 identification error [%]				
00-20	4.8	6.4	14	21
20-40	3.3	3.4	4.2	7.1
40-60	1.5	1.5	1.5	1.7
00-92	3.7	4	5.7	1.7
Normalization and π^0 counting range				
00-20	0.84	1.6	5.8	21
20-40	0.38	0.77	2.2	14
40-60	0.43	0.62	1.4	10
00-92	0.45	0.87	2.1	7.2
Shower merging effect				
00-92	-	-	-	4
Reaction plane determination				
00-20	6.8			
20-40	5.9			
40-60	5.6			
00-92	6.3			

3.7.6 The Result of π^0 v_2 in Minimum Bias

As described in this section, the v_2 of π^0 is calculated from invariant mass distribution of two photons, and fitting by the Fourier expansion function. The angle of reaction plane is determined using BBC and RxNP, respectively as shown in Fig. 3.28. The systematical error is estimated from particle identification procedure, definition of normalization range of event mixed distribution, shower merging effect, and determination of reaction plane. The total systematical error is propagated by quadratic-sum.

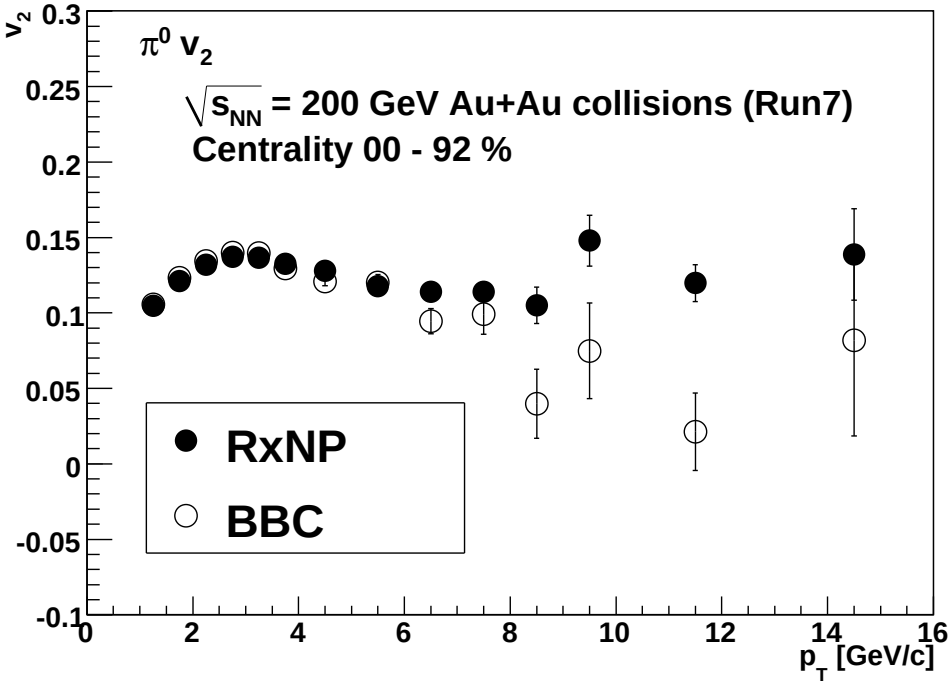

Figure 3.28: The measured v_2 of π^0 π^0 v_2 in $\sqrt{s_{\rm NN}}$ = 200 GeV at minimum bias Au + Au collisions up to $p_{\rm T}$ = 16 GeV/c. Reaction plane angle is determined by using RxNP and BBC, and their v_2 are calculated, respectively.

3.8 Extraction of Azimuthal Anisotropy of Direct Photon

The direct photon yield is measured experimentally by the subtraction of hadronic decay photon from the inclusive photon distribution. Since a main source of the hadronic decay photon contamination is π^0 emission, it has been measured in the Section 3.7 by using $\pi^0 \to 2\gamma$ decay mode. Before extraction of the v_2 direct photon, we have to know the other influence of particles which have capability of decaying to photon. In this section, the estimation method of hadronic decay photon, the excess ratio of direct photon respecting with inclusive photon, and the procedure of direct photon measurement are described.

3.8.1 Estimation of Hadronic Decay Photon

Since components besides π^0 are not measured directly even η meson as a secondary contribution, the photons from hadrons are estimated by Monte-Carlo simulation. The branching ratio of mesons decaying to photon is summarized in Table 3.9.

Table 3.9: Decay kinematics of hadrons to photon. These ratio is referred from "Particle Physics booklet" in 2006.

hadron	invariant mass (MeV/c^2)	decay mode	ratio (%)
π^0	134.98	2γ	98.798 ± 0.032
		$e^+\ e^-\ \gamma$	1.198 ± 0.032
η	547.8	2γ	39.33 ± 0.25
		$e^+e^-\gamma$	$(4.9 \pm 1.1) \times 10^{-3}$
		$\pi^0 2\gamma$	$(7.1 \pm 1.4) \times 10^{-4}$
		$\mu^+\mu^-\gamma$	$(3.1 \pm 0.4) \times 10^{-4}$
ω	782.6	$\eta\gamma$	$(6.5 \pm 1.0) \times 10^{-4}$
		$\pi^0\gamma$	8.5 ± 0.5
ρ^0	769.0	$\pi^+\pi^-\gamma$	$(9.9 \pm 1.6) \times 10^{-3}$
		$\pi^0\gamma$	$(6.8 \pm 1.7) \times 10^{-4}$
		$\eta\gamma$	$(2.4 \pm 0.8) \times 10^{-4}$
η'	957.8	$\rho^0\gamma$	29.5 ± 1.0
		$\omega\gamma$	3.03 ± 0.31
		2γ	2.12 ± 0.14
		$\mu^+\mu^-\gamma$	$(1.04 \pm 0.26) \times 10^{-4}$

The ratio of yield for η meson to π^0 are referred experimental results in [53] approximately 0.45, and applied same amount of π^0 for other contributions. Azimuthal anisotropy of parent particles except π^0 estimated from $KE_{\rm T}$ scaled π^0 v_2 under the assumption of $KE_{\rm T}$ scaled v_2 is unity among all emission hadrons in the heavy-ion collisions [57]. The parameter, $KE_{\rm T}$ is given by,

$$KE_{\rm T} = \sqrt{p_{\rm T}^2 + m_0^2} - m_0, \tag{3.68}$$

where, m_0 is an invariant mass of emission hadrons. In Fig. 3.29 shows the measured v_2 of π^0 and estimated v_2 of other parent hadrons by using $KE_{\rm T}$ scaled π^0 v_2 , and Fig. 3.30 shows the

results of Monte-Carlo simulation of particle decay kinematics for π^0 , η, ω, ρ, and η'. The error bars for v_2 of hadronic decay photon are propagated from π^0 as shown the up and down lines around data points.

In Fig. 3.31, the p_{T} slopes of each parent particle are estimated with respecting the m_{T} scaling. Data points are experimental invariant yield of π^0 as shown in left figure, and the fraction of each contribution is shown in right figure.

Finally, estimated v_2 of each parent hadron are cocktailed referring to fraction of each contribution as shown in Fig. 3.32. The contribution of hadronic decay photon v_2 is mainly π^0 ($\approx$ 77.6%), and secondary contribution is η ($\approx$ 19.0%).

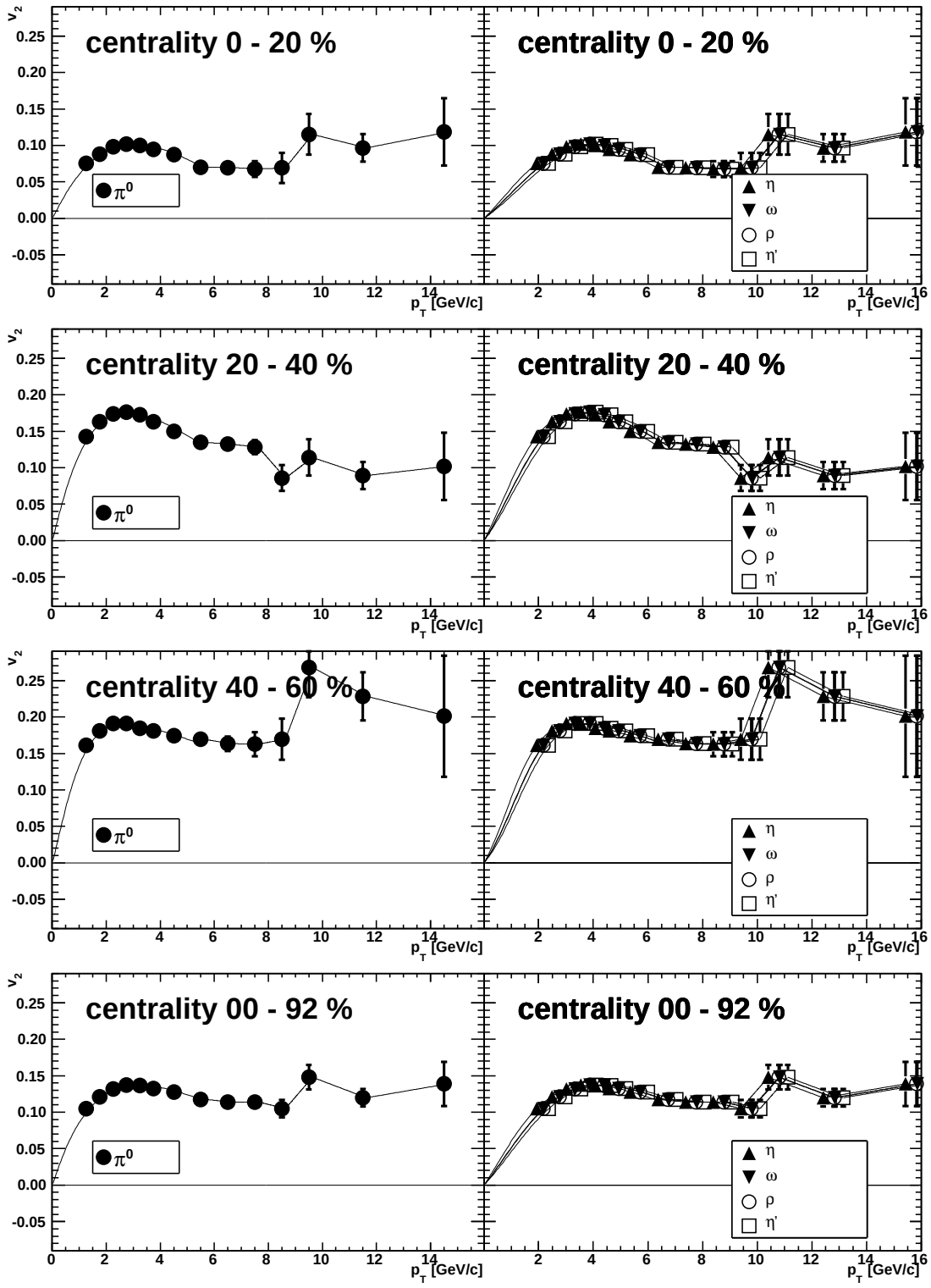

Figure 3.29: Estimated v_2 of parent hadrons for input of Monte-Carlo simulation at 4 centrality selections. Lines show the fitting results for each particles.

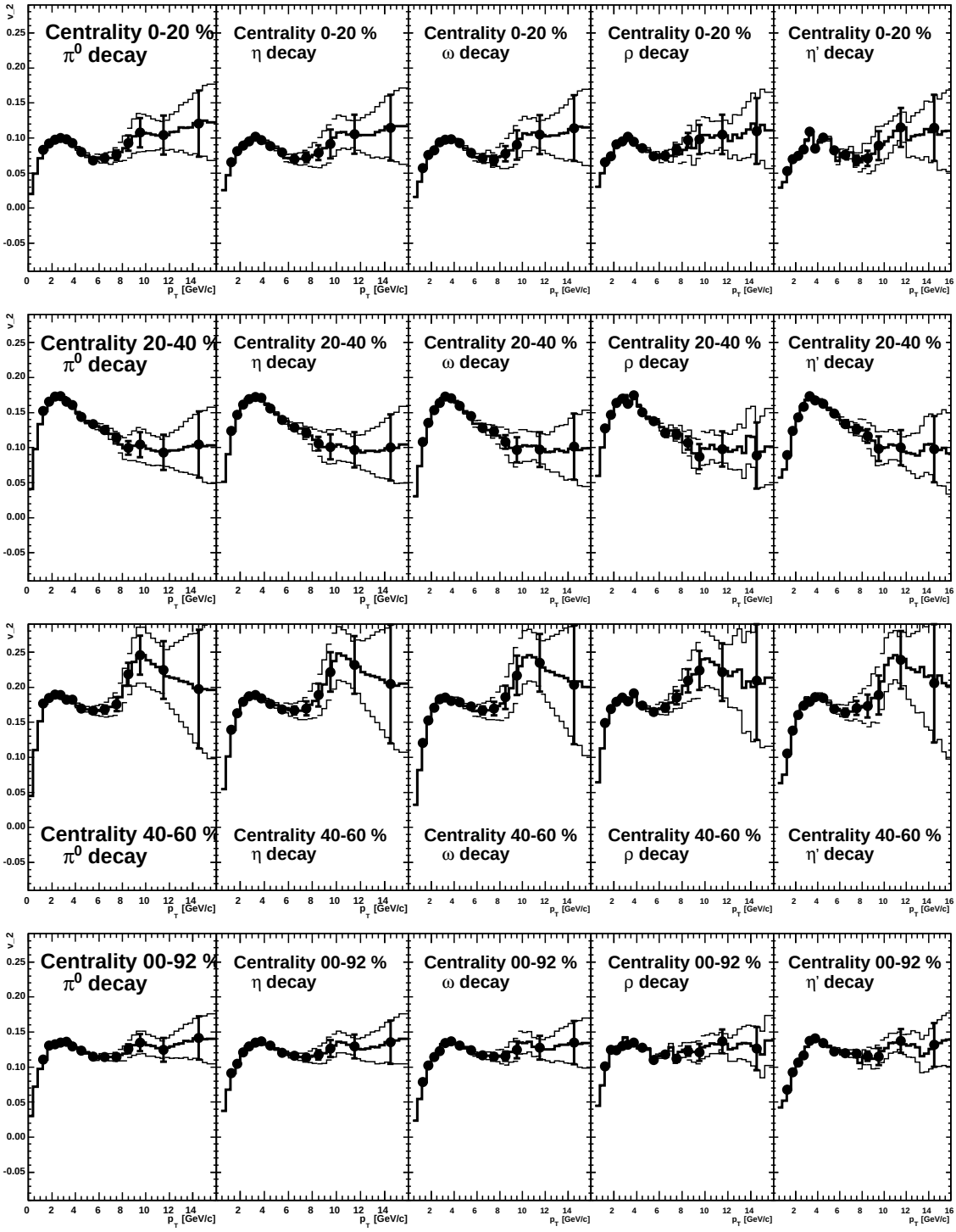

Figure 3.30: Hadronic decay photon v_2 of π^0, η, ω, ρ, and η' in $\sqrt{s_{\rm NN}} = 200$ GeV at 4 centrality selections Au+Au collisions. The systematical and statistical error is propagated from π^0 v_2 as shown the up and down lines around data points.

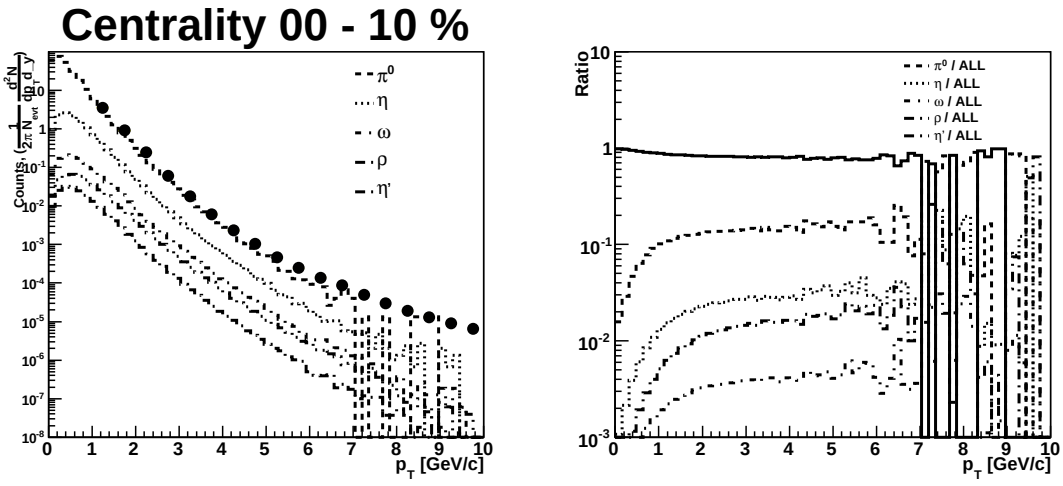

Figure 3.31: (Left): Input p_{T} spectra for particle decay simulation, compared with experimental measurements of π^0 spectra. (Right): Contribution ratio to back ground photon from each decay particles.

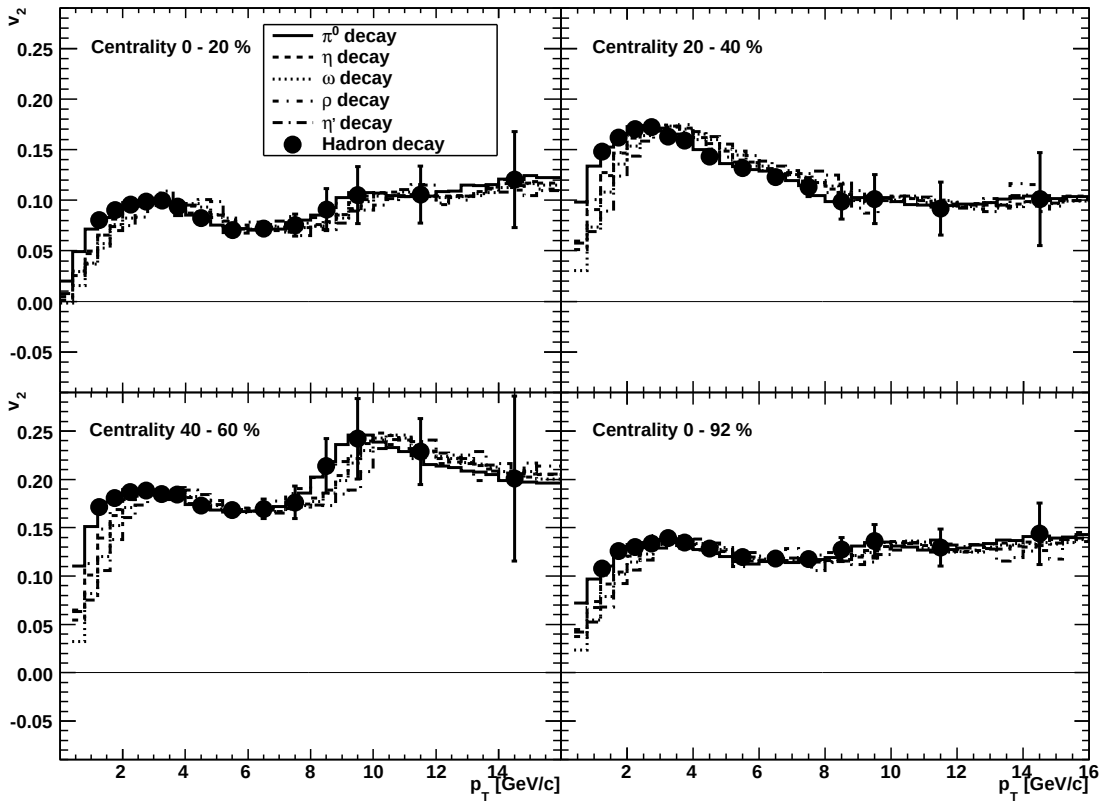

Figure 3.32: Cocktailed v_2 of hadronic decay photon from π^0, η, ω, ρ, and η'.

3.8.2 Excess Ratio of Direct Photon

Direct photon is defined as remaining photons after subtracting the hadronic decay photons inclusive photons. The v_2 as a second coefficient parameter of Fourier expansion function are independent value for each particle. Therefore v_2 of each emission particle is discriminated by using its yield as weight. In the direct photon case, its v_2 is given by,

$$N^{\mathrm{direct}} = N^{\mathrm{inclusive}} - N^{\mathrm{bg}} \tag{3.69}$$

$$N^{\mathrm{direct}} v_2^{\mathrm{direct}} = N^{\mathrm{inclusive}} v_2^{\mathrm{inclusive}} - N^{\mathrm{bg}} v_2^{\mathrm{bg}} \tag{3.70}$$

$$v_2^{\mathrm{direct}} = \frac{N^{\mathrm{inclusive}} v_2^{\mathrm{inclusive}} - N^{\mathrm{bg}} v_2^{\mathrm{bg}}}{N^{\mathrm{inclusive}} - N^{\mathrm{bg}}} \tag{3.71}$$

$$= \frac{(N^{\mathrm{inclusive}}/N^{\mathrm{bg}}) v_2^{\mathrm{inclusive}} - v_2^{\mathrm{bg}}}{(N^{\mathrm{inclusive}}/N^{\mathrm{bg}}) - 1}, \tag{3.72}$$

here, $N^{\mathrm{inclusive}}$ is measured from an energy deposit in EMCal and several correction factors (Section 3.6), and N^{bg} is calculated from Monte-Carlo simulation based on experimental π^0 results. The fraction of inclusive photon and hadron decay photon has been performed in PHENIX experiment, called "excess ratio of direct photon". In order to cancel out the energy scale contamination and systematical error, this ratio of photons are normalized by the π^0 yield as following,

$$R \equiv \frac{N^{\mathrm{inclusive}}}{N^{\mathrm{bg}}} = \frac{(N^{\mathrm{inclusive}}/N^{\pi^0})_{\mathrm{measure}}}{(N^{\mathrm{bg}}/N^{\pi^0})_{\mathrm{MC}}}. \tag{3.73}$$

Figure 3.33 shows the ratio of inclusive photon and hadronic decay photon. While there is not so many direct photon yield in low-p_{T} , large excesses are observed in high-p_{T} due to hadron suppression.

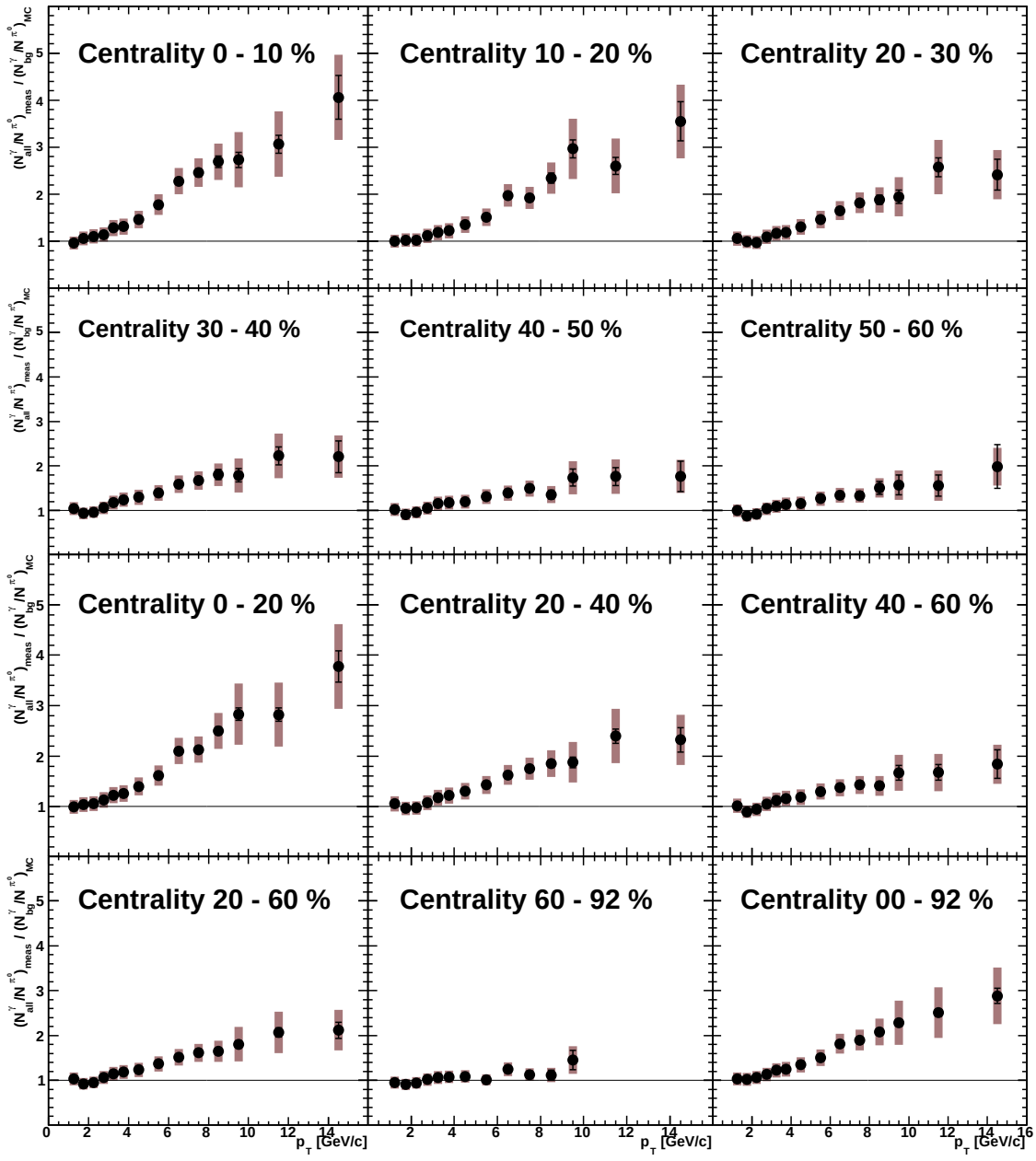

Figure 3.33: The number of inclusive photon to background photon ratio. In order to cancellation the some of systematical error, these ratio is normalized by yield of π^0. Bars show the statistical error, and boxes show the systematical error.

3.8.3 Direct Photon v_2 Extraction

Finally, we performed the v_2 of direct photon from inclusive photon, hadronic decay photon via Monte-Carlo simulation based on π^0 , and excess ratio of direct photon.

$$v_2^{\rm direct} = \frac{(N^{\rm inclusive}/N^{\rm bg})v_2^{\rm inclusive} - v_2^{\rm bg}}{(N^{\rm inclusive}/N^{\rm bg}) - 1}, \quad (3.74)$$

$$= \frac{R \cdot v_2^{\rm inclusive} - v_2^{\rm bg}}{(R-1)}. \quad (3.75)$$

Then, the statistical and systematical errors are propagated from each estimations,

$$\Delta v_2^{\rm direct} = \sqrt{\left(\frac{\partial v_2^{\rm direct}}{\partial v_2^{\rm inclusive}}\Delta v_2^{\rm inclusive}\right)^2 + \left(\frac{\partial v_2^{\rm direct}}{\partial v_2^{\rm bg}}\Delta v_2^{\rm bg}\right)^2 + \left(\frac{\partial v_2^{\rm direct}}{\partial R}\Delta R\right)^2}, \quad (3.76)$$

here, the measurement error of π^0 is used as hadronic decay photon error. Figure 3.34 shows the v_2 of inclusive photon, hadron decay photon, and direct photon in $\sqrt{s_{\rm NN}} = 200$ GeV at minimum bias Au + Au collisions up to $p_{\rm T} = 16.0$ GeV/c .

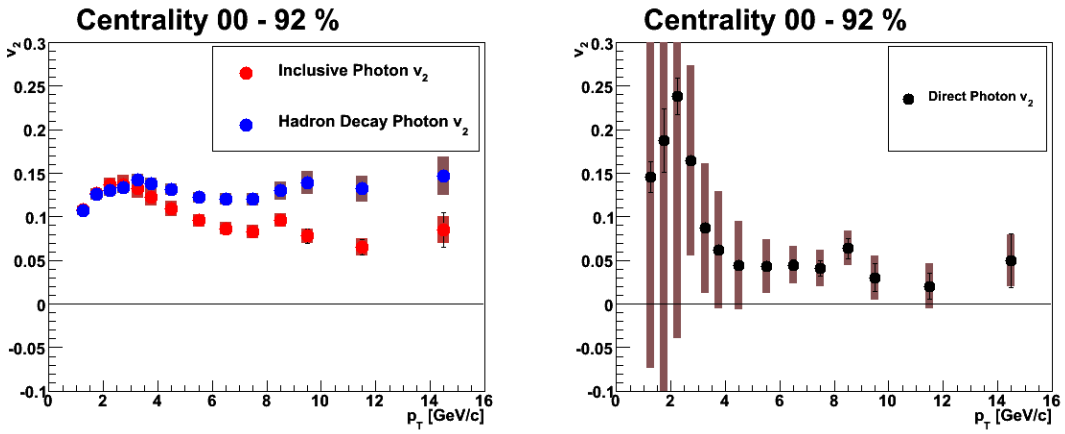

Figure 3.34: The v_2 of inclusive photon, hadron decay photon, and direct photon in $\sqrt{s_{\rm NN}} = 200$ GeV at minimum bias Au + Au collisions up to $p_{\rm T} = 16.0$ GeV/c. Reaction plane is determined by using RxNP. Boxes show the systematical error.

Although the error bars of direct photon in low-$p_{\rm T}$ are large due to excess ratio ~ 1, direct photon v_2 is extracted at $p_{\rm T} = 4 \sim 16$ GeV/c.

In the meantime, we have good method for low-$p_{\rm T}$ direct photon measurement in low $p_{\rm T}$ by using internal conversion to dilepton of thermal photon as described in Section 1.4.4. Excess ratio of direct photon via dilepton have better accuracy than real photon analysis especially $p_{\rm T}$ = 1 ∼3 GeV/c, the v_2 would be also improved as discuss in Section 5.3.

Chapter 4

Results

The measured v_2 of inclusive photon, neutral pion, and direct photon in $\sqrt{s_{\rm NN}} = 200$ GeV at Au+Au collisions (PHENIX Year-7 data set) are summarized in this chapter. Figure 4.1 and 4.2 show the inclusive photon v_2, Fig. 4.3 and 4.4 show the π^0 v_2, Fig. 4.5 and 4.6 show the direct photon v_2. The angle of reaction plane is determined by using BBC and RxNP, and measured v_2 respectively. According to a large statistics and good resolution of reaction plane, the $p_{\rm T}$ range is extended up to 16.0 GeV/c. The black bars show the statistical error and gray bands show the systematical error.

In the direct photon analysis, the statistical error and the systematical error are propagated from v_2 of inclusive photon, hadron decay photon, and their ratio.

- Figure 4.1 : Inclusive photon v_2 by using RxNP
- Figure 4.2 : Inclusive photon v_2 by using BBC
- Figure 4.3 : Neutral pion v_2 by using RxNP
- Figure 4.4 : Neutral pion v_2 by using BBC
- Figure 4.5 : Direct photon v_2 by using RxNP
- Figure 4.6 : Direct photon v_2 by using BBC

4.1 Inclusive Photon v_2 in $\sqrt{s_{\rm NN}}$ = 200 GeV Au+Au Collisions

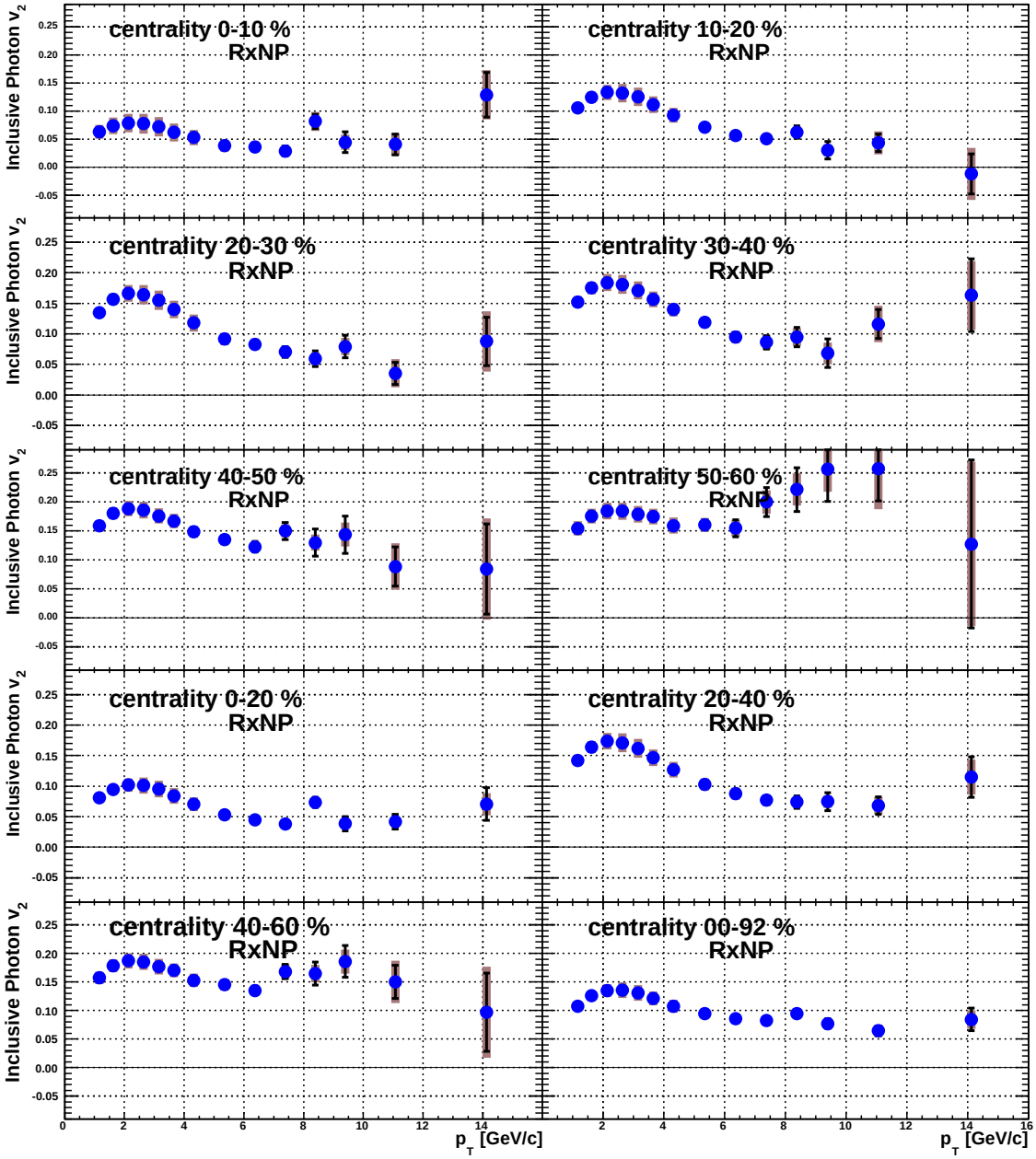

Figure 4.1: Inclusive photon v_2 by using RxNP as a function of $p_{\rm T}$ in $\sqrt{s_{\rm NN}}$ = 200 GeV Au+Au collisions at PHENIX Year-7.

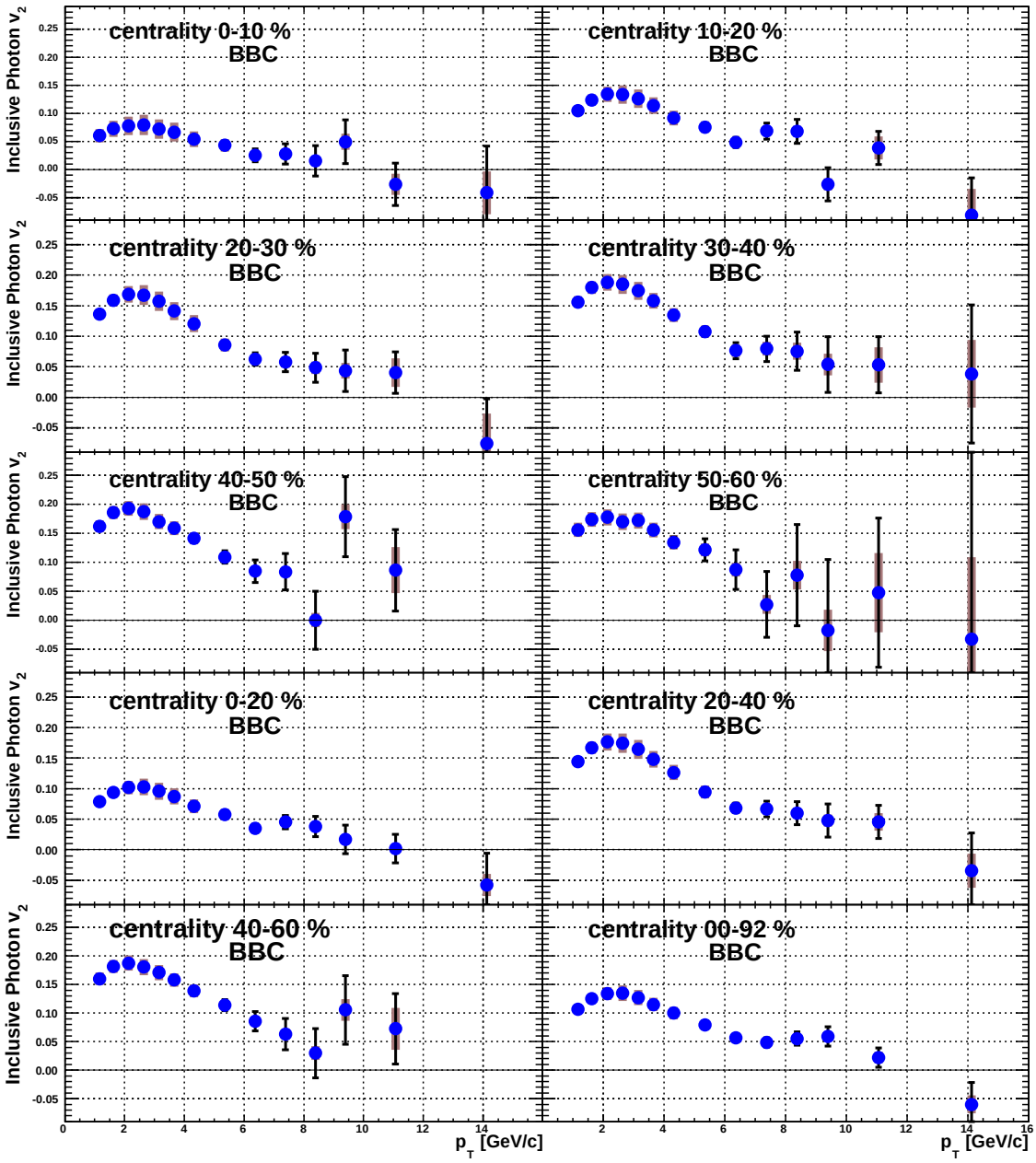

Figure 4.2: Inclusive photon v_2 by using BBC as a function of p_{T} in $\sqrt{s_{\mathrm{NN}}} = 200$ GeV Au+Au collisions at PHENIX Year-7.

4.2 Neutral Pion v_2 in $\sqrt{s_{\rm NN}}$ = 200 GeV Au+Au Collisions

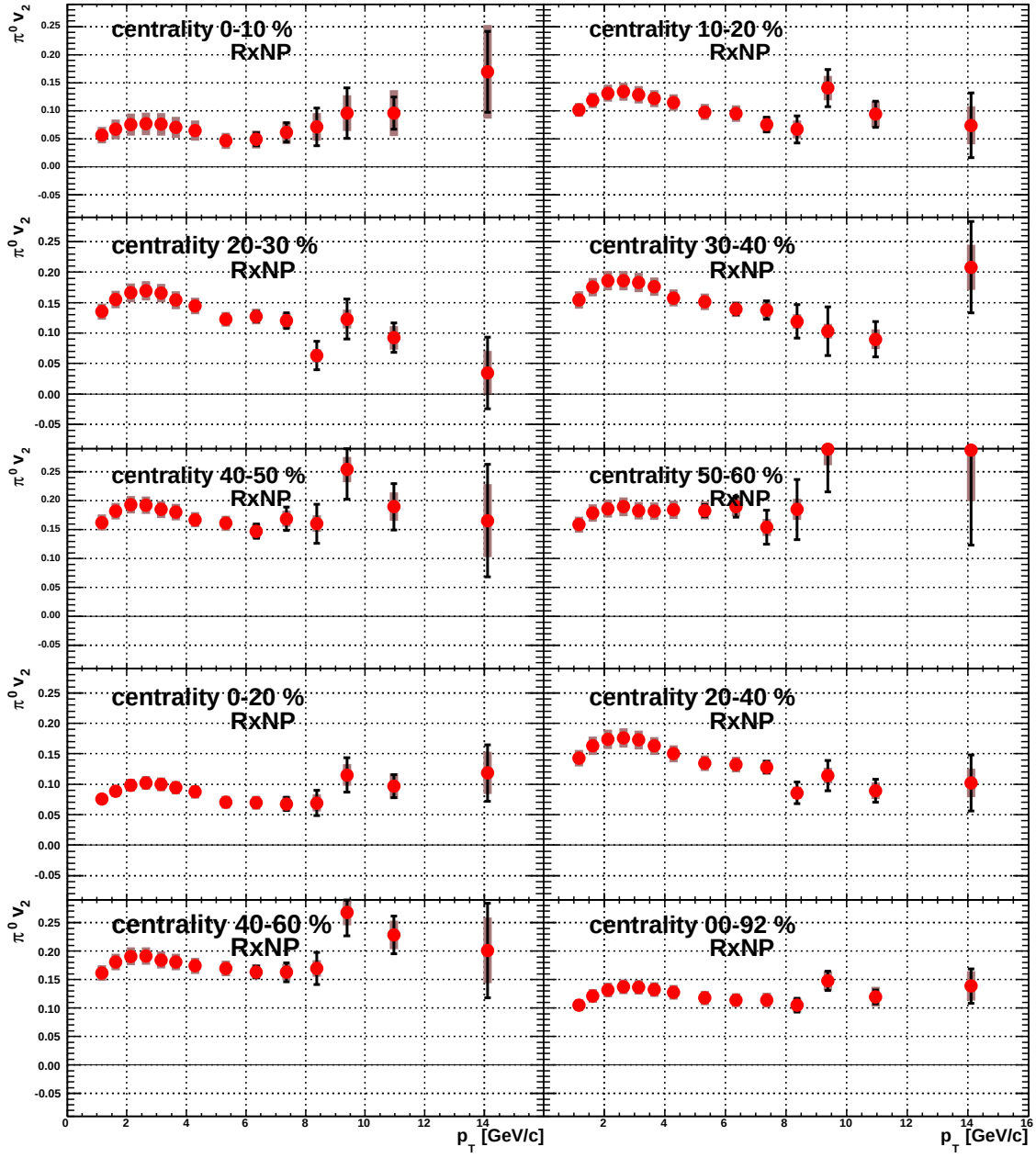

Figure 4.3: Neutral pion v_2 by using RxNP as a function of $p_{\rm T}$ in $\sqrt{s_{\rm NN}}$ = 200 GeV Au+Au collisions at PHENIX Year-7.

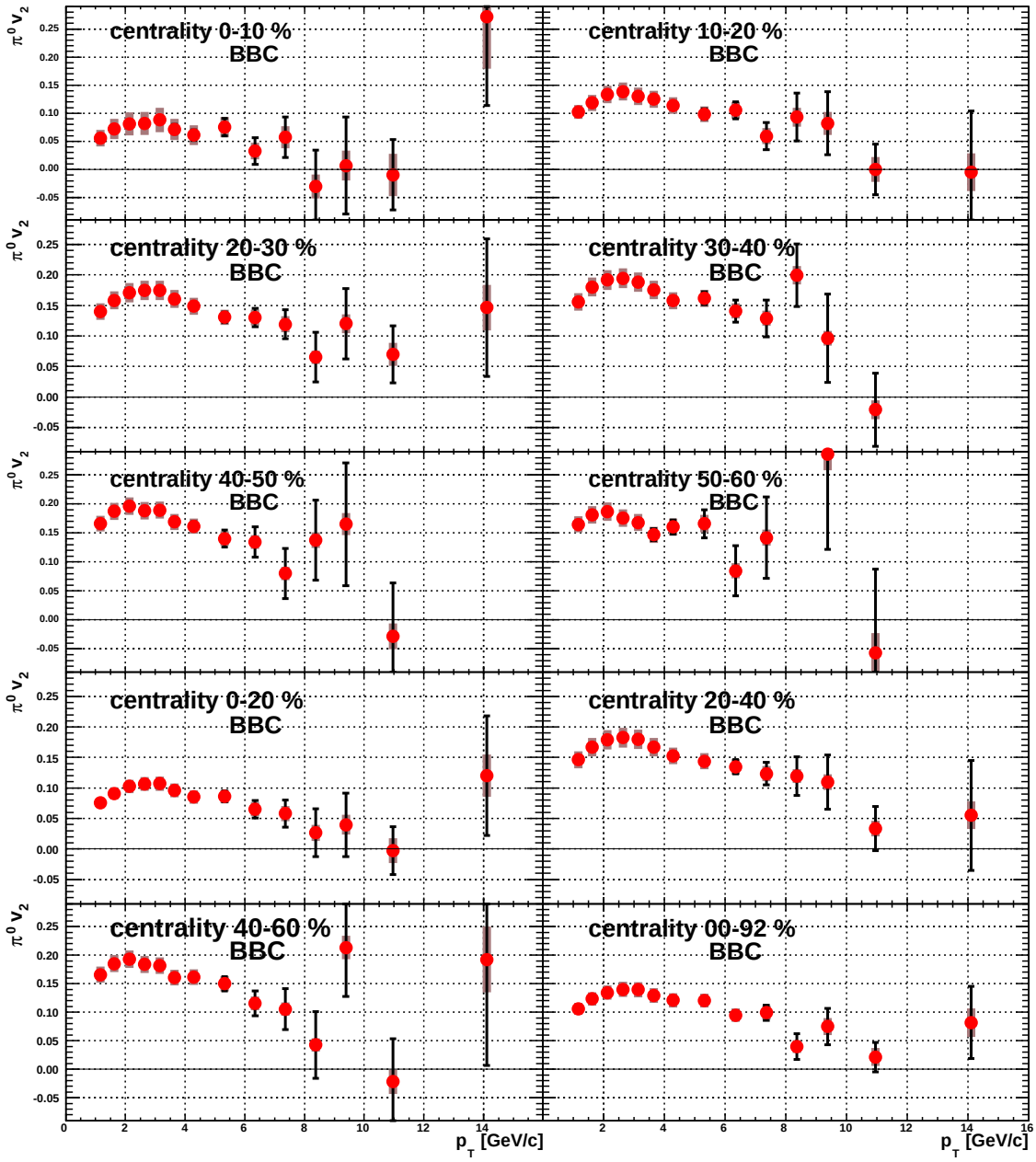

Figure 4.4: Neutral pion v_2 by using BBC as a function of p_{T} in $\sqrt{s_{\mathrm{NN}}}$ = 200 GeV Au+Au collisions at PHENIX Year-7.

4.3 Direct Photon v_2 in $\sqrt{s_{\rm NN}}$ = 200 GeV Au+Au Collisions

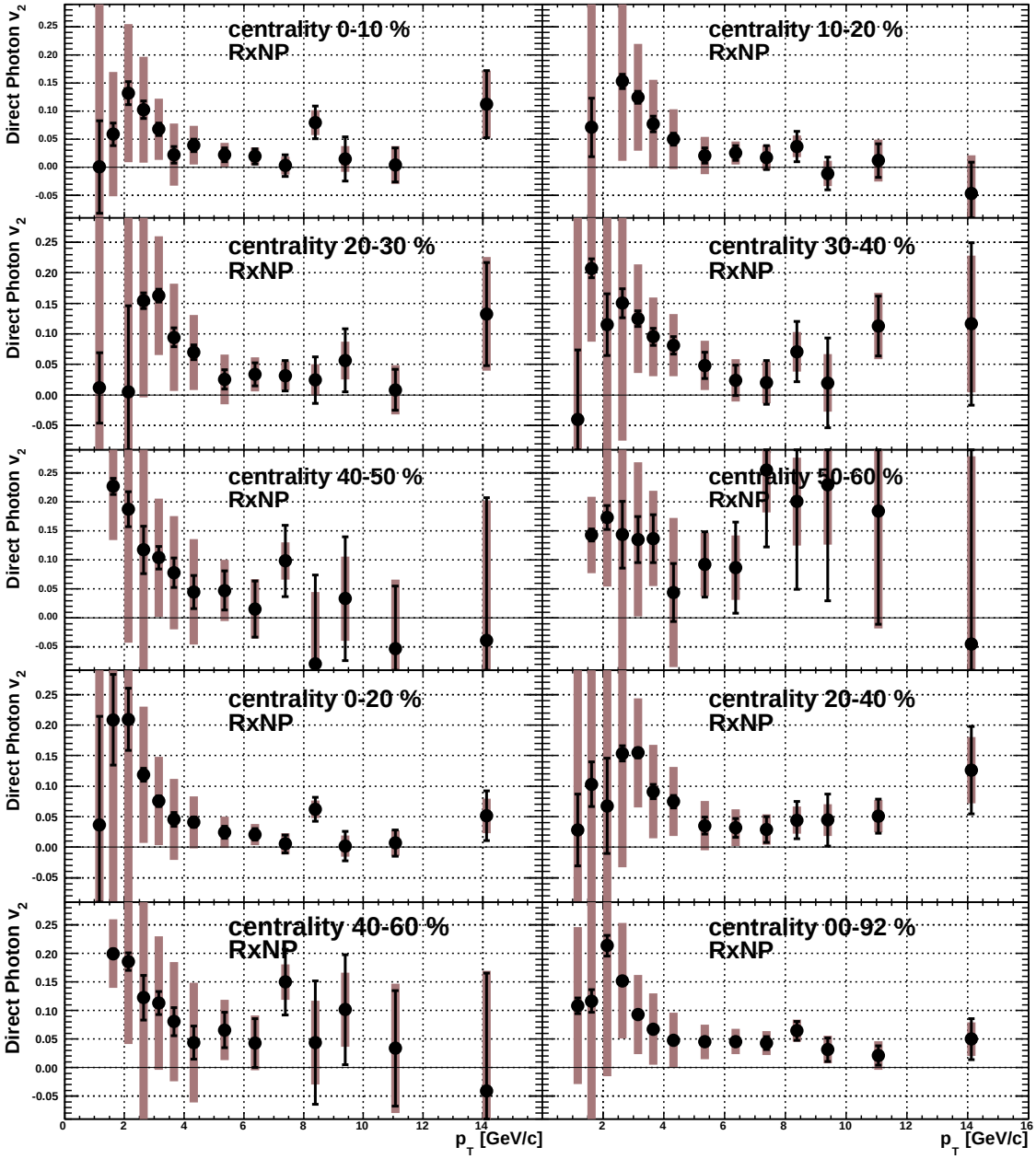

Figure 4.5: Direct photon v_2 by using RxNP as a function of $p_{\rm T}$ in $\sqrt{s_{\rm NN}}$ = 200 GeV Au+Au collisions at PHENIX Year-7.

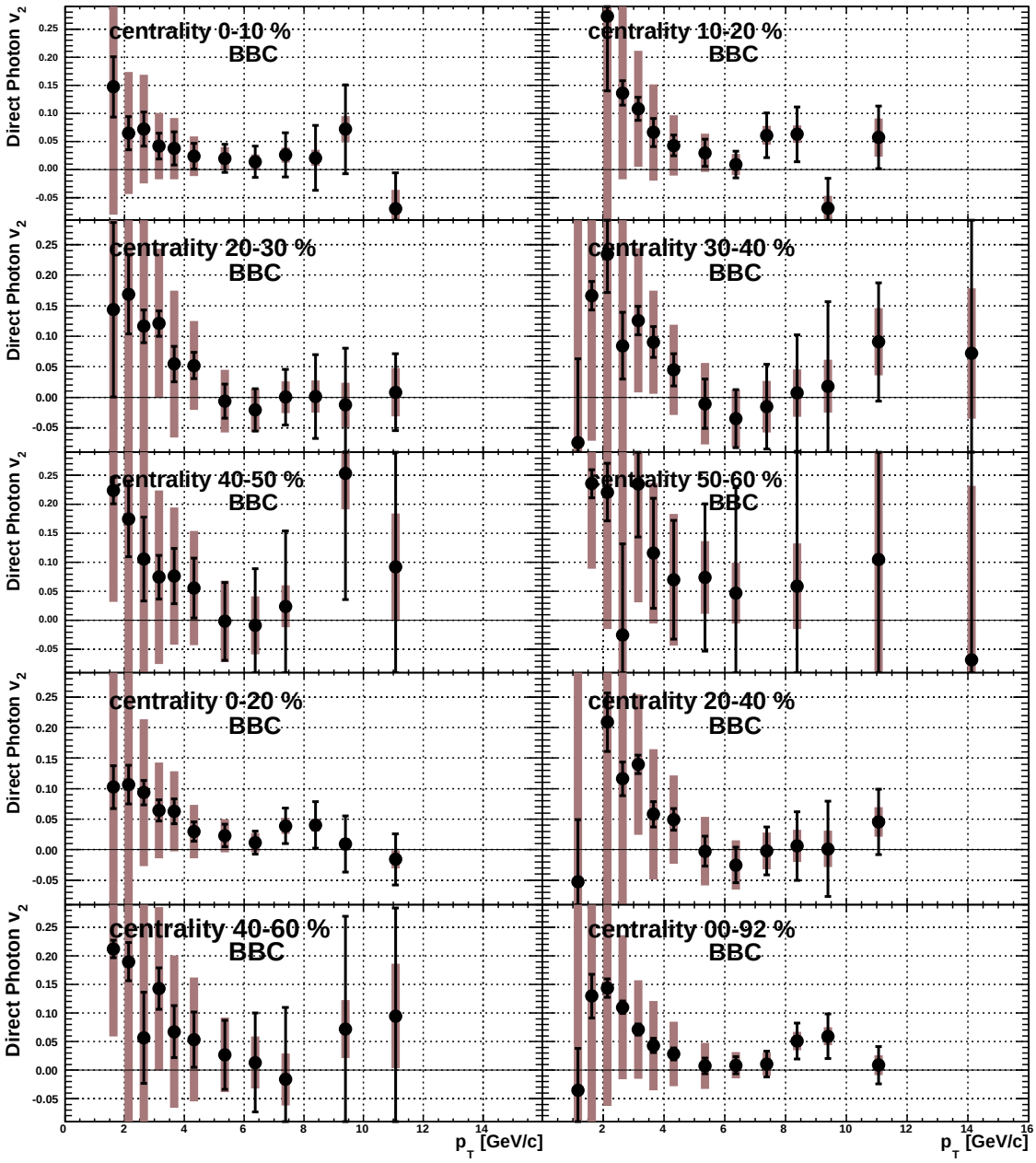

Figure 4.6: Direct photon v_2 by using BBC as a function of p_{T} in $\sqrt{s_{\mathrm{NN}}}$ = 200 GeV Au+Au collisions at PHENIX Year-7.

Chapter 5

Discussions

As shown in the previous chapter, we have obtained v_2 of neutral pion and that of direct photon up to $p_{\rm T} = 16$ GeV/c in $\sqrt{s_{\rm NN}} = 200$ GeV Au + Au collisions at PHENIX Year-7 data set. As described in Section 1.4.5, v_2 of direct photon provides information of the production processes of photon, while v_2 of π^0 at low-$p_{\rm T}$ shows the anisotropic collective flow of generated hadrons. From the results of photon and and charged hadron measurements, we discuss,

- comparison of measured v_2 between π^0 and charged hadrons (Section 5.1),
- origin of direct photon in high $p_{\rm T}$ (Section 5.2),
- origin of direct photon v_2 in low $p_{\rm T}$ (Section 5.3), and,
- secondary contribution of high-$p_{\rm T}$ direct photon (Section 5.4),

followed by summaries in Section 5.5.

5.1 π^0 v_2 Compared with Charged Hadrons

The measured v_2 of π^0 should be comparable to that of charged pion obtained totally different scheme of measurement. As a first of discussions, v_2 of π^0 compared with that of identified charged hadrons for consistency check in low-$p_{\rm T}$. Particle species of charged hadrons are identified by using their time-of-flight. The π^0 v_2 is also compared with the non-identified charged hadron v_2 in order to study the structure in high-$p_{\rm T}$.

5.1.1 The v_2 of π^0 Compared with $\pi^{\pm}$

Figure 5.1 shows the comparison plots for π^0, $\pi^{\pm}$, $K^{\pm}$, p and $\bar{p}$ [57]. Charged particles are measured in $\sqrt{s_{\rm NN}} = 200$ GeV Au + Au collisions with PHENIX Year-4 data set by using Time-of-Flight detector. The v_2 of π^0 shows a good agreement with charged hadrons below $p_{\rm T} = 3$ GeV/c within error bar. Since v_2 of charged hadrons is well described by a hydro-dynamical calculation [43], that of π^0 is also described by the same hydro-dynamical picture.

The parameter, $KE_{\rm T}$ is given by,

$$KE_{\rm T} = \sqrt{p_{\rm T}^2 + m_0^2} - m_0, \tag{5.1}$$

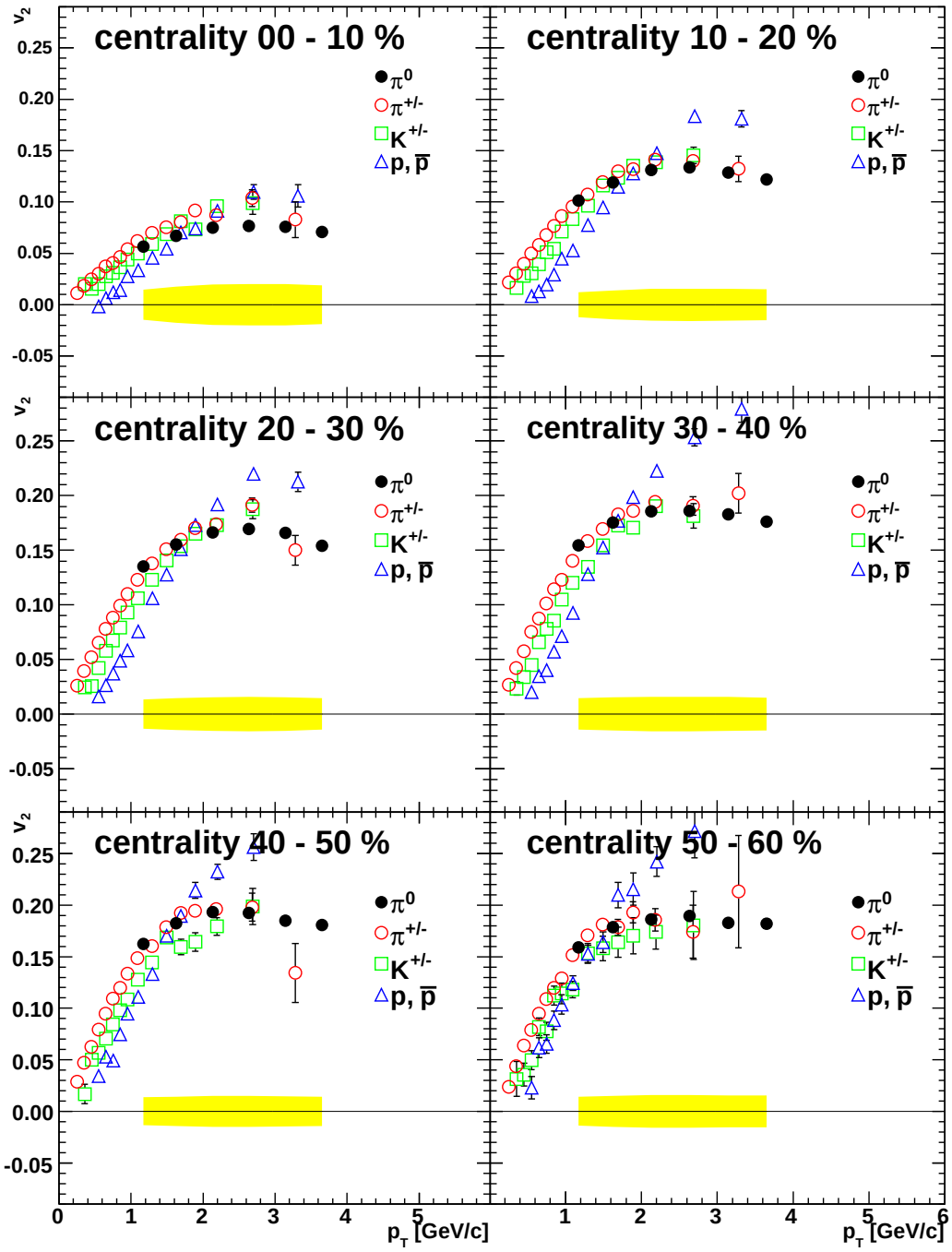

Figure 5.1: The measured v_2 of π^0 compared with $\pi^{\pm}$, $K^{\pm}$, p, and $\bar{p}$. The charged hadrons are measured by using Time-of-Flight detector in $\sqrt{s_{\rm NN}} = 200$ GeV Au+Au collisions [57]. The bands around $y = 0$ show the systematical error for v_2 of π^0.

where, m_0 denotes the invariant mass of each particle. Experimentally, the agreement of quark number scaled v_2 structure between charged hadrons in low-$p_{\rm T}$ is also observed in π^0. Figure 5.2 shows the quark number scaled v_2 of identified charged hadrons and π^0 as a function of quark number scaled $KE_{\rm T}$.

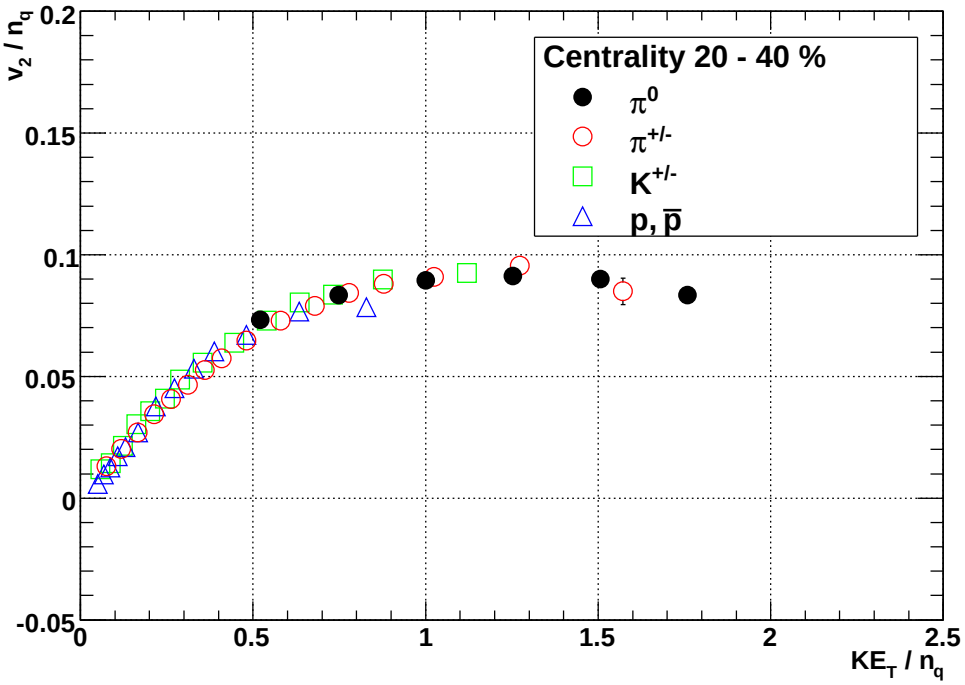

Figure 5.2: Scaled v_2 by the number of quark for identified charged hadrons and π^0 at centrality 20 to 40%. The n_q denotes the quark number of each hadron.

In general, low-p_{T} v_2 of charged hadrons is known to follow KE_{T} scaling together with quark number scaling [57], implying quark recombination mechanism for hadron production. Therefore this is considered to be one of the evidence of collective quark flow in the early stage of partonic medium (QGP) generated by the heavy-ion collisions.

5.1.2 π^0 v_2 in High-p_{T}

The capability of particle identification of π^0 in high-p_{T} is better than other hadrons, because of the superior signal-to-noise ratio (S/N) of invariant mass distribution of 2γ for π^0 at high-p_{T}. Furthermore, we can use higher statistics and the reaction plane with better resolution in PHENIX Year-7 which enables us to obtain v_2 of π^0 up to $p_{\mathrm{T}} = 16$ GeV/c.

When we do not need to know the particle species of hadrons, non-identified charged hadrons also allow us reliable discussions at high-p_{T} region. The yields of non-identified charged hadron are measured by matching selection between charged particle tracking and hit position, without particle identification. In the Fig. 5.3, v_2 of non-identified charged hadron is shown with π^0 at mid-central collisions. In high-p_{T} region above 6 GeV/c, the π^0 v_2 is consistent with the charged hadron v_2 indicating that charged hadrons are mostly pions in that region.

Figure 5.4 shows the invariant yield of $\pi^{\pm}$, π^0 and proton at $\sqrt{s_{\mathrm{NN}}} = 200$ GeV in mid-central Au + Au collisions (left figure). In the study for particle yield ratio of proton and pion, proton enhancement has been observed in Au + Au collisions (right figure) [59] compared with p + p collisions. The baryon enhancement is explained in [59] by a transverse radial flow or quark recombination, which disappears above 6 GeV/c.

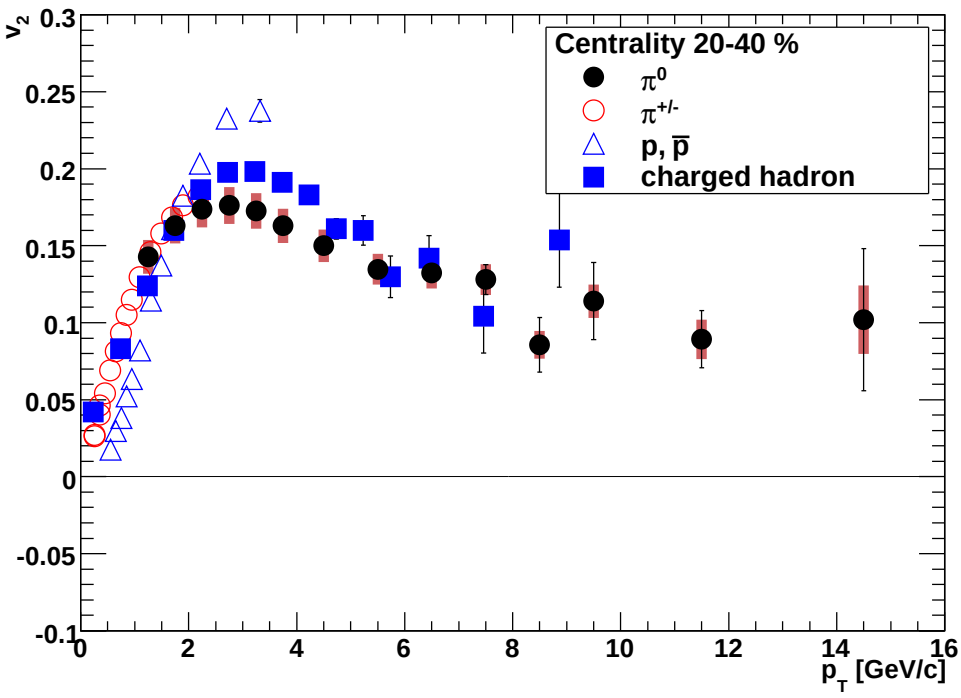

Figure 5.3: The v_2 of non-identified charged hadron with π^0 and $\pi^{\pm}$ are shown in mid-central Au + Au collisions. The band around $y = 0$ denotes the systematical error of π^0.

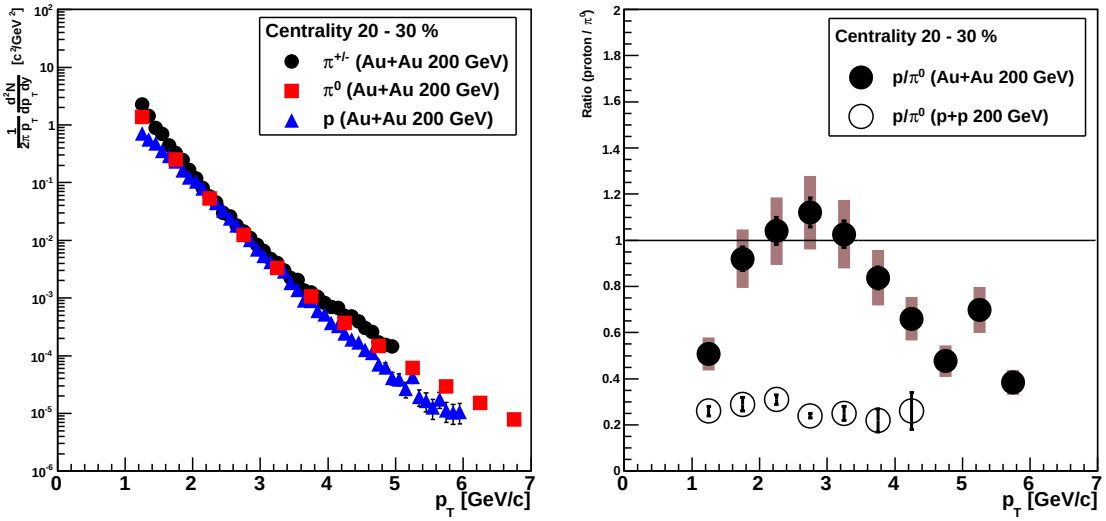

Figure 5.4: (Left) Measured invariant yields of charged pion, neutral pion, and proton at $\sqrt{s_{\rm NN}}$ = 200 GeV in mid-central Au + Au collisions [59] [28]. (Right) The proton to pion ratio for the study of baryon enhancement at Au + Au collisions. The ratio in p + p are also plotted as a reference.

The p/π ratios turn over at $p_{\rm T}$ = 2-3 GeV/c, and fall towards the ratio in p + p at $p_{\rm T}$ >6 GeV/c. This indicates a transition from soft to hard process at intermediate-$p_{\rm T}$, and this is also

shown in v_2 in Fig. 5.3, where v_2 of π^0 becomes same with that of charged hadrons at high-p_T while charged hadron v_2 is greater than π^0 at intermediate-p_T. Therefore, we concluded the baryon enhancement is disappeared at p_T >6 GeV/c.

5.2 High-p_T v_2 of Direct Photon

Figure 5.5 shows the v_2 of direct photon compared with π^0 v_2 at $\sqrt{s_{NN}} = 200$ GeV in mid-central Au + Au collisions up to $p_T = 16$ GeV/c. It is not easy to determine the low-p_T direct photon

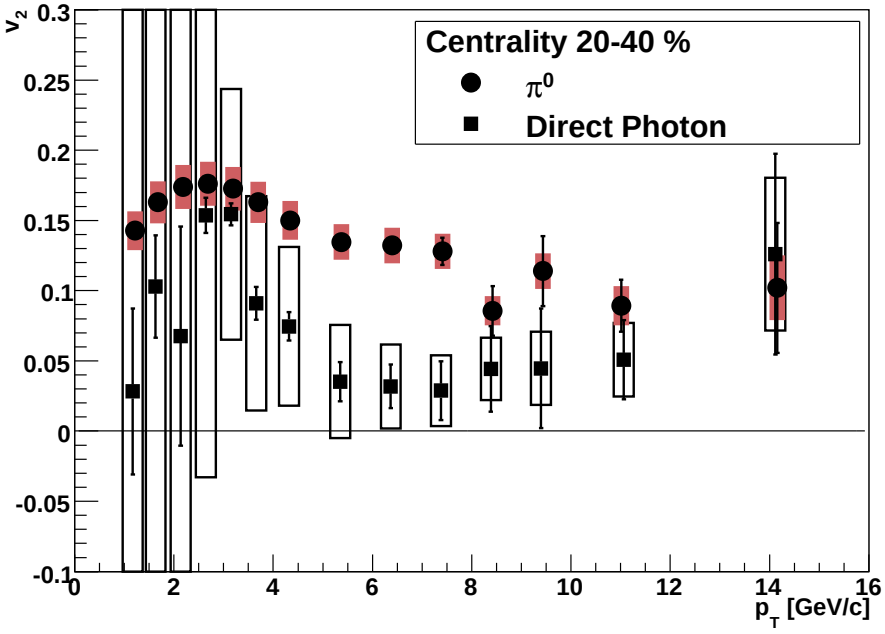

Figure 5.5: Measured v_2 of direct photon and π^0 as a function of p_T at $\sqrt{s_{NN}} = 200$ GeV in mid-central Au + Au collisions. The bars show statistical error and the boxes show the systematical error for each data point.

with small error bars due to the large hadron decay background and the worse detector response. On the other hand, since there is large suppression in high-p_T hadron yields at central Au+Au collisions, signal-to-background ratio (S/B) for photon yield improves at high-p_T, so that the measured v_2 also improves.

5.2.1 Direct Photon v_2 Compared with R_{AA}

The nuclear modification factor (R_{AA}) has been measured in PHENIX. The R_{AA} is given by invariant yields in unit rapidity and cross section in the p + p collisions as follows,

$$R_{AA} = \frac{d^2N_{AA}/dp_T d\eta}{T_{AA} d^2\sigma_{NN}/dp_T d\eta}, \tag{5.2}$$

where, T_{AA} denotes Glauber scaling factor, and η is pseudo-rapidity. In the early results of RHIC experiment, we observed the strong suppression of high-p_T hadron yields in the central heavy

ion collisions compared with p+p collisions when using the scaling law of the number of binary nucleon-nucleon collisions [47]. Figure 5.6 shows the measured $R_{\rm AA}$ of direct photon, π^0 , η, ω, J/ψ, and ϕ at central collision. A suppression of high-$p_{\rm T}$ hadrons is observed clearly by the

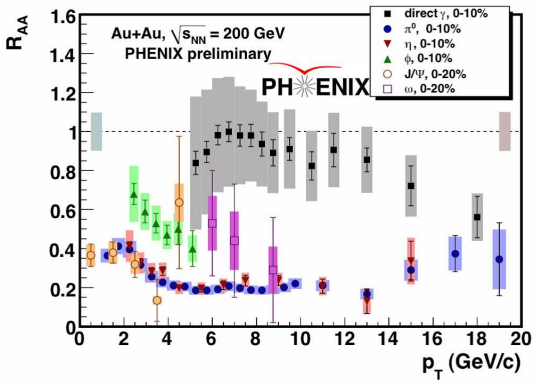

Figure 5.6: The $R_{\rm AA}$ of direct photon, π^0 , η, ω, J/ψ, and ϕ [63][52][53][67][54][68] at $\sqrt{s_{\rm NN}}$ = 200 GeV in central Au + Au collisions.

measurement of $R_{\rm AA}$, it is resulting from a characteristic energy loss of hard-scattered partons passing through the high density matter [28]. On the contrary, non-suppression of high-$p_{\rm T}$ direct photon yields are observed in $\sqrt{s_{\rm NN}}$ = 200 GeV Au + Au collisions [29]. It is indicated that the photon does not interact strongly even in the extreme hot and dense medium, and this results confirm the advantage of direct photon analysis as a penetrating probe.

In addition, we got a strong statement about the main contribution of high-$p_{\rm T}$ direct photon from results of direct photon $R_{\rm AA}$. As we can see in the figure of Fig. 5.6, $R_{\rm AA}$ of direct photon is equal to 1 (even error bar is large), so the extreme hot and dense medium generated by heavy-ion collisions does not influence entirely on the photon emission. This suggests that the initial hard-scattering of partons (prompt photon) is the dominant source of direct photon in high-$p_{\rm T}$, and medium effects such as jet-fragmentation, and jet-photon conversion (Section 1.4.1) are not effective even Au+Au collisions.

Figure 5.7 shows the measured v_2 of direct photon in centrality 0 to 20% and 20 to 40%. Solid lines show the mean value of v_2 above $p_{\rm T}$ = 6 GeV/c, and dashed lines and dashed-dotted lines show the statistical and systematical error range respectively. According to Fig. 5.7, direct photon v_2 in central is consistent with zero in high $p_{\rm T}$.

Since the photons from initial hard-scattering emit to all azimuth, the v_2 of prompt photon is expected to be equal to zero. Therefore, this confirms that the direct photon is mainly composed of prompt photon in this $p_{\rm T}$ region, and it is consistent with the $R_{\rm AA}$ results.

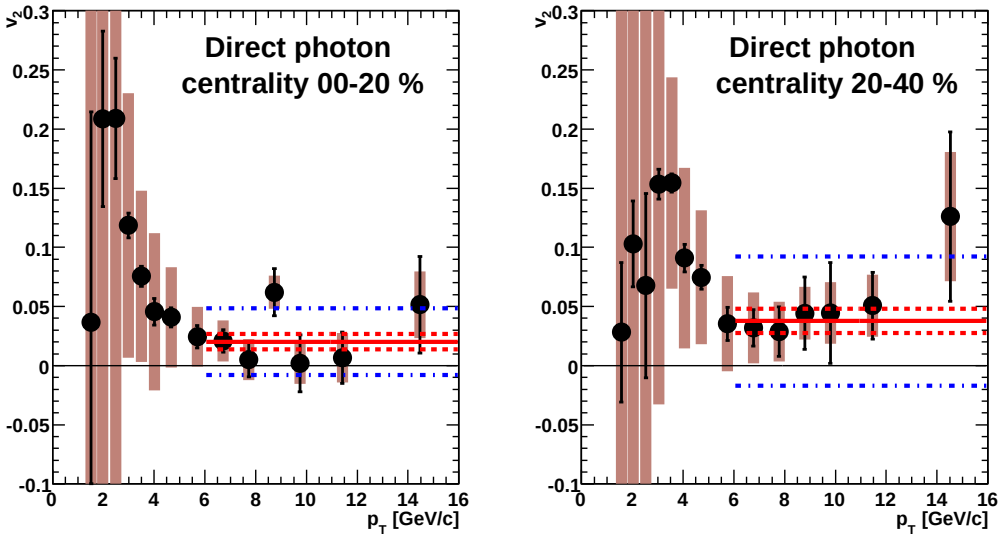

Figure 5.7: Measured v_2 of direct photon in centrality 0 to 20% and 20 to 40%. Solid lines show the mean value of v_2 above p_T = 6 GeV/c, dashed lines show the error band of statistical and dashed-dotted lines show the range of systematical uncertainty.

5.3 Low-p_T v_2 of Direct Photon

Thermal radiations from the QGP and/or hadron gas are expected by pQCD calculation to be observed at p_T = 2-3 GeV/c [40]. However, it is not easy to measure the direct photon in this p_T region because of large hadron decay contamination, and the worse detector resolution. In the meantime as described in Section 1.4.4, good direct photon spectra at low-p_T has been observed via internal conversion of dilepton in PHENIX experiment [45].

In general, any sources of photons also generate the virtual photon which convert to low mass e^+e^- pairs. Since the difference of Feynman diagram for real and virtual photon production is only internal conversion part, it is trivial to relate the production rates of real and virtual photon. Furthermore, when we choose the low mass region compared with p_T , the ratio of direct and inclusive photon turns out to be the ratio of real and virtual photon as described in Section 1.4.4,

$$r \equiv \frac{N_\gamma^{\rm direct}}{N_\gamma^{\rm inclusive}} = \frac{N_{\gamma^*}^{\rm direct}}{N_{\gamma^*}^{\rm inclusive}}, \tag{5.3}$$

Figure 1.18 shows the direct photon to inclusive photon ratio (r) obtained from electron pair analysis in p + p and Au + Au collisions. The ratio r is able to adopt to excess ratio R of direct photon (Section 3.8.2) by Eq. 5.3, so that is also able to apply for the v_2 analysis of direct

photon. The ratio r and excess ratio R of direct photon is related as,

$$\begin{aligned} R &\equiv \frac{N_\gamma^{\rm inclusive}}{N_\gamma^{\rm background}}, \\ &= \frac{N_\gamma^{\rm inclusive}}{N_\gamma^{\rm inclusive} - N_\gamma^{\rm direct}}, \\ &= \frac{1}{1 - N_\gamma^{\rm direct}/N_\gamma^{\rm inclusive}}, \\ &= \frac{1}{1 - N_{\gamma^*}^{\rm direct}/N_{\gamma^*}^{\rm inclusive}} = \frac{1}{1-r}. \end{aligned} \tag{5.4}$$

Figure 5.8 shows the excess ratios of direct photon determined by real photon and internal conversion of virtual photon. The ratio r shows a good resolution compared with real photon in low-$p_{\rm T}$ since virtual photon analysis is able to avoid the large background contamination from π^0 decay. Therefore, the v_2 of direct photon is expected to improve in lower $p_{\rm T}$ region.

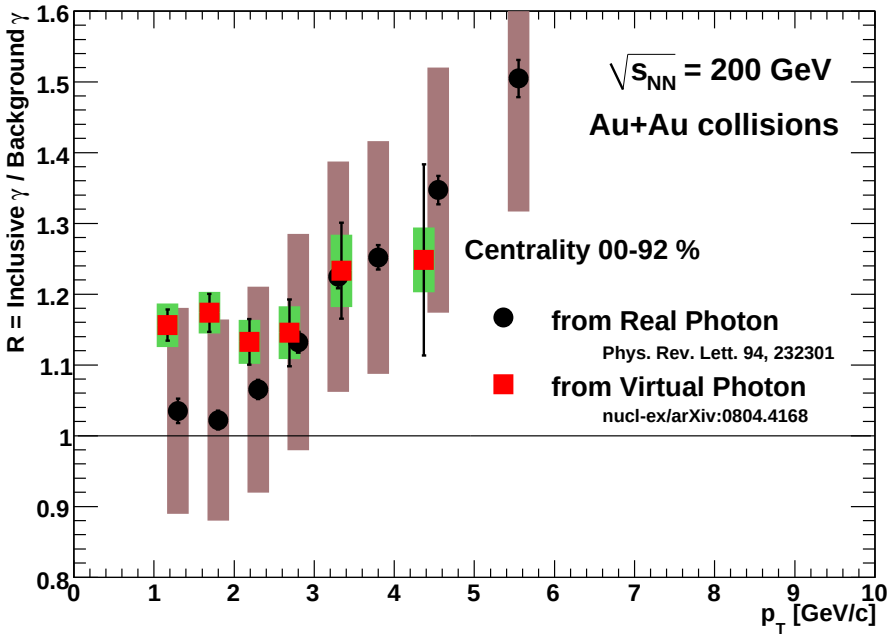

Figure 5.8: Excess ratios of direct photon are shown determined from real [29] and virtual [45] photon analysis, respectively. Bars shows the statistical error, and colored boxes show the systematical error for each data point.

Figure 5.9 shows the direct photon v_2 estimated from v_2 of inclusive photon, hadronic decay photon, and the ratio r via e^+e^- pair analysis in [45]. Because of better resolution for the excess ratio of direct photon, v_2 of direct photon improves significantly below $p_{\rm T} = 3$ GeV/c compared with the real photon analysis. In Fig. 5.10 (left), the measured direct photon v_2 is compared with charged hadron v_2. The results is again consistent with charged hadron v_2 within systematic error bar. And in Fig. 5.10 (right), direct photon is compared with quark number scaled v_2 in order to study the photon resulting from thermal-QGP. If we consider the direct photon is

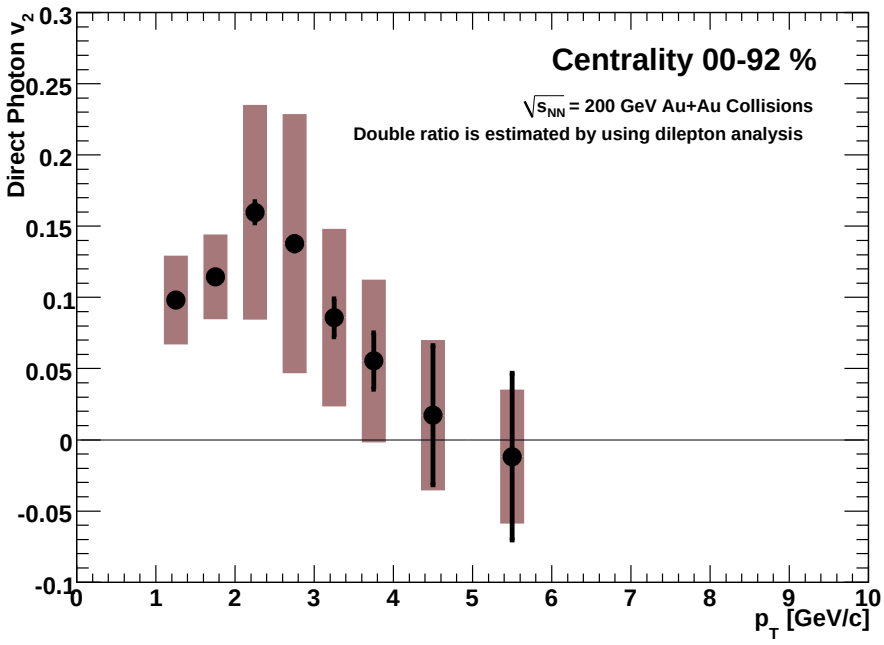

Figure 5.9: Measured direct photon v_2 from inclusive photon, hadronic decay photon, and the direct photon to inclusive photon ratio via internal converted electron pair analysis [45] at $\sqrt{s_{\rm NN}}$ = 200 GeV in minimum bias Au + Au collisions.

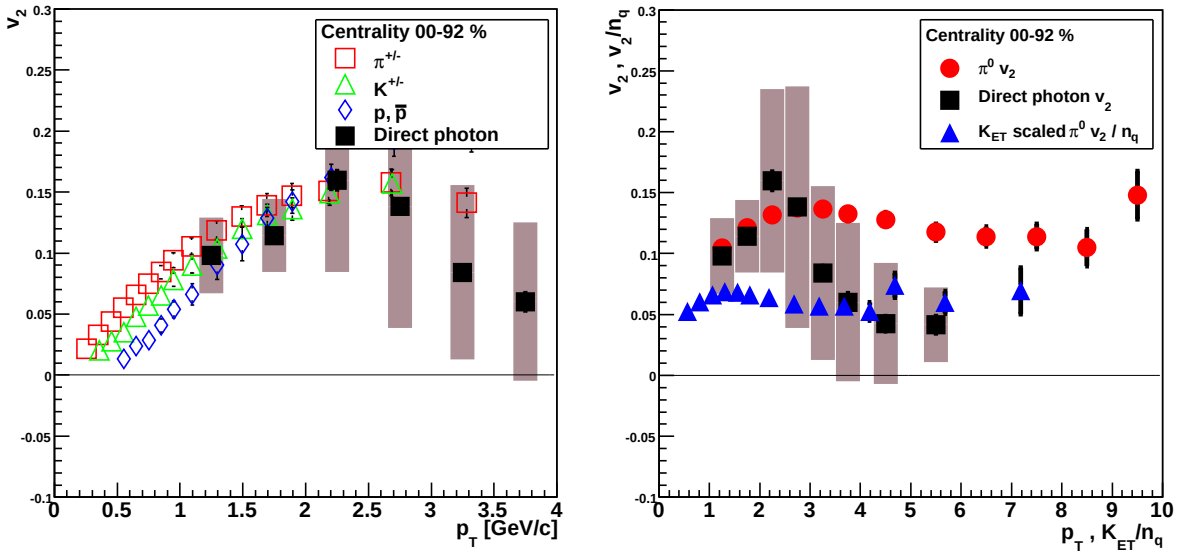

Figure 5.10: (Left) The measured v_2 of direct photon, $\pi^{\pm}$, $K^{\pm}$, p and $\bar{p}$. Direct photon result is consistent with charged hadron at low-$p_{\rm T}$ within statistical/systematical error bar. (Right) Direct photon v_2 is compared with $KE_{\rm T}$ scaled π^0. If all contamination of direct photon produced from thermalized QGP, direct photon would emitted from thermalized partons in QGP, so that the v_2 would be smaller than quark collective flow.

consisted of thermal photon from QGP, v_2 of direct photon would be smaller than the collective flow of quarks in low-p_{T}. In case of KE_{T} scaled v_2 of hadrons reflects the collective flow of quarks exactly, v_2 of thermal photon from QGP is also expected to depend on it. Figure 5.10 (left) shows the KE_{T} scaled π^0 v_2 with direct photon v_2.

As described in Section 1.4.4, the temperature of thermal photon ($T \approx 221$ MeV) estimated from direct photon yield in low-p_{T} is higher than chemical equilibrium temperature ($T_{\mathrm{ch}} \approx 177$ MeV). This statement imply for the most of low-p_{T} direct photons are generated in much earlier stage of the collisions than that of hadronic chemical equilibrium. Therefore it is naively expected that those direct photons with $T \approx 221$ MeV are emitted from the QGP phase. It is very interesting that the v_2 of direct photon in the $p_{\mathrm{T}} = 2$-3 GeV/c is similar or slightly larger than that of pions. This may imply the contribution as emission source from late hadron gas to thermal photon yield is not negligible in Au + Au collisions.

5.4 Secondary Contribution of Direct Photon

As described at Section 1.4 and 5.2, most of direct photons in high p_{T} are expected to be produced in initial hard-scattering of partons, called prompt photon. The v_2 of direct photon is well described with $v_2 = 0$ at $p_{\mathrm{T}} > 6$ GeV/c, it indicates the dominant source of direct photon is in fact the prompt photon, which should have zero v_2. This is also consistent with independent measurement such as non-suppressed direct photon which is confirmed by R_{AA} results of direct photon and π^0.

It is one of the greatest observation of prompt photon at high energy heavy-ion collision experiments, however systematical error of direct photon is significantly large, and the following discussion may not be applicable if we take the systematical error seriously. Nevertheless, it is important to extend the discussion about secondary contribution in the direct photon yield.

5.4.1 Average v_2 of High-p_{T} Direct Photon

The centrality dependence of direct photon v_2 represents as a function of the number of participating nucleons, $\langle N_{\mathrm{part}} \rangle$, as shown in Fig. 5.11. The v_2 of π^0 and direct photon are averaged above $p_{\mathrm{T}} = 6$ GeV/c to obtain less statistical error. The number of participating nucleons has

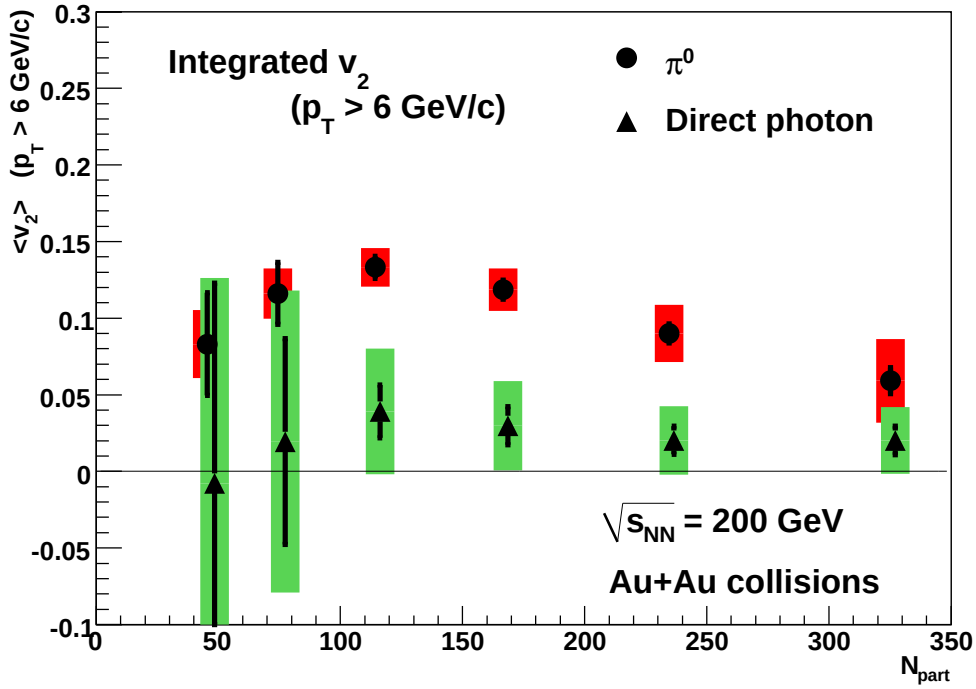

Figure 5.11: Average v_2 of direct photon and π^0 above $p_{\mathrm{T}} = 6$ GeV/c as a function of the number of participating nucleons. The bars show the statistical error, and colored boxes show the systematical error.

been determined by Glauber calculation as a function of centrality. The results are listed below for N_{part}, N_{coll}, and impact parameter b for $\sqrt{s_{\mathrm{NN}}} = 200$ GeV Au + Au collisions [66].

In peripheral collisions, the v_2 with respect to the azimuthal angle of reaction plane deter-

Table 5.1: Results of $\sqrt{s_{\rm NN}} = 200$ GeV Au + Au Glauber calculations [66].

Centrality	$\langle N_{\rm part} \rangle$	sys. error	$\langle N_{\rm coll} \rangle$	sys. error	$\langle b \rangle$ [fm]	sys. error
0-10 %	325.2	3.3	955.4	93.6	3.2	0.2
10-20 %	234.6	4.7	602.6	59.3	5.7	0.3
20-30 %	166.6	5.4	373.8	39.6	7.4	0.3
30-40 %	114.2	4.4	219.8	22.6	8.7	0.4
40-50 %	74.4	3.8	120.3	13.7	9.9	0.4
50-60 %	45.5	3.3	61.0	9.9	11.0	0.4
0-92 %	109.1	4.1	257.8	25.4	9.5	0.4

mined by BBC is used for the following discussions. From the results of average v_2 for π^0 and direct photon, we obtain that,

- photon v_2 is smaller than hadron v_2,
- v_2 of direct photon has a small positive value,
- non centrality dependence of direct photon is observed compared with hadron

We discuss about secondary contribution of direct photon yield by using the results on Fig. 5.11 in the following section.

5.4.2 Ratio of High-$p_{\rm T}$ Direct Photon

In p + p collisions, prompt and jet-fragmentation are considerable as production sources of high-$p_{\rm T}$ direct photon. The fraction of direct photon contribution is determined by pQCD calculation as shown in Fig. 5.12. The production rate of the jet-fragmentation photon is smaller than that of the prompt photon, but the contribution of jet-fragmentation is not negligible, and expected to be $n^{\rm fragment}/n^{\rm prompt} \approx 0.35/0.65$ above $p_{\rm T} = 8$ GeV/c.

Now, we adopt the following assumptions for discussion about prompt to jet-fragmentation ratio in Au+Au collisions,

- prompt photons obey the scaling low of binary number collisions exactly,
- all of high-$p_{\rm T}$ π^0 are produced by jet-fragmentation,
- the ratio of photon and π^0 produced by jet-fragmentation is same between p + p and Au+Au.

Under these assumptions, $R_{\rm AA}$ of jet-fragmentation photon corresponds to that of π^0 in Au+Au. Since the jet-fragmentation photons are defined as emission photon from fragmentation of hard-scattered parton, yields of jet-fragmentation photons are also suppressed by jet-quenching effect with π^0 in Au+Au.

Then we obtain the following relations,

$$R_{\rm AA}^{\rm prompt} = \frac{N^{\rm prompt}}{N_{\rm b} \cdot n^{\rm prompt}} = 1, \tag{5.5}$$

$$R_{\rm AA}^{\rm fragment} = \frac{N^{\rm fragment}}{N_{\rm b} \cdot n^{\rm fragment}} = R_{\rm AA}^{\pi^0}, \tag{5.6}$$

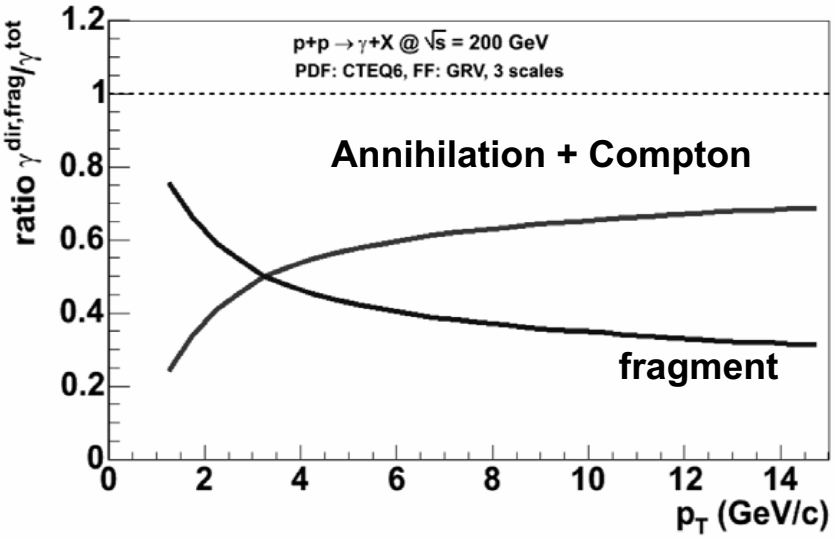

Figure 5.12: Fraction of jet-fragmentation photon (denotes fragment) and prompt photon (denotes Annihilation+Compton) in $p + p \rightarrow \gamma + X$ process at $\sqrt{s} = 200$ GeV predicted by pQCD calculation.

where, n^X and N^X denote the yields in a process X at p + p and Au + Au collisions respectively, and $N_{\rm b}$ is the scale factor of number of binary collisions. The $R_{\rm AA}$ of direct photon and π^0 are estimated experimentally, as shown in Fig. 5.13. Yield of π^0 are suppressed by jet-quenching at central collisions while non-suppression is observed in yield of direct photon. In the meantime, jet-fragmentation photon should be suppressed with π^0 in Au+Au collisions by jet-quenching effect. Therefore, we need to include an additional production source of direct photon caused by extreme hot and dense medium effect for enhance source of the direct photon yield. The number of total direct photon in Au+Au collisions is described as,

$$\begin{aligned} N^{\rm direct} &= N^{\rm prompt} + N^{\rm fragment} + N^{\rm add.}, \\ &= N_{\rm b} \cdot n^{\rm prompt} + N_{\rm b} \cdot n^{\rm fragment} \cdot R_{\rm AA}^{\pi^0} + N^{\rm add.}, \\ &= N_{\rm b} \cdot n^{\rm prompt}(1 + a \cdot R_{\rm AA}^{\pi^0} + b), \end{aligned} \tag{5.7}$$

where, a is defined as fraction of fragmentation and prompt in p + p ($a = n^{\rm fragment}/n^{\rm prompt}$), and b is defined as a rate of photons from additional source ($b = N^{\rm add.}/(n^{\rm prompt} \cdot N_{\rm b})$). The $R_{\rm AA}$ of direct photon is described by using parameter a, b, and $R_{\rm AA}^{\rm fragment}$ as,

$$\begin{aligned} R_{\rm AA}^{\rm direct} &= \frac{N^{\rm direct}}{N_{\rm b} \cdot n^{\rm direct}}, \\ &= \frac{N_{\rm b} \cdot n^{\rm prompt}(1 + a \cdot R_{\rm AA}^{\pi^0} + b)}{N_{\rm b} \cdot n^{\rm prompt} \cdot (1 + a)}, \\ &\quad (\because n^{\rm direct} = n^{\rm prompt} + n^{\rm fragment} = n^{\rm prompt}(1 + a)) \\ &= \frac{1 + a \cdot R_{\rm AA}^{\pi^0} + b}{1 + a}. \end{aligned} \tag{5.8}$$

Therefore, the fraction b of photons from additional source is calculated from $R_{\rm AA}^{\rm direct}$, $R_{\rm AA}^{\pi^0}$, and a,

$$b = (1+a)R_{\rm AA}^{\rm direct} - aR_{\rm AA}^{\pi^0} - 1. \tag{5.9}$$

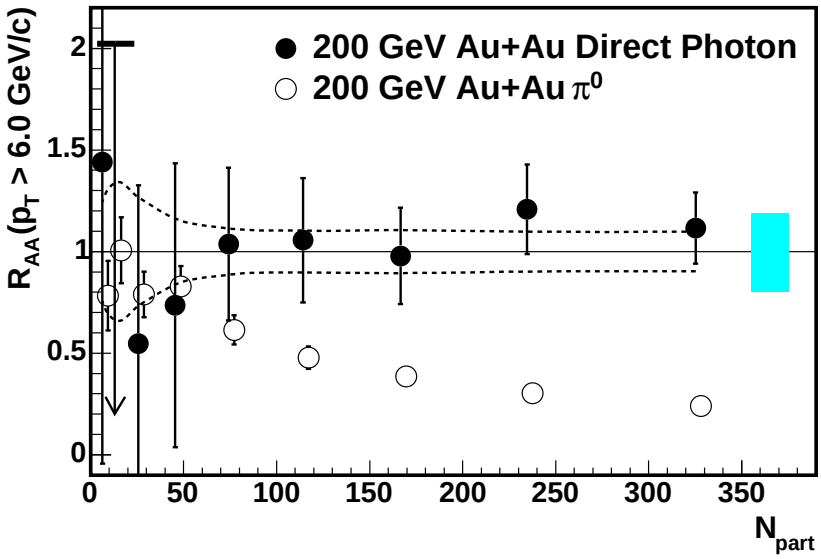

Figure 5.13: Nuclear modification factor ($R_{\rm AA}$) of direct photon and π^0 as a function of number of participants ($N_{\rm part}$) in $\sqrt{s_{\rm NN}} = 200$ GeV collisions [29]. The measured $R_{\rm AA}$ is averaged above 6 GeV/c.

From the experimental results of $R_{\rm AA}$ and parameter $a = n^{\rm fragment}/n^{\rm prompt} \approx 0.35/0.65$ obtained from pQCD calculation, we calculated parameter b as shown in Fig. 5.14. From the 1 polynomial fitting result, the ratio of high-$p_{\rm T}$ direct photon in central collisions is given by,

$$\begin{aligned} N^{\rm prompt} : N^{\rm fragment} : N^{\rm add.} &= n^{\rm prompt} : R_{\rm AA}^{\rm fragment} \cdot n^{\rm fragment} : \frac{N^{\rm add.}}{N_{\rm b}}, & (5.10)\\ &= 1 : R_{\rm AA}^{\rm fragment} \cdot \frac{n^{\rm fragment}}{n^{\rm prompt}} : b, & (5.11)\\ &\approx 1.0 : 0.13(\pm 0.01) : 0.5(\pm 0.17), & (5.12) \end{aligned}$$

here, $a \approx 0.54$, and $R_{\rm AA}^{\rm fragment} = R_{\rm AA}^{\pi^0} \approx 0.24 \pm 0.02$ are used in this calculation. It indicates the existence of another photon production process ($N^{\rm add.}$) in Au+Au collisions with about half amount of prompt photon.

5.4.3 Production Sources of High-$p_{\rm T}$ Direct Photon

Finally, we calculate the v_2 of additional source in high-$p_{\rm T}$ direct photon. Basically, same assumptions to previous section is also applied for the following discussion. Direct photon v_2 is

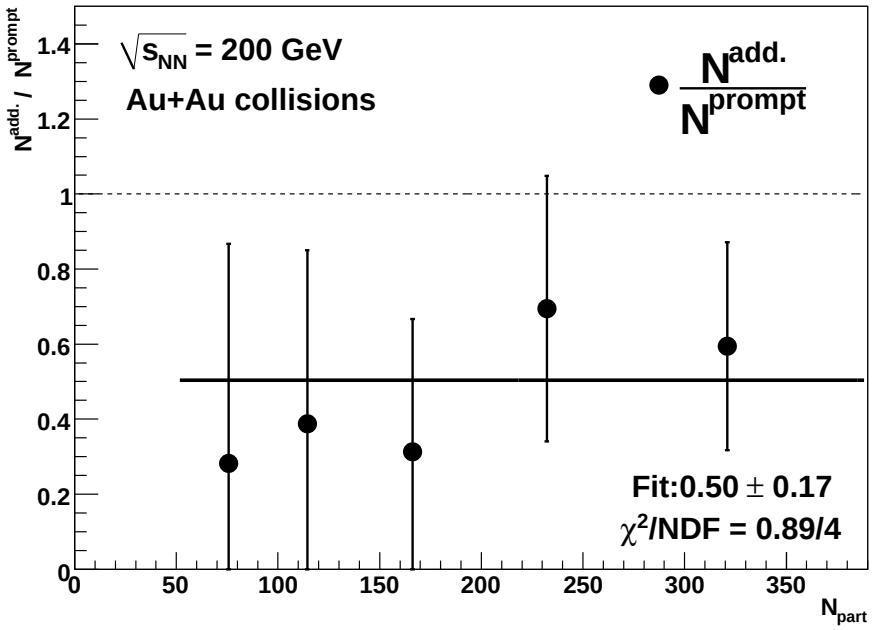

Figure 5.14: Fraction of high-$p_{\rm T}$ photon from production source except the prompt and jet-fragmentation estimated by measured $R_{\rm AA}$ as a function of $N_{\rm part}$.

described using v_2 and yield of each production source as,

$$v_2^{\rm direct} = \frac{N^{\rm prompt}\cdot v_2^{\rm prompt} + N^{\rm fragment}\cdot v_2^{\rm fragment} + N^{\rm add.}\cdot v_2^{\rm add.}}{N^{\rm direct}}, \tag{5.13}$$

$$= \frac{N_{\rm b}\cdot n^{\rm fragment}\cdot R_{\rm AA}^{\rm fragment}\cdot v_2^{\rm fragment} + N_{\rm b}\cdot n^{\rm prompt}\cdot b\cdot v_2^{\rm add.}}{N_{\rm b}\cdot R_{\rm AA}^{\rm direct}\cdot n^{\rm direct}}, \tag{5.14}$$

$$= \frac{n^{\rm fragment}\cdot R_{\rm AA}^{\rm fragment}\cdot(a+1)\cdot v_2^{\rm fragment} + n^{\rm prompt}\cdot b\cdot(a+1)\cdot v_2^{\rm add.}}{(1+aR_{\rm AA}^{\rm fragment}+b)n^{\rm prompt}(a+1)}, \tag{5.15}$$

$$= \frac{aR_{\rm AA}^{\rm fragment}}{1+aR_{\rm AA}^{\rm fragment}+b}v_2^{\rm fragment} + \frac{b}{1+aR_{\rm AA}^{\rm fragment}+b}v_2^{\rm add.}, \tag{5.16}$$

$$\approx \frac{aR_{\rm AA}^{\pi^0}}{1+aR_{\rm AA}^{\pi^0}+b}v_2^{\pi^0} + \frac{b}{1+aR_{\rm AA}^{\pi^0}+b}v_2^{\rm add.}, \tag{5.17}$$

here, we added the two assumptions,

- $v_2^{\rm prompt} = 0$,
- $v_2^{\rm fragment} = v_2^{\pi^0}$.

Then, we obtained the v_2 of additional photon source from measured v_2 of π^0 and direct photon, and parameter a and b as shown in Fig. 5.15. From this calculation, the v_2 of additional photon source has positive finite value about 0.045±0.030 in central collisions.

The strength of additional photon v_2 is investigated from another point of view in Fig. 5.16. According to Eq. (5.17), the v_2 ratio of direct photon and π^0 is described by $R_{\rm AA}^{\pi^0}$, parameter a,

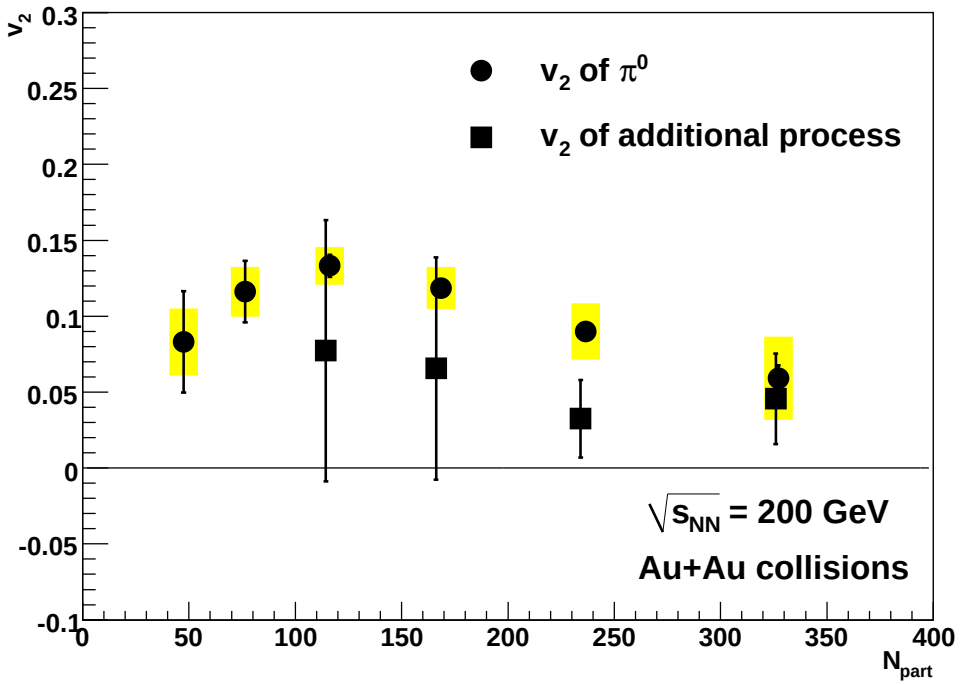

Figure 5.15: Estimated v_2 of additional process in high-p_{T} direct photon as a function of N_{part} in $\sqrt{s_{\mathrm{NN}}} = 200$ GeV Au + Au collisions.

b, and $v_2^{\mathrm{add.}}$. Therefore, $v_2^{\mathrm{add.}}$ is able to speculate from v_2 ratio. The lines in Fig. 5.16 show the expected values of v_2 ratio calculated at $v_2^{\mathrm{add.}} = -0.02, 0.00, 0.02, 0.04, 0.06, 0.08$ and following relation,

$$\frac{v_2^{\mathrm{direct}}}{v_2^{\pi^0}} = \frac{aR_{\mathrm{AA}}^{\pi^0}}{1 + aR_{\mathrm{AA}}^{\pi^0} + b} + \frac{b}{1 + aR_{\mathrm{AA}}^{\pi^0} + b} \frac{v_2^{\mathrm{add.}}}{v_2^{\pi^0}}. \tag{5.18}$$

From the results in Fig. 5.16, the v_2 of additional production source is expected to finite positive value approximately 0.045 $\pm$0.030.

From the results in this section, we confirmed the existence of high-p_{T} photon production source except prompt and jet-fragmentation by R_{AA} measurement of direct photon and π^0 in Au+Au collisions with approximately half ratio of prompt photon. The v_2 of photons resulting from additional source is estimated as 0.045 ± 0.030 which obtained from R_{AA} and v_2 result and some assumptions.

As described in Section 1.4.1, we have a prediction of additional photon source in Au+Au collisions as "photon-conversion". The enhancement of photon yield in Au+Au collisions might be generate by energy loss of hard-scattered partons in the high density medium.

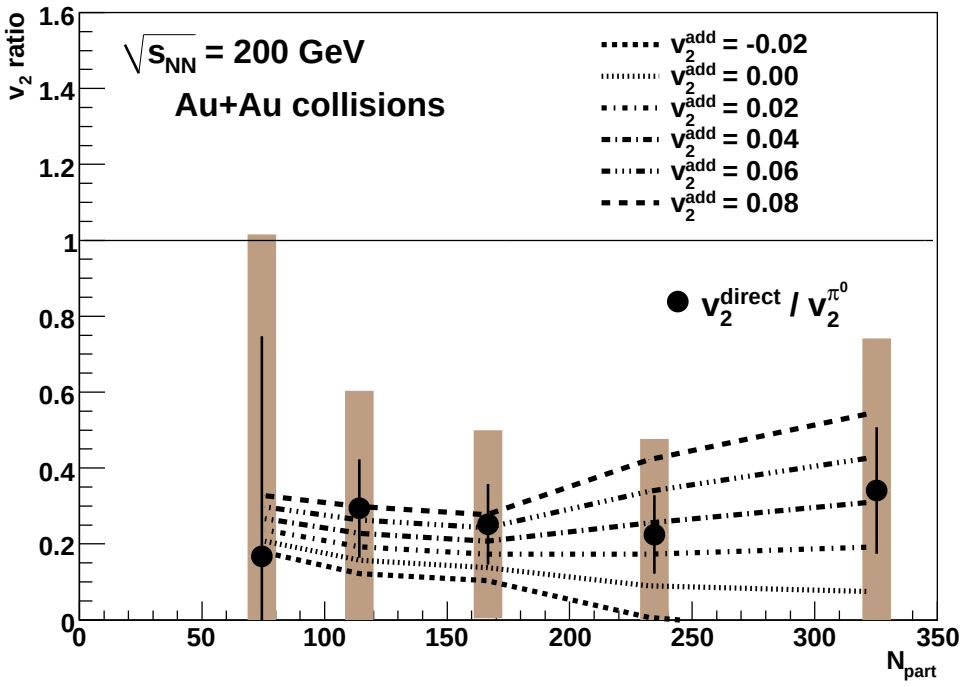

Figure 5.16: The v_2 ratio of direct photon and π^0 as a function of $N_{\rm part}$. Lines show the expected values of v_2 ratio calculated from Eq. 5.17 at $v_2^{\rm add.} = -0.02, 0.00, 0.02, 0.04, 0.06, 0.08$.

5.5 Summary of Discussions

Finally, discussions in this thesis are summarized in the follows;

- The dominant source of direct photon is in fact the prompt photon confirmed by zero v_2 of direct photon.
- Low-$p_{\rm T}$ direct photon has v_2 of positive finite value. Although thermal emission from QGP is expected more dominant process than that from late hadron gas state, the influence of late hadron gas to thermal photon yield might be not negligible.
- Contribution ratio of jet-fragmentation to prompt photon is very small. And we need another emission source in Au+Au collisions. It exists about half amount of prompt photon.
- The v_2 of photons resulting from additional source is expected 0.045 ± 0.030.

Chapter 6

Conclusion

On the study of Quark Gluon Plasma (QGP) state, direct photon is a powerful probe to investigate the hot and dense medium generated by Relativistic Heavy Ion Collider (RHIC), since photons are emitted from every production sources directly without re-scattering to other particles due to their long mean free path. Especially, azimuthal anisotropy parameter v_2 of direct photon is a interesting/important tool to explore the production source of direct photon, because the azimuthal distribution is reflected the properties of their production source.

We have performed measured v_2 of neutral pion and direct photon in $\sqrt{s_{\rm NN}}$ = 200 GeV Au+Au collisions at RHIC-PHENIX, the data set has been taken in the PHENIX Year-7 (about 4 times larger statistics than Year-4). In the study of neutral pion v_2, we obtained not only a consistent result with charged pion in low $p_{\rm T}$, but also extended up to $p_{\rm T}$ = 16 GeV/c for v_2 of π^0. This is also compared with v_2 of non-identified charge hadron and proton-to-pion ratio, then we confirmed valid range of baryon enhancement referring to p+p collisions. The v_2 of direct photon is extracted experimentally from π^0, inclusive photon, and excess ratio of direct photon, then it is calculated up to $p_{\rm T}$ = 16 GeV/c.

Most of direct photons in high-$p_{\rm T}$ are expected to be emitted as prompt photon resulting from initial hard-scattering of parton. The v_2 of direct photon is well described with zero at $p_{\rm T} > 6$ GeV/c, it indicates the dominant source of direct photon is in fact the prompt photon, which has zero v_2. This is also consistent with independent measurement such as non-suppressed direct photon which is confirmed by $R_{\rm AA}$ results of direct photon and π^0.

According to analysis results of this study, we confirmed that there is quite different structure between low-$p_{\rm T}$ ($p_{\rm T} < 3$ GeV/c and $p_{\rm T} > 6$ GeV/c). In order to discuss about low-$p_{\rm T}$ structure of direct photon, v_2 is recalculated using alternative excess ratio which is determined by internal conversion of dilepton. The strength of direct photon v_2 at low-$p_{\rm T}$ indicated the finite positive value, between charged hadron v_2 and $KE_{\rm T}$ scaled charged hadron v_2. Therefore, it does not negligible the thermal emission from late hadron gas state even its temperature is expected lower than thermal emission from QGP.

We investigate the contamination ratio of prompt photon, and jet-fragmentation photon and additional source in Au+Au collisions under some assumption as a discussion at high-$p_{\rm T}$ structure. From the early results of $R_{\rm AA}$, the ratio is estimated as,

$$N^{\rm prompt} : N^{\rm fragment} : N^{\rm additional} = 1.0 : 0.13(\pm 0.01) : 0.5(\pm 0.17), \tag{6.1}$$

therefore, we do not negligible the additional photon source in Au+Au collisions, though prompt photon is still first-order dominant process. If we assumed that v_2 of jet-fragmentation photon is corresponding to that of π^0, the v_2 of additional process is estimated from $R_{\rm AA}$ and contamination ratio of direct photon. As the result of this calculation, we obtained that v_2 of additional process is 0.045 ± 0.030.

When we assumed that enhancement of high-$p_{\rm T}$ direct photon is produced from interaction between hard-scattered parton and hot dense matter, its v_2 is expected a negative sign due to the spatial shape of participant. Although the result of v_2 in this thesis is not represented the negative sign, discussions for the enhancement source of direct photon will be continued with higher statistical and systematical accuracy in future.

Appendix A

Data Tables of Neutral Pion v_2 (RxNP)

- Table A.1 : π^0 v_2 at centrality 00 to 10 % by using RxNP
- Table A.2 : π^0 v_2 at centrality 10 to 20 % by using RxNP
- Table A.3 : π^0 v_2 at centrality 20 to 30 % by using RxNP
- Table A.4 : π^0 v_2 at centrality 30 to 40 % by using RxNP
- Table A.5 : π^0 v_2 at centrality 40 to 50 % by using RxNP
- Table A.6 : π^0 v_2 at centrality 50 to 60 % by using RxNP
- Table A.7 : π^0 v_2 at centrality 00 to 20 % by using RxNP
- Table A.8 : π^0 v_2 at centrality 20 to 40 % by using RxNP
- Table A.9 : π^0 v_2 at centrality 40 to 60 % by using RxNP
- Table A.10 : π^0 v_2 at centrality 00 to 92 % by using RxNP

Table A.1: Neutral pion v_2 as a function of p_T by using RxNP for reaction plane determination (centrality 0 to 10 %).

p_T [GeV/c]	$< p_T >$ [GeV/c]	v_2	statistical error	systematical error
1.25	1.17	0.0564	0.00115	0.0147
1.75	1.63	0.067	0.00113	0.0175
2.25	2.13	0.0751	0.00145	0.0196
2.75	2.64	0.0769	0.00205	0.0201
3.25	3.14	0.0758	0.00294	0.02
3.75	3.65	0.0707	0.00408	0.0189
4.5	4.29	0.0648	0.00444	0.0177
5.5	5.32	0.0467	0.00738	0.0143
6.5	6.35	0.049	0.0113	0.016
7.5	7.36	0.0611	0.0172	0.0201
8.5	8.37	0.0713	0.0338	0.0243
9.5	9.38	0.0957	0.0449	0.0319
11.5	11	0.0958	0.0288	0.0412
14.5	14.1	0.169	0.0717	0.0836

Table A.2: Neutral pion v_2 as a function of p_T by using RxNP for reaction plane determination (centrality 10 to 20 %).

p_T [GeV/c]	$< p_T >$ [GeV/c]	v_2	statistical error	systematical error
1.25	1.17	0.101	0.000806	0.0123
1.75	1.63	0.119	0.000745	0.014
2.25	2.13	0.131	0.000936	0.0153
2.75	2.64	0.134	0.0013	0.0157
3.25	3.14	0.129	0.00184	0.0154
3.75	3.65	0.122	0.00257	0.015
4.5	4.29	0.114	0.00284	0.0148
5.5	5.32	0.0978	0.00503	0.0141
6.5	6.35	0.0951	0.00818	0.0148
7.5	7.36	0.0752	0.0129	0.0147
8.5	8.37	0.0668	0.0241	0.0158
9.5	9.38	0.14	0.0334	0.0219
11.5	11	0.0939	0.0233	0.0235
14.5	14.1	0.0741	0.0577	0.0338

Table A.3: Neutral pion v_2 as a function of p_T by using RxNP for reaction plane determination (centrality 20 to 30 %).

p_T [GeV/c]	$< p_T >$ [GeV/c]	v_2	statistical error	systematical error
1.25	1.17	0.135	0.000761	0.0134
1.75	1.63	0.155	0.000668	0.0147
2.25	2.13	0.166	0.000825	0.0154
2.75	2.64	0.17	0.00115	0.0156
3.25	3.14	0.166	0.00163	0.0153
3.75	3.65	0.154	0.0023	0.0144
4.5	4.29	0.145	0.00261	0.0138
5.5	5.32	0.123	0.00478	0.0123
6.5	6.35	0.127	0.00805	0.013
7.5	7.36	0.12	0.0126	0.013
8.5	8.37	0.063	0.0233	0.0109
9.5	9.38	0.123	0.0327	0.0154
11.5	11	0.0923	0.0242	0.0193
14.5	14.1	0.0345	0.0586	0.0364

Table A.4: Neutral pion v_2 as a function of p_T by using RxNP for reaction plane determination (centrality 30 to 40 %).

p_T [GeV/c]	$< p_T >$ [GeV/c]	v_2	statistical error	systematical error
1.25	1.17	0.154	0.000818	0.0143
1.75	1.63	0.175	0.000689	0.0152
2.25	2.13	0.186	0.000852	0.0158
2.75	2.64	0.186	0.00119	0.0158
3.25	3.14	0.183	0.0017	0.0156
3.75	3.65	0.176	0.00244	0.0151
4.5	4.29	0.158	0.00281	0.0137
5.5	5.32	0.151	0.00537	0.0133
6.5	6.35	0.139	0.00926	0.0126
7.5	7.36	0.138	0.015	0.0128
8.5	8.37	0.119	0.0274	0.0121
9.5	9.38	0.103	0.0397	0.0122
11.5	11	0.0897	0.029	0.0161
14.5	14.1	0.208	0.075	0.0369

Table A.5: Neutral pion v_2 as a function of p_{T} by using RxNP for reaction plane determination (centrality 40 to 50 %).

p_{T} [GeV/c]	$< p_{\mathrm{T}} >$ [GeV/c]	v_2	statistical error	systematical error
1.25	1.17	0.163	0.000983	0.0136
1.75	1.63	0.182	0.000808	0.0144
2.25	2.13	0.193	0.00101	0.0152
2.75	2.64	0.192	0.00142	0.0151
3.25	3.14	0.185	0.00206	0.0146
3.75	3.65	0.181	0.003	0.0143
4.5	4.29	0.167	0.00355	0.0133
5.5	5.32	0.161	0.00688	0.013
6.5	6.35	0.147	0.012	0.0122
7.5	7.36	0.169	0.0202	0.014
8.5	8.37	0.16	0.0337	0.0142
9.5	9.38	0.254	0.0512	0.0217
11.5	11	0.19	0.0402	0.0245
14.5	14.1	0.166	0.097	0.063

Table A.6: Neutral pion v_2 as a function of p_{T} by using RxNP for reaction plane determination (centrality 50 to 60 %).

p_{T} [GeV/c]	$< p_{\mathrm{T}} >$ [GeV/c]	v_2	statistical error	systematical error
1.25	1.17	0.159	0.00134	0.014
1.75	1.63	0.179	0.00111	0.0151
2.25	2.13	0.186	0.00142	0.0157
2.75	2.64	0.19	0.00201	0.016
3.25	3.14	0.183	0.00295	0.0154
3.75	3.65	0.182	0.00437	0.0154
4.5	4.29	0.185	0.00526	0.0156
5.5	5.32	0.183	0.0103	0.0157
6.5	6.35	0.19	0.018	0.0165
7.5	7.36	0.154	0.0294	0.0144
8.5	8.37	0.185	0.052	0.0181
9.5	9.38	0.289	0.0738	0.0276
11.5	11	0.311	0.0606	0.0382
14.5	14.1	0.288	0.164	0.0883

Table A.7: Neutral pion v_2 as a function of p_T by using RxNP for reaction plane determination (centrality 0 to 20 %).

p_T [GeV/c]	$< p_T >$ [GeV/c]	v_2	statistical error	systematical error
1.25	1.17	0.0753	0.000719	0.00821
1.75	1.63	0.0883	0.000681	0.00953
2.25	2.13	0.0984	0.000863	0.0106
2.75	2.64	0.102	0.0012	0.0111
3.25	3.14	0.0998	0.00171	0.0112
3.75	3.65	0.0944	0.00237	0.011
4.5	4.29	0.0876	0.00258	0.011
5.5	5.32	0.0701	0.00442	0.0106
6.5	6.35	0.0697	0.00694	0.0115
7.5	7.36	0.0677	0.0107	0.0125
8.5	8.37	0.0692	0.0207	0.0139
9.5	9.38	0.115	0.028	0.0179
11.5	11	0.0966	0.0187	0.0212
14.5	14.1	0.118	0.0462	0.0347

Table A.8: Neutral pion v_2 as a function of p_T by using RxNP for reaction plane determination (centrality 20 to 40 %).

p_T [GeV/c]	$< p_T >$ [GeV/c]	v_2	statistical error	systematical error
1.25	1.17	0.143	0.000569	0.0138
1.75	1.63	0.163	0.000488	0.0149
2.25	2.13	0.174	0.0006	0.0156
2.75	2.64	0.176	0.00083	0.0158
3.25	3.14	0.173	0.00118	0.0155
3.75	3.65	0.163	0.00167	0.0147
4.5	4.29	0.15	0.00191	0.0138
5.5	5.32	0.135	0.00356	0.0127
6.5	6.35	0.132	0.00605	0.0127
7.5	7.36	0.128	0.00963	0.0126
8.5	8.37	0.0857	0.0177	0.0103
9.5	9.38	0.114	0.025	0.0127
11.5	11	0.0892	0.0185	0.0139
14.5	14.1	0.102	0.0462	0.0231

Table A.9: Neutral pion v_2 as a function of p_{T} by using RxNP for reaction plane determination (centrality 40 to 60 %).

p_{T} [GeV/c]	$< p_{\mathrm{T}} >$ [GeV/c]	v_2	statistical error	systematical error
1.25	1.17	0.161	0.000796	0.0137
1.75	1.63	0.181	0.00065	0.0147
2.25	2.13	0.191	0.000818	0.0154
2.75	2.64	0.191	0.00115	0.0154
3.25	3.14	0.184	0.00167	0.0149
3.75	3.65	0.181	0.00245	0.0147
4.5	4.29	0.174	0.00291	0.0141
5.5	5.32	0.169	0.00567	0.0138
6.5	6.35	0.163	0.00987	0.0135
7.5	7.36	0.163	0.0165	0.0137
8.5	8.37	0.17	0.028	0.0147
9.5	9.38	0.268	0.0412	0.0228
11.5	11	0.228	0.0331	0.0249
14.5	14.1	0.201	0.083	0.0577

Table A.10: Neutral pion v_2 as a function of p_{T} by using RxNP for reaction plane determination (centrality 0 to 92 %).

p_{T} [GeV/c]	$< p_{\mathrm{T}} >$ [GeV/c]	v_2	statistical error	systematical error
1.25	1.17	0.105	0.000478	0.0104
1.75	1.63	0.121	0.000412	0.0118
2.25	2.13	0.132	0.000499	0.0127
2.75	2.64	0.137	0.000665	0.0132
3.25	3.14	0.137	0.00092	0.0132
3.75	3.65	0.132	0.00127	0.013
4.5	4.29	0.128	0.0014	0.0128
5.5	5.32	0.118	0.00251	0.0122
6.5	6.35	0.114	0.00413	0.0123
7.5	7.36	0.114	0.00655	0.0129
8.5	8.37	0.105	0.0121	0.0129
9.5	9.38	0.148	0.0169	0.0167
11.5	11	0.12	0.0122	0.0175
14.5	14.1	0.139	0.0303	0.0258

Appendix B

Data Tables of Neutral Pion v_2 (BBC)

- Table B.1 : π^0 v_2 at centrality 00 to 10 % by using BBC
- Table B.2 : π^0 v_2 at centrality 10 to 20 % by using BBC
- Table B.3 : π^0 v_2 at centrality 20 to 30 % by using BBC
- Table B.4 : π^0 v_2 at centrality 30 to 40 % by using BBC
- Table B.5 : π^0 v_2 at centrality 40 to 50 % by using BBC
- Table B.6 : π^0 v_2 at centrality 50 to 60 % by using BBC
- Table B.7 : π^0 v_2 at centrality 00 to 20 % by using BBC
- Table B.8 : π^0 v_2 at centrality 20 to 40 % by using BBC
- Table B.9 : π^0 v_2 at centrality 40 to 60 % by using BBC
- Table B.10 : π^0 v_2 at centrality 00 to 92 % by using BBC

Table B.1: Neutral pion v_2 as a function of p_T by using BBC for reaction plane determination (centrality 0 to 10 %).

p_T [GeV/c]	$< p_T >$ [GeV/c]	v_2	statistical error	systematical error
1.25	1.17	0.0557	0.00242	0.0146
1.75	1.63	0.0719	0.00236	0.0181
2.25	2.13	0.081	0.00304	0.0204
2.75	2.64	0.0819	0.00431	0.0208
3.25	3.14	0.088	0.00618	0.0216
3.75	3.65	0.0714	0.00856	0.0189
4.5	4.29	0.0611	0.00935	0.0173
5.5	5.32	0.0755	0.0155	0.0179
6.5	6.35	0.0328	0.0237	0.0146
7.5	7.36	0.0571	0.0361	0.0197
8.5	8.37	-0.03	0.0646	0.0213
9.5	9.38	0.00696	0.0863	0.0267
11.5	11	-0.00967	0.0627	0.0373
14.5	14.1	0.272	0.158	0.0921

Table B.2: Neutral pion v_2 as a function of p_T by using BBC for reaction plane determination (centrality 10 to 20 %).

p_T [GeV/c]	$< p_T >$ [GeV/c]	v_2	statistical error	systematical error
1.25	1.17	0.103	0.00152	0.0123
1.75	1.63	0.118	0.00141	0.014
2.25	2.13	0.133	0.00177	0.0154
2.75	2.64	0.138	0.00246	0.0159
3.25	3.14	0.13	0.00349	0.0155
3.75	3.65	0.125	0.00487	0.0152
4.5	4.29	0.114	0.00537	0.0147
5.5	5.32	0.0983	0.0095	0.0141
6.5	6.35	0.105	0.0153	0.0152
7.5	7.36	0.0593	0.0244	0.0143
8.5	8.37	0.0931	0.0425	0.0165
9.5	9.38	0.082	0.0561	0.0202
11.5	11	6.82e-05	0.045	0.0225
14.5	14.1	-0.00497	0.109	0.0334

Table B.3: Neutral pion v_2 as a function of p_T by using BBC for reaction plane determination (centrality 20 to 30 %).

p_T [GeV/c]	$< p_T >$ [GeV/c]	v_2	statistical error	systematical error
1.25	1.17	0.14	0.00143	0.0136
1.75	1.63	0.158	0.00126	0.0148
2.25	2.13	0.171	0.00156	0.0156
2.75	2.64	0.174	0.00217	0.0158
3.25	3.14	0.175	0.00307	0.0157
3.75	3.65	0.161	0.00434	0.0147
4.5	4.29	0.149	0.00492	0.0139
5.5	5.32	0.131	0.00902	0.0126
6.5	6.35	0.13	0.0151	0.0131
7.5	7.36	0.119	0.0237	0.013
8.5	8.37	0.0652	0.0409	0.0109
9.5	9.38	0.12	0.0575	0.0154
11.5	11	0.0699	0.0464	0.0189
14.5	14.1	0.146	0.113	0.0374

Table B.4: Neutral pion v_2 as a function of p_T by using BBC for reaction plane determination (centrality 30 to 40 %).

p_T [GeV/c]	$< p_T >$ [GeV/c]	v_2	statistical error	systematical error
1.25	1.17	0.156	0.00162	0.0144
1.75	1.63	0.18	0.00137	0.0154
2.25	2.13	0.192	0.0017	0.0161
2.75	2.64	0.195	0.00236	0.0162
3.25	3.14	0.188	0.00338	0.0158
3.75	3.65	0.176	0.00485	0.0151
4.5	4.29	0.158	0.00557	0.0137
5.5	5.32	0.162	0.0106	0.0137
6.5	6.35	0.141	0.018	0.0127
7.5	7.36	0.129	0.0299	0.0125
8.5	8.37	0.2	0.0511	0.0152
9.5	9.38	0.0963	0.0727	0.012
11.5	11	-0.021	0.0598	0.0153
14.5	14.1	-0.105	0.154	0.0354

Table B.5: Neutral pion v_2 as a function of p_T by using BBC for reaction plane determination (centrality 40 to 50 %).

p_T [GeV/c]	$< p_T >$ [GeV/c]	v_2	statistical error	systematical error
1.25	1.17	0.166	0.00211	0.0137
1.75	1.63	0.187	0.00174	0.0146
2.25	2.13	0.196	0.00218	0.0153
2.75	2.64	0.188	0.00306	0.015
3.25	3.14	0.189	0.00444	0.0147
3.75	3.65	0.169	0.00646	0.0138
4.5	4.29	0.162	0.00763	0.0131
5.5	5.32	0.14	0.0147	0.0122
6.5	6.35	0.134	0.0259	0.0117
7.5	7.36	0.0801	0.0436	0.0115
8.5	8.37	0.137	0.0691	0.0135
9.5	9.38	0.165	0.106	0.019
11.5	11	-0.0285	0.0919	0.0223
14.5	14.1	0.326	0.213	0.0648

Table B.6: Neutral pion v_2 as a function of p_T by using BBC for reaction plane determination (centrality 50 to 60 %).

p_T [GeV/c]	$< p_T >$ [GeV/c]	v_2	statistical error	systematical error
1.25	1.17	0.165	0.00316	0.0142
1.75	1.63	0.181	0.00261	0.0152
2.25	2.13	0.187	0.00335	0.0157
2.75	2.64	0.176	0.00475	0.0154
3.25	3.14	0.168	0.00696	0.0148
3.75	3.65	0.147	0.0103	0.014
4.5	4.29	0.16	0.0124	0.0147
5.5	5.32	0.166	0.0243	0.015
6.5	6.35	0.0848	0.0431	0.0131
7.5	7.36	0.142	0.0705	0.014
8.5	8.37	-0.117	0.121	0.016
9.5	9.38	0.286	0.164	0.0275
11.5	11	-0.0568	0.145	0.0337
14.5	14.1	-0.146	0.388	0.0871

Table B.7: Neutral pion v_2 as a function of p_T by using BBC for reaction plane determination (centrality 0 to 20 %).

p_T [GeV/c]	$< p_T >$ [GeV/c]	v_2	statistical error	systematical error
1.25	1.17	0.0755	0.00147	0.00822
1.75	1.63	0.091	0.0014	0.00965
2.25	2.13	0.103	0.00178	0.0108
2.75	2.64	0.107	0.00248	0.0113
3.25	3.14	0.107	0.00351	0.0115
3.75	3.65	0.0961	0.00487	0.0111
4.5	4.29	0.0852	0.00532	0.0109
5.5	5.32	0.086	0.00907	0.0111
6.5	6.35	0.0653	0.0142	0.0114
7.5	7.36	0.0581	0.0221	0.0123
8.5	8.37	0.0266	0.0391	0.0132
9.5	9.38	0.0397	0.052	0.0163
11.5	11	-0.00284	0.0395	0.0201
14.5	14.1	0.12	0.0979	0.0347

Table B.8: Neutral pion v_2 as a function of p_T by using BBC for reaction plane determination (centrality 20 to 40 %).

p_T [GeV/c]	$< p_T >$ [GeV/c]	v_2	statistical error	systematical error
1.25	1.17	0.146	0.00108	0.014
1.75	1.63	0.167	0.000933	0.0151
2.25	2.13	0.179	0.00115	0.0158
2.75	2.64	0.182	0.00159	0.016
3.25	3.14	0.18	0.00226	0.0158
3.75	3.65	0.167	0.00321	0.0149
4.5	4.29	0.153	0.00365	0.0139
5.5	5.32	0.144	0.0068	0.013
6.5	6.35	0.135	0.0114	0.0128
7.5	7.36	0.123	0.0184	0.0125
8.5	8.37	0.12	0.0315	0.0114
9.5	9.38	0.11	0.0447	0.0126
11.5	11	0.0335	0.0364	0.013
14.5	14.1	0.0551	0.0902	0.0225

Table B.9: Neutral pion v_2 as a function of p_T by using BBC for reaction plane determination (centrality 40 to 60 %).

p_T [GeV/c]	$< p_T >$ [GeV/c]	v_2	statistical error	systematical error
1.25	1.17	0.166	0.00173	0.0139
1.75	1.63	0.185	0.00142	0.0148
2.25	2.13	0.193	0.00179	0.0155
2.75	2.64	0.184	0.00251	0.0152
3.25	3.14	0.182	0.00365	0.0148
3.75	3.65	0.161	0.00533	0.0139
4.5	4.29	0.161	0.00634	0.0137
5.5	5.32	0.15	0.0123	0.0131
6.5	6.35	0.116	0.0217	0.0119
7.5	7.36	0.105	0.036	0.0118
8.5	8.37	0.0426	0.0584	0.0115
9.5	9.38	0.214	0.086	0.0209
11.5	11	-0.0217	0.0752	0.0214
14.5	14.1	0.192	0.186	0.0576

Table B.10: Neutral pion v_2 as a function of p_T by using BBC for reaction plane determination (centrality 0 to 92 %).

p_T [GeV/c]	$< p_T >$ [GeV/c]	v_2	statistical error	systematical error
1.25	1.17	0.106	0.000965	0.0105
1.75	1.63	0.123	0.000833	0.0119
2.25	2.13	0.134	0.00101	0.0128
2.75	2.64	0.14	0.00135	0.0133
3.25	3.14	0.14	0.00187	0.0134
3.75	3.65	0.129	0.00257	0.0129
4.5	4.29	0.121	0.00284	0.0125
5.5	5.32	0.12	0.00508	0.0123
6.5	6.35	0.0946	0.00835	0.0117
7.5	7.36	0.0993	0.0133	0.0124
8.5	8.37	0.0398	0.0229	0.0114
9.5	9.38	0.0749	0.0318	0.0146
11.5	11	0.0213	0.0256	0.0158
14.5	14.1	0.0818	0.0632	0.0249

Appendix C

Data Tables of Direct Photon v_2 (RxNP)

- Table C.1 : Direct photon v_2 at centrality 00 to 10 % by using RxNP
- Table C.2 : Direct photon v_2 at centrality 10 to 20 % by using RxNP
- Table C.3 : Direct photon v_2 at centrality 20 to 30 % by using RxNP
- Table C.4 : Direct photon v_2 at centrality 30 to 40 % by using RxNP
- Table C.5 : Direct photon v_2 at centrality 40 to 50 % by using RxNP
- Table C.6 : Direct photon v_2 at centrality 50 to 60 % by using RxNP
- Table C.7 : Direct photon v_2 at centrality 00 to 20 % by using RxNP
- Table C.8 : Direct photon v_2 at centrality 20 to 40 % by using RxNP
- Table C.9 : Direct photon v_2 at centrality 40 to 60 % by using RxNP
- Table C.10 : Direct photon v_2 at centrality 00 to 92 % by using RxNP

Table C.1: Direct photon v_2 as a function of p_T by using RxNP for reaction plane determination (centrality 0 to 10 %).

p_T [GeV/c]	$< p_T >$ [GeV/c]	v_2	statistical error	systematical error
1.25	1.17	0.000561	0.082	0.316
1.75	1.63	0.0587	0.0202	0.11
2.25	2.14	0.132	0.0206	0.123
2.75	2.64	0.102	0.0154	0.0942
3.25	3.15	0.0677	0.0108	0.0545
3.75	3.66	0.0224	0.0149	0.0552
4.5	4.32	0.0392	0.0109	0.0343
5.5	5.35	0.0221	0.0121	0.0216
6.5	6.37	0.0195	0.0133	0.0158
7.5	7.38	0.00302	0.019	0.0161
8.5	8.39	0.0798	0.0288	0.0221
9.5	9.4	0.0148	0.039	0.0232
11.5	11.1	0.00415	0.0305	0.0338
14.5	14.1	0.112	0.0595	0.0597

Table C.2: Direct photon v_2 as a function of p_T by using RxNP for reaction plane determination (centrality 10 to 20 %).

p_T [GeV/c]	$< p_T >$ [GeV/c]	v_2	statistical error	systematical error
1.25	1.17	-0.354	2.87	14.8
1.75	1.63	0.071	0.0521	0.376
2.25	2.14	0.333	0.17	1.09
2.75	2.64	0.153	0.0124	0.141
3.25	3.15	0.125	0.0107	0.0952
3.75	3.66	0.077	0.0136	0.0789
4.5	4.32	0.0498	0.0105	0.053
5.5	5.35	0.0207	0.0137	0.0331
6.5	6.37	0.0252	0.013	0.0203
7.5	7.38	0.0172	0.0213	0.0221
8.5	8.39	0.0369	0.0269	0.0192
9.5	9.4	-0.0112	0.0291	0.0226
11.5	11.1	0.012	0.03	0.0375
14.5	14.1	-0.0469	0.0563	0.0682

Table C.3: Direct photon v_2 as a function of p_T by using RxNP for reaction plane determination (centrality 20 to 30 %).

p_T [GeV/c]	$< p_T >$ [GeV/c]	v_2	statistical error	systematical error
1.25	1.17	0.0116	0.0576	0.328
1.75	1.63	-0.0979	0.601	3.9
2.25	2.14	0.00525	0.141	0.974
2.75	2.64	0.154	0.0129	0.158
3.25	3.15	0.163	0.0108	0.0972
3.75	3.66	0.0944	0.0155	0.0881
4.5	4.32	0.0695	0.0121	0.0615
5.5	5.35	0.0254	0.0158	0.0406
6.5	6.37	0.0336	0.0188	0.0277
7.5	7.38	0.0312	0.0248	0.0233
8.5	8.39	0.0243	0.0384	0.0257
9.5	9.4	0.0564	0.0518	0.0307
11.5	11.1	0.00825	0.0337	0.0405
14.5	14.1	0.133	0.0844	0.0932

Table C.4: Direct photon v_2 as a function of p_T by using RxNP for reaction plane determination (centrality 30 to 40 %).

p_T [GeV/c]	$< p_T >$ [GeV/c]	v_2	statistical error	systematical error
1.25	1.17	-0.0402	0.114	0.62
1.75	1.63	0.207	0.0156	0.12
2.25	2.14	0.115	0.0504	0.417
2.75	2.64	0.15	0.0238	0.225
3.25	3.15	0.125	0.013	0.0892
3.75	3.66	0.0952	0.0142	0.0646
4.5	4.32	0.0814	0.0142	0.051
5.5	5.35	0.0484	0.0211	0.0401
6.5	6.37	0.0235	0.0249	0.0347
7.5	7.38	0.0202	0.0358	0.0344
8.5	8.39	0.0709	0.0496	0.0325
9.5	9.4	0.0195	0.0734	0.0471
11.5	11.1	0.113	0.049	0.0543
14.5	14.1	0.116	0.133	0.112

Table C.5: Direct photon v_2 as a function of p_T by using RxNP for reaction plane determination (centrality 40 to 50 %).

p_T [GeV/c]	$< p_T >$ [GeV/c]	v_2	statistical error	systematical error
1.25	1.17	-0.302	0.399	2.35
1.75	1.63	0.227	0.0141	0.0924
2.25	2.14	0.188	0.03	0.23
2.75	2.64	0.117	0.0409	0.278
3.25	3.15	0.104	0.0197	0.102
3.75	3.66	0.0777	0.0254	0.0976
4.5	4.32	0.045	0.0287	0.0909
5.5	5.35	0.0474	0.0338	0.053
6.5	6.37	0.0154	0.0482	0.0512
7.5	7.38	0.0984	0.0617	0.032
8.5	8.39	-0.0791	0.153	0.124
9.5	9.4	0.0332	0.107	0.0726
11.5	11.1	-0.0529	0.108	0.119
14.5	14.1	-0.0385	0.246	0.241

Table C.6: Direct photon v_2 as a function of p_T by using RxNP for reaction plane determination (centrality 50 to 60 %).

p_T [GeV/c]	$< p_T >$ [GeV/c]	v_2	statistical error	systematical error
1.25	1.17	-7.99	165	1.01e+03
1.75	1.63	0.143	0.0106	0.0658
2.25	2.14	0.173	0.0206	0.119
2.75	2.64	0.144	0.0577	0.282
3.25	3.15	0.135	0.0397	0.133
3.75	3.66	0.137	0.0411	0.0822
4.5	4.32	0.0438	0.0498	0.129
5.5	5.35	0.0923	0.0564	0.0551
6.5	6.37	0.087	0.0785	0.0554
7.5	7.38	0.255	0.133	0.0735
8.5	8.39	0.201	0.152	0.0758
9.5	9.4	0.23	0.2	0.103
11.5	11.1	0.184	0.195	0.202
14.5	14.1	-0.045	0.37	0.324

Table C.7: Direct photon v_2 as a function of p_{T} by using RxNP for reaction plane determination (centrality 0 to 20 %).

p_{T} [GeV/c]	$< p_{\mathrm{T}} >$ [GeV/c]	v_2	statistical error	systematical error
1.25	1.17	0.0367	0.178	0.929
1.75	1.63	0.209	0.0741	0.432
2.25	2.14	0.209	0.0509	0.326
2.75	2.64	0.119	0.0104	0.112
3.25	3.15	0.0755	0.00853	0.0724
3.75	3.66	0.0455	0.0112	0.0664
4.5	4.32	0.0408	0.00811	0.0425
5.5	5.35	0.0243	0.00953	0.0254
6.5	6.37	0.0208	0.00952	0.0173
7.5	7.38	0.00518	0.0147	0.0173
8.5	8.39	0.062	0.0199	0.014
9.5	9.4	0.0019	0.0241	0.0173
11.5	11.1	0.00676	0.0217	0.0208
14.5	14.1	0.0515	0.041	0.0283

Table C.8: Direct photon v_2 as a function of p_{T} by using RxNP for reaction plane determination (centrality 20 to 40 %).

p_{T} [GeV/c]	$< p_{\mathrm{T}} >$ [GeV/c]	v_2	statistical error	systematical error
1.25	1.17	0.0282	0.0591	0.341
1.75	1.63	0.103	0.0365	0.281
2.25	2.14	0.0676	0.078	0.611
2.75	2.64	0.154	0.0126	0.186
3.25	3.15	0.154	0.00784	0.0893
3.75	3.66	0.091	0.0116	0.0764
4.5	4.32	0.0746	0.0101	0.0566
5.5	5.35	0.0353	0.014	0.0403
6.5	6.37	0.0318	0.0155	0.0299
7.5	7.38	0.0288	0.021	0.0251
8.5	8.39	0.0443	0.0305	0.0222
9.5	9.4	0.0446	0.0426	0.0261
11.5	11.1	0.0508	0.0282	0.0263
14.5	14.1	0.126	0.0716	0.0545

Table C.9: Direct photon v_2 as a function of p_T by using RxNP for reaction plane determination (centrality 40 to 60 %).

p_T [GeV/c]	$< p_T >$ [GeV/c]	v_2	statistical error	systematical error
1.25	1.17	-0.847	1.72	10.3
1.75	1.63	0.2	0.00737	0.0602
2.25	2.14	0.186	0.0154	0.145
2.75	2.64	0.122	0.0387	0.29
3.25	3.15	0.113	0.0205	0.117
3.75	3.66	0.0807	0.0247	0.104
4.5	4.32	0.0439	0.029	0.105
5.5	5.35	0.0659	0.0309	0.0527
6.5	6.37	0.0433	0.0427	0.0479
7.5	7.38	0.15	0.0576	0.0307
8.5	8.39	0.0439	0.108	0.0736
9.5	9.4	0.102	0.0966	0.0649
11.5	11.1	0.0338	0.101	0.113
14.5	14.1	-0.0408	0.206	0.211

Table C.10: Direct photon v_2 as a function of p_T by using RxNP for reaction plane determination (centrality 0 to 92 %).

p_T [GeV/c]	$< p_T >$ [GeV/c]	v_2	statistical error	systematical error
1.25	1.17	0.108	0.0137	0.137
1.75	1.63	0.117	0.0197	0.239
2.25	2.14	0.214	0.0182	0.229
2.75	2.64	0.152	0.0056	0.101
3.25	3.15	0.0928	0.00529	0.0694
3.75	3.66	0.0675	0.00683	0.0627
4.5	4.32	0.0477	0.00603	0.0485
5.5	5.35	0.045	0.0071	0.0304
6.5	6.37	0.0457	0.00779	0.0221
7.5	7.38	0.0429	0.0115	0.021
8.5	8.39	0.0646	0.0164	0.0194
9.5	9.4	0.0314	0.0205	0.0242
11.5	11.1	0.0213	0.0169	0.025
14.5	14.1	0.05	0.0357	0.0297

Appendix D

Data Tables of Direct Photon v_2 (BBC)

- Table D.1 : Direct photon v_2 at centrality 00 to 10 % by using BBC
- Table D.2 : Direct photon v_2 at centrality 10 to 20 % by using BBC
- Table D.3 : Direct photon v_2 at centrality 20 to 30 % by using BBC
- Table D.4 : Direct photon v_2 at centrality 30 to 40 % by using BBC
- Table D.5 : Direct photon v_2 at centrality 40 to 50 % by using BBC
- Table D.6 : Direct photon v_2 at centrality 50 to 60 % by using BBC
- Table D.7 : Direct photon v_2 at centrality 00 to 20 % by using BBC
- Table D.8 : Direct photon v_2 at centrality 20 to 40 % by using BBC
- Table D.9 : Direct photon v_2 at centrality 40 to 60 % by using BBC
- Table D.10 : Direct photon v_2 at centrality 00 to 92 % by using BBC

Table D.1: Direct photon v_2 as a function of p_{T} by using BBC for reaction plane determination (centrality 0 to 10 %).

p_{T} [GeV/c]	$< p_{\mathrm{T}} >$ [GeV/c]	v_2	statistical error	systematical error
1.25	1.17	0.0603	9.29e-05	0.0117
1.75	1.63	0.0725	0.00021	0.0142
2.25	2.14	0.078	0.000442	0.0164
2.75	2.64	0.0794	0.000865	0.018
3.25	3.15	0.0721	0.00157	0.0173
3.75	3.66	0.0666	0.00262	0.0167
4.5	4.32	0.0544	0.00338	0.0139
5.5	5.35	0.0431	0.00678	0.0112
6.5	6.37	0.0253	0.0116	0.00852
7.5	7.38	0.0278	0.0183	0.00896
8.5	8.39	0.0158	0.0272	0.00909
9.5	9.4	0.0495	0.0387	0.0141
11.5	11.1	-0.0261	0.0376	0.0189
14.5	14.1	-0.0412	0.0827	0.0379

Table D.2: Direct photon v_2 as a function of p_{T} by using BBC for reaction plane determination (centrality 10 to 20 %).

p_{T} [GeV/c]	$< p_{\mathrm{T}} >$ [GeV/c]	v_2	statistical error	systematical error
1.25	1.17	0.105	7.54e-05	0.00802
1.75	1.63	0.124	0.000166	0.00974
2.25	2.14	0.134	0.000345	0.0135
2.75	2.64	0.133	0.000666	0.0164
3.25	3.15	0.126	0.00119	0.0164
3.75	3.66	0.114	0.00198	0.0148
4.5	4.32	0.0918	0.00255	0.0129
5.5	5.35	0.0757	0.00511	0.0102
6.5	6.37	0.0483	0.00891	0.00824
7.5	7.38	0.0684	0.0142	0.00889
8.5	8.39	0.0682	0.0213	0.00973
9.5	9.4	-0.0262	0.0297	0.0109
11.5	11.1	0.0385	0.0294	0.0206
14.5	14.1	-0.0806	0.0656	0.0467

Table D.3: Direct photon v_2 as a function of p_T by using BBC for reaction plane determination (centrality 20 to 30 %).

p_T [GeV/c]	$< p_T >$ [GeV/c]	v_2	statistical error	systematical error
1.25	1.17	0.136	8.49e-05	0.00831
1.75	1.63	0.159	0.000188	0.00971
2.25	2.14	0.169	0.000388	0.0138
2.75	2.64	0.167	0.000739	0.0162
3.25	3.15	0.157	0.00131	0.016
3.75	3.66	0.141	0.00216	0.0144
4.5	4.32	0.12	0.00277	0.0139
5.5	5.35	0.0855	0.0056	0.0106
6.5	6.37	0.0626	0.00986	0.00885
7.5	7.38	0.0577	0.0157	0.00888
8.5	8.39	0.0486	0.0237	0.0102
9.5	9.4	0.0435	0.0341	0.013
11.5	11.1	0.0405	0.0339	0.0232
14.5	14.1	-0.0758	0.0736	0.0493

Table D.4: Direct photon v_2 as a function of p_T by using BBC for reaction plane determination (centrality 30 to 40 %).

p_T [GeV/c]	$< p_T >$ [GeV/c]	v_2	statistical error	systematical error
1.25	1.17	0.156	0.000115	0.00942
1.75	1.63	0.18	0.000254	0.0104
2.25	2.14	0.188	0.000519	0.0139
2.75	2.64	0.185	0.00098	0.0156
3.25	3.15	0.174	0.00172	0.0148
3.75	3.66	0.158	0.00281	0.0127
4.5	4.32	0.135	0.00359	0.011
5.5	5.35	0.108	0.00727	0.01
6.5	6.37	0.0763	0.0129	0.00981
7.5	7.38	0.0794	0.0207	0.0115
8.5	8.39	0.0755	0.0312	0.014
9.5	9.4	0.0537	0.0455	0.0176
11.5	11.1	0.0532	0.046	0.0291
14.5	14.1	0.0385	0.113	0.0555

Table D.5: Direct photon v_2 as a function of p_{T} by using BBC for reaction plane determination (centrality 40 to 50 %).

p_{T} [GeV/c]	$< p_{\mathrm{T}} >$ [GeV/c]	v_2	statistical error	systematical error
1.25	1.17	0.162	0.00018	0.0102
1.75	1.63	0.186	0.000396	0.0108
2.25	2.14	0.193	0.000803	0.013
2.75	2.64	0.187	0.0015	0.0142
3.25	3.15	0.17	0.0026	0.0131
3.75	3.66	0.159	0.00422	0.0119
4.5	4.32	0.141	0.00537	0.0102
5.5	5.35	0.109	0.0109	0.0075
6.5	6.37	0.0849	0.0196	0.0067
7.5	7.38	0.0839	0.0313	0.00871
8.5	8.39	0.000512	0.05	0.0122
9.5	9.4	0.179	0.069	0.0214
11.5	11.1	0.0866	0.0703	0.0399
14.5	14.1	-0.132	0.18	0.0874

Table D.6: Direct photon v_2 as a function of p_{T} by using BBC for reaction plane determination (centrality 50 to 60 %).

p_{T} [GeV/c]	$< p_{\mathrm{T}} >$ [GeV/c]	v_2	statistical error	systematical error
1.25	1.17	0.156	0.000325	0.0122
1.75	1.63	0.174	0.000715	0.0125
2.25	2.14	0.178	0.00144	0.0139
2.75	2.64	0.17	0.00266	0.0142
3.25	3.15	0.172	0.00458	0.0141
3.75	3.66	0.156	0.00741	0.0125
4.5	4.32	0.135	0.00941	0.0123
5.5	5.35	0.122	0.019	0.0111
6.5	6.37	0.0876	0.0339	0.0121
7.5	7.38	0.0274	0.0567	0.0162
8.5	8.39	0.078	0.0874	0.0247
9.5	9.4	-0.017	0.122	0.0357
11.5	11.1	0.0478	0.128	0.0681
14.5	14.1	-0.0324	0.336	0.141

Table D.7: Direct photon v_2 as a function of p_T by using BBC for reaction plane determination (centrality 0 to 20 %).

p_T [GeV/c]	$< p_T >$ [GeV/c]	v_2	statistical error	systematical error
1.25	1.17	0.0785	5.86e-05	0.00627
1.75	1.63	0.0939	0.00013	0.00771
2.25	2.14	0.102	0.000272	0.0109
2.75	2.64	0.103	0.000528	0.0135
3.25	3.15	0.0958	0.000947	0.0137
3.75	3.66	0.0873	0.00158	0.0131
4.5	4.32	0.0709	0.00204	0.0112
5.5	5.35	0.0575	0.00408	0.00934
6.5	6.37	0.0353	0.00707	0.00768
7.5	7.38	0.0451	0.0112	0.0072
8.5	8.39	0.0381	0.0168	0.00665
9.5	9.4	0.0169	0.0236	0.00635
11.5	11.1	0.00171	0.0232	0.00857
14.5	14.1	-0.0576	0.0514	0.018

Table D.8: Direct photon v_2 as a function of p_T by using BBC for reaction plane determination (centrality 20 to 40 %).

p_T [GeV/c]	$< p_T >$ [GeV/c]	v_2	statistical error	systematical error
1.25	1.17	0.144	6.83e-05	0.00876
1.75	1.63	0.167	0.000151	0.01
2.25	2.14	0.177	0.000311	0.0138
2.75	2.64	0.174	0.00059	0.0159
3.25	3.15	0.164	0.00104	0.0155
3.75	3.66	0.148	0.00171	0.0137
4.5	4.32	0.126	0.00219	0.0126
5.5	5.35	0.0947	0.00443	0.0106
6.5	6.37	0.0683	0.00783	0.00931
7.5	7.38	0.0667	0.0125	0.00901
8.5	8.39	0.0597	0.0189	0.00902
9.5	9.4	0.0476	0.0273	0.00964
11.5	11.1	0.0456	0.0273	0.0141
14.5	14.1	-0.0346	0.0617	0.0279

Table D.9: Direct photon v_2 as a function of p_{T} by using BBC for reaction plane determination (centrality 40 to 60 %).

p_{T} [GeV/c]	$< p_{\mathrm{T}} >$ [GeV/c]	v_2	statistical error	systematical error
1.25	1.17	0.16	0.000157	0.0109
1.75	1.63	0.182	0.000347	0.0114
2.25	2.14	0.187	0.000702	0.0133
2.75	2.64	0.181	0.00131	0.0141
3.25	3.15	0.171	0.00226	0.0133
3.75	3.66	0.158	0.00367	0.0117
4.5	4.32	0.139	0.00467	0.011
5.5	5.35	0.114	0.00947	0.00859
6.5	6.37	0.086	0.0169	0.00757
7.5	7.38	0.0632	0.0274	0.00866
8.5	8.39	0.0298	0.0434	0.0121
9.5	9.4	0.106	0.0601	0.019
11.5	11.1	0.0725	0.0617	0.0366
14.5	14.1	-0.103	0.158	0.0797

Table D.10: Direct photon v_2 as a function of p_{T} by using BBC for reaction plane determination (centrality 0 to 92 %).

p_{T} [GeV/c]	$< p_{\mathrm{T}} >$ [GeV/c]	v_2	statistical error	systematical error
1.25	1.17	0.107	4.27e-05	0.00682
1.75	1.63	0.125	9.46e-05	0.00808
2.25	2.14	0.134	0.000196	0.0114
2.75	2.64	0.135	0.000376	0.0136
3.25	3.15	0.127	0.000667	0.0135
3.75	3.66	0.115	0.0011	0.0119
4.5	4.32	0.1	0.00142	0.0108
5.5	5.35	0.0794	0.00285	0.00942
6.5	6.37	0.0567	0.005	0.0084
7.5	7.38	0.0485	0.00797	0.00812
8.5	8.39	0.0554	0.012	0.0085
9.5	9.4	0.0591	0.0171	0.00905
11.5	11.1	0.0222	0.0169	0.0102
14.5	14.1	-0.0601	0.0382	0.0156

Bibliography

[1] G. F. Chapline, M. H. Johnson, E. Teller, and M. S. Weiss, "Highly excited nuclear matter", Phys. Rev. **D8**:4302-4308, (1973)

[2] T. D. Lee, "Abnormal nuclear states and vacuum excitation", Rev. Mod. Phys. **47**:267-275, (1975)

[3] T. D. Lee and G. C. Wick, "Vacuum stability and vacuum excitation in a spin-0 field theory", Phys. Rev., **D9**:2291-2316, (1974)

[4] T. D. Lee, "Is the physical vacuum a medium?", cU-TP-170, Trans. N. Y. Acad. Sci. Ser. 2, 40, (1979)

[5] E. V. Shuryak, "Quantum Chromodynamics and the theory of superdense matter", Phys. Rept., **61**:177-180, (1980)

[6] F. Karsch, E. Laermann, and A. Peikert, "The pressure in 2, 2+1, and 3 flavour QCD", Phys. Lett. **B478**, 447, (2000)

[7] WA98 Collaboration, "Large acceptance measurement of photons and charged particles in heavy ion reactions". CERN SPSLC/91-17, (1991)

[8] K. Guettler et al., "Inclusive production of low-momentum charged pions at $x = 0$ at the CERN intersecting storage rings", Phys. Rev. **D64**, 111, (1976)

[9] J. Y. Ollitrault, "Differential measure of response to initial geometry", Phys. Rev. **D46**, 229, (1992)

[10] Michael L. Miller, Klaus Reygers, Stephen J. Sanders, Peter Steinberg, "Glauber modeling in high energy nuclear collisions", nucl-ex/0701025, (2007)

[11] M. N. Ericson et al., "Development of a front end controller/heap manager for PHENIX", IEEE Trans. Nucl. Sci., vol. 44, No. 3, 312, (1997)

[12] P. Braun-Munzinger, D. Magestro, K. Redlich, and J. Stachel, "Hadron production in Au+Au collisions at RHIC", Phys. Lett. **B518**, 41, (2001)

[13] PHOBOS Collaboration, B. B. Back et al., "Ratios of charged antiparticles to particles near midrapidity in Au+Au collisions at $\sqrt{s_{\rm NN}} = 200$ GeV", Phys. Rev. **C67**, 021901, (2003)

[14] BRAHMS Collaboration, I. G. Bearden et al., "Rapidity dependence of charged antihadron to hadron ratios in Au+Au collisions at $\sqrt{s_{\rm NN}}$ = 200 GeV", Phys. Rev. Lett. **90**, 102301, (2003)

[15] STAR Collaboration, J. Adams et al., "Identified particle distributions in pp and Au+Au collisions at $\sqrt{s_{\rm NN}}$ = 200 GeV", Phys. Rev. Lett. **92**, 112301, (2004)

[16] L. Aphecetche et al., "The PHENIX calorimeter", NIM, **A499**, 521, (2003)

[17] M. Allen et al., "PHENIX inner detector", NIM, **A499**, 549, (2003)

[18] C. Adler et al., "The RHIC zero degree calorimeters", Nucl. Instrum. Meth. **A470**, 488-499, (2001)

[19] C. Adler et al., "The RHIC zero-degree calorimeters", Nucl. Instrum. Meth. **A461**, 337, (2001)

[20] P. B. Nilsson, "The pixel readout system for the PHENIX pad chambers", Nucl. Phys. **A661**, (1999)

[21] K. Adcox et al., "Construction and performance of the PHENIX pad chambers", Nucl. Instr. and Meth. **A497**, 263, (2003)

[22] J. Haggerty et al., "Letter of intent for PHENIX reaction plane detector", Internal Letter of Intent, (2006)

[23] S. S. Adler et al.,"PHENIX on-line systems", NIM, **A499**, 560, (2003)

[24] H. A. Weldon, "Simple rules for discontinuities in finite-temperature field theory", Phys. Rev., **D28**:2007-2015, (1983)

[25] C. Gale and J. I. Kapusta, "Vector dominance model at finite temperature", Nucl. Phys., **357**:65-89, (1991)

[26] J. I. Kapusta, P. Lichard, and D. Seibert, "High-energy photons from quark-gluon plasma versus hot hadronic gas", Phys. Rev. **D44**, (1991)

[27] PHENIX Collaboration, S. S. Adler et al., "Systematic studies of the centrality and $\sqrt{s_{\rm NN}}$ dependence of the $dE_{\rm T}/d\eta$ and $dN_{\rm ch}/d\eta$ in heavy ion collisions at mid-rapidity", Phys. Rev. **C71**, 034908, (2005)

[28] PHENIX Collaboration, S. S. Adler et al., "Detailed study of high-$p_{\rm T}$ neutral pion suppression and azimuthal anisotropy in Au + Au collisions at $\sqrt{s_{\rm NN}}$ = 200 GeV", Phys. Rev. **C76**, 034904, (2007)

[29] PHENIX Collaboration, S. S. Adler et al., "Centrality dependence of direct photon production in $\sqrt{s_{\rm NN}}$ = 200 GeV Au + Au collisions", Phys. Rev. Lett. **94**, 232301, (2005)

[30] PHENIX Collaboration, S. S. Adler et al., "Measurement of direct photon production in p+p collisions at $\sqrt{s}$ = 200 GeV", Phys. Rev. Lett. **98**, 012002, (2007)

[31] PHENIX Collaboration, S. S. Adler et al., "Common suppression pattern of η and π^0 mesons at high transverse momentum in Au+Au collisions at $\sqrt{s_{\rm NN}}$ = 200 GeV", Phys. Rev. Lett. **96**, 202301, (2006)

[32] R. Chatterjee, E. S. Frodermann, U. Heinz, and D. K. Srivastava, "Elliptic flow of thermal photons in relativistic nuclear collisions", Phys. Rev. Lett. **96**, 202302, (2006)

[33] PHENIX Collaboration, S. S. Adler et al., "Elliptic flow of identified hadrons in Au + Au collisions at $\sqrt{s_{\rm NN}}$ = 200 GeV", Phys. Rev. Lett. **91**, 182301, (2003)

[34] PHENIX Collaboration, S. S. Adler et al., "Measurement of identified π^0 and inclusive photon second-harmonic parameter v_2 and implications for direct photon production in $\sqrt{s_{\rm NN}}$ = 200 GeV Au+Au", Phys. Rev. Lett. **96**, 032302, (2006)

[35] T. Matsubara, "A new approach to Quantum-Statistical mechanics", Prog. Theor. Phys., **14**:351-378, (1955)

[36] G. David et al., "The PHENIX lead-scintillator electromagnetic calorimeter: Test beam and construction experience", IEEE Trans. Nucl. Sci. **45**, 692, (1998)

[37] J. Barrette et al., "Energy and charged particles flow in 10.8A GeV/c Au+Au collisions", Phys. Rev. **C55**, 1420, (1997)

[38] J. Barrette et al., "Proton and pion production relative to the reaction plane in Au+Au collisions at 11A GeV/c", Phys. Rev. **C56**, 3254, (1997)

[39] S. Turbide, C. Gale, and R. J. Fries, "Azimuthal asymmetry of direct photon in high energy nuclear collisions", Phys. Rev. Lett, **96**, 032303, (2006)

[40] S. Turbide, R. Rapp, and C. Gale, "Hadronic production of thermal photons", Phys. Rev. **C69**, 014903, (2004)

[41] S. Turbide, C. Gale, E. Frodermann, and U. Heinz, "Electromagnetic radiation from unclear collisions at RHIC energies", Phys. Rev. **C77**, 024909, (2008)

[42] J. H. Cobb et al., "Limits on the production of large transverse momentum direct photon deduced from the measurement of low mass electron pairs", Phys. Lett. **78B**, (1978), 519

[43] P. Houvinen, P. E. Kolb, U. W. Heinz, P. V. Ruuskanen, and S. A. Voloshin, "Radial and elliptic flow at RHIC:Further predictions", Phys. Lett. **B503**, 58, (2001)

[44] R. J. Fries, B. Muller, and D. K. Srivastava, "High energy photons from passage of jets through quark gluon plasma", Phys. Rev. Lett., **90**:132301, (2003)

[45] PHENIX Collaboration, S. S. Adare et al., "Enhanced production of direct photons in Au + Au collisions at $\sqrt{s_{\rm NN}}$ = 200 GeV", arXiv:0804.4168, (2008)

[46] U. Heinz, et al., "Elliptic flow of thermal photon/dileptons", Nucl. Phys. **A783**, (2007)

[47] PHENIX Collaboration, K. Adcox et al., "Suppression of hadrons with large transverse momentum in central Au+Au collisions at $\sqrt{s_{\rm NN}} = 130$ GeV", Phys. Rev. Lett. 88, 022301, (2002)

[48] PHENIX Collaboration, S. S. Adler et al., "Identified charged particle spectra and yields in Au+Au collisions at $\sqrt{s_{\rm NN}} = 200$ GeV", Phys. Rev. **C69**, 034909, (2004)

[49] A. M. Poskanzer and S. A. Voloshin, "Methods for analyzing anisotropic flow in relativistic nuclear collisions", Phys. Rev. **C58**, 1671, (1998)

[50] Phool Chand et al., "A primer manual for the PHENIX simulation code PISA", PHENIX Web Site, (1999)

[51] R. Brun, R. Hagelberg, M. Hansroul, and J. C. Lassalle, "Geant: Simulation program for particle physics experiments. user guide and reference manual.", CERN-DD-78-2-REV.

[52] PHENIX Collaboration, A. Adare et al., "Suppression pattern of neutral pions at high transverse momentum in Au+Au collisions at $\sqrt{s_{\rm NN}} = 200$ GeV and constraints on medium transport coefficients", Phys. Rev. Lett. **101**, 232301, (2008)

[53] PHENIX Collaboration, S. S. Adler et al., "High transverse momentum η meson production in $\rm p + p$, $\rm d + Au$, and $\rm Au + Au$ collisions at $\sqrt{s_{\rm NN}} = 200$ GeV", Phys. Rev. **C75**, 024909, (2007)

[54] PHENIX Collaboration, A. Adare et al., "J/ψ Production versus Centrality, Transverse Momentum, and Rapidity in Au+Au Collisions at $\sqrt{s_{\rm NN}} = 200$ GeV", Phys. Rev. Lett. **98**, 232301, (2007)

[55] K. Oyama, "π^0 production in Au+Au collisions at $\sqrt{s_{\rm NN}} = 130$ GeV", Ph.D thesis, (2002)

[56] T. Isobe, "Production of direct photons and neutral pions in relativistic Au+Au collisions", Ph.D thesis, (2007)

[57] H. Masui, "Measurement of centrality dependence of elliptic flow for identified hadrons in Au+Au collisions at $\sqrt{s_{\rm NN}} = 200$ GeV", Ph.D thesis, (2007)

[58] A. Kiyomichi, "Study of identified hadron spectra and yields at mid-rapidity in $\sqrt{s_{\rm NN}} =$ 200 GeV Au+Au collisions", Ph. D thesis, (2005)

[59] M. Konno, "Proton and antiproton production in high energy heavy ion collisions at RHIC", Ph. D thesis, (2007)

[60] S. Bathe, "Run7 EMCal calibration", Internal Analysis Meeting, 18 Nov 2008

[61] Y. Akiba, et al., "Measurement of direct photon via internal conversions in Au+Au and p+p collisions at $\sqrt{s_{\rm NN}} = 200$ GeV", PHENIX Internal Analysis Note 695, (2008)

[62] T. Hachiya et al., "Study of the BBC trigger efficiency based on simulations for run-2 analysis", PHENIX Internal Analysis Note 107 (2002)

[63] T. Isobe et al., "High p_{T} direct photon analysis in the PbSc Run-4 200 GeV Au+Au collisions", PHENIX Internal Analysis Note 545, (2006)

[64] T. Isobe et al., "Final results for π^0 p_{T} spectra and R_{AA} in Au+Au at $\sqrt{s_{\mathrm{NN}}}$ = 200GeV", PHENIX Internal Analysis Note 647, (2007)

[65] D. Morrison, et al., "Centrality determination for 62.4 GeV Au+Au", PHENIX Internal Analysis Note 290, (2004)

[66] K. Reygers, "Glauber Monte-Carlo calculation for Au + Au collisions at $\sqrt{s_{\mathrm{NN}}}$ = 200 GeV", PHENIX Internal Analysis Note 169, (2003)

[67] A. Milov et al., "Hadron decay of ω meson in Run4 Au+Au", PHENIX Internal Analysis Note 537, (2006)

[68] A. Milov et al., "$\phi \rightarrow K^+K^-$ measurement in Run4 Au+Au with no PID", PHENIX Internal Analysis Note 673, (2008)